IMPROVED DROUGHT EARLY WARNING AND FORECASTING TO STRENGTHEN PREPAREDNESS AND ADAPTATION TO DROUGHTS IN AFRICA

DEWFORA

A 7th Framework Programme Collaborative Research Project

Statistical analysis of natural climatic variability and hydrological parameters

WP4-D4.6

October 2012

Coordinator: Deltares, The Netherlands
Project website: www.dewfora.net
FP7 Call ENV-2010-1.3.3.1
Contract no. 265454

Page intentionally left blank

DOCUMENT INFORMATION

Title	Statistical analysis of natural climatic variability and hydrological parameters
Lead Author	GFZ
Contributors	IHE
Distribution	<Please select on of three below> PP: Restricted to other programme participants (including the Commission Services) RE: Restricted to a group specified by the consortium (including the Commission Services) CO: Confidential, only for members of the consortium (including the Commission Services)
Reference	WP4-D4.6

DOCUMENT HISTORY

Date	Revision	Prepared by	Organisation	Approved by	Notes
20/06/2012		Mathias Seibert	GFZ		
27/10/2012		Heiko Apel	GFZ		
31/10/2012		Mathias Seibert	GFZ		

ACKNOWLEDGEMENT

The research leading to these results has received funding from the European Union's Seventh Framework Programme (FP7/2007-2013) under grant agreement N°265454

Page intentionally left blank

Summary

In this report we present the analysis of drought variability in meteorological and hydrological data. Drought was represented by standardised time series of precipitation and runoff to represent anomalies. The analysis investigates the complexity that characterises the relationship of drought in the Limpopo basin with climate anomalies. Drought variability was accessed both in the spatial as well in the temporal domain.

First we show that the Standardised Precipitation Evapotranspiration Index is a measure capable of representing the potential impact of drought on vegetation status. However, the sensitivity of vegetation to water deficit strongly depends on many more local factors. Hence, the sensitivity showed high spatial variation in the basin.

Spatial variability of drought was analysed by employing principal component analysis. Hereby the spatial precipitation anomaly field was dissembled into dominating spatial patterns. The dominating spatial patterns in rainfall anomalies can be reduced to five patterns which still account for 74 % of the total variation. The results indicate that no spatial pattern can be linked directly to a specific climate anomaly. Further work on statistical forecasting will build on promising Sea Surface Temperature regions in the Indian Ocean, Atlantic and Pacific, which were identified in this report as potential predictors.

The temporal variability was analysed based on meteorological and hydrological data. The analysis of the Limpopo wide standardized precipitation provided a large scale perspective of temporal variability. The large scale perspective was contrasted with standardized runoff in smaller subcatchments. We show the shared properties in the frequency domain of these drought signals with climate anomalies. The period 1985 to 1995 is marked by strong changes in precipitation total and signal properties, which could not be attributed to the El Nino phenomenon. However, in general, both precipitation and runoff share signal properties with the El Nino southern oscillation in frequencies between 2 and 16 years. The relationship was stronger on the larger scale, whereas local smaller scale time series can differ strongly from the large scale pattern.

The analyses present a picture of complex spatial and temporal variability and relationships. Prediction models have to able to deal with nonlinear and interacting relationships with climate anomalies. Neither could certain anomalies be associated with spatial patterns nor could certain important climate anomalies be isolated. It is very likely that every drought event is affected by unique combination of different anomalies.

Page intentionally left blank

TABLE OF CONTENTS

LIST OF FIGURES

LIST OF TABLES

1. INTRODUCTION

The task of this deliverable is to analyse the variability of drought in a combined analysis of climatic variability and hydrological variability. Improving understanding of drought variability in the case study region serves as a preliminary step for following work on a statistical forecasting model. Drought is a complex multidimensional and multivariate phenomenon. Here, we approach variability both spatially and temporally to account for the complexity of the problem.

Precipitation anomalies are related to atmospheric anomalies. The most renowned anomaly is the El Nino phenomenon for its global impact on droughts and floods. In Southern Africa, most of the severe droughts are associated with El Nino (Rouault, 2005). Southern Africa has experienced many severe droughts and Rouault (2005) notes an increase in drought covered area since the seventies. Although, their analysis was based on the CRU2 precipitation data set which ends in 1999. Mwale, Yew Gan, & Shen (2004) noted the same trend and found that central Southern African precipitation responded to the El Nino Southern Oscillation (ENSO) when it had associated cycles of ca. 2 and 6 years. The start of the decreasing precipitation trend was even set earlier by (Mwale, Gan, Shen, Shu, & Kim, 2007) who note that precipitation had been increasing from 1950 to 1965. Thereafter it has been decreasing with an intermittant period of higher precipitation during 1985 and 1990. Mwale, Gan, Shen, Shu, & Kim (2007) partly attributed this to ENSO and anomalies in the sea surface temperature (SST) of the Southern Atlantic and the Southwestern Indian Ocean. Various studies have employed different methods to use these teleconnections for rainfall prediction (Landman & Mason, 1999; Mwale et al., 2007).

As summarised in the paragraph above the relation of rainfall and drought variability to climate anomalies has been analysed for the greater Southern African region. Here, we will focus the scope on the smaller Limpopo basin and analyse how spatial and temporal drought variability is related to atmospheric anomalies, which is an important step in the identification of potential predictors (Özger, Mishra, & Singh, 2012). This is necessary since the predictability of rainfall differs between regions within Southern Africa (Landman & Mason, 1999). The spatial variability was analysed for recurring patterns. This reduced dataset was then related to climate anomaly indexes and SST. In this approach it was tested whether spatial drought patterns within the basin could be caused by specific anomalies.

The temporal variability of drought was analysed based on the basin wide precipitation anomaly and runoff anomalies of available subcatchments. Wavelet analysis was applied to

analyse the time series in the frequency domain and show signal coherences with climate anomaly indexes.

Southern Africa has regions of very different climatology and ecology, thus it can be misleading to compare rainfall deficit as a measure of drought. Hence, the Standardized Precipitation Index (SPI and its successor the Standardized Precipitation Evapotranspiration Index (Vicente-Serrano, Beguería, & López-Moreno, 2010) have been in use for this purpose (Rouault, 2005). This is particularly important for studies covering large regions. Here, we used SPI and SPEI in the Limpopo basin, a catchment of approx. 400.000 km². In order to investigate how well SPEI represents the drought impact on vegetation, we show a validation attempt using remotely sensed vegetation condition.

2. DATA AND METHODS

The analyses in this report used hydrological and meteorological data. The meteorological data encompasses the reanalysis data of ERA-Interim including the drought indexes SPI and SPEI and climate indexes of different sources which are listed in Table 1. Runoff data sources analysed here are from the Global Runoff Data Centre (GRDC, http://www.bafg.de/GRDC), the regional water administration in Mozambique (ARA-SUL) and from the Department of Water Affairs of the Republic of South Africa (http://www.dwaf.gov.za/Hydrology/). Furthermore, metadata such as catchment boundaries and rivers were taken from the free HydroSHEDS data set (http://hydrosheds.cr.usgs.gov/). Country boundaries were used unchanged from the Global Administrative Areas database version 2.0 (GADM, http://www.gadm.org/) or as available in the R package "maps" which builds upon the CIA World Data Bank II (http://www.evl.uic.edu/pape/data/WDB/).

The available runoff data covered a high number of stations. Many of these had small catchments. Data preprocessing covered three steps. First, a quality control was performed, second, completeness was checked, third and last, priorities were assigned to the stations. Then, the Standardized Runoff Index (Shukla & Wood, 2008) was calculated for the runoff time series. See following paragraphs for details on the preprocessing procedure.

The quality control dealt with the occurrence of sequences of repeated values. Two cases of repeated values are distinguished: repeated zeros and other repeated values. Several datasets had zero runoff over periods of several years, thus, it was assumed that these were periods of missing values. However, in arid regions rivers can fall dry with zero runoff for several months. Hence, periods of zero runoff had to be removed only, when they were abnormally long. Here, zero periods with a length of more than 1.5 times the inter quartile range above the median length were removed. This is an outlier threshold common to box-whisker-plots to identify extreme values. By following this approach the thresholds were defined specifically per station to account for the different runoff regimes. A different and simpler approach was chosen to account for sequences of repeated values other than zero. If any value other than zero was repeated for more than three month then the sequence was deleted.

Following on the quality control, a data summary was created by calculating the following indicators:

- Start and end of record
- Total Number of data points, number of gaps and rel. completeness
- Number of data points, number of gaps and rel. completeness after 1979 (start time of ERA-Interim period)

- Number of drought events below a standardized runoff index (SRI) value of -0.5, which is a mild drought threshold.

Some of these indicators were used in the assignment of priorities to the stations. Three priorities were assigned based on catchment size, completeness of record and length of record (for details see Table 2). In the Limpopo basin only 11 stations had priority one (see Figure 2-1).

The analysis presented in this report was performed with the statistical programming environment R (R Development Core Team, 2011).

Table 1: Climate indexes used in correlation analyses

Variable / Data set	**Covered period**	**Source**
Southern Oscillation Index (SOI)	01.1951 - now	Climate Prediction Center of NOAA: ftp://ftp.cpc.ncep.noaa.gov/wd52dg/data/indices/soi
ENSO indexes (ERSST)	01.1950 - now	Climate Prediction Center of NOAA: http://www.cpc.ncep.noaa.gov/data/indices/ersst3b.nino.mth.ascii
ENSO indexes (OISST)	01.1982 - now	Climate Prediction Center of NOAA: http://www.cpc.ncep.noaa.gov/data/indices/sstoi.indices
Darwin sea level pressure (SLP)	01.1951 - now	Climate Prediction Center of NOAA: http://www.cpc.ncep.noaa.gov/data/indices/darwin
Tahiti SLP	01.1951 - now	Climate Prediction Center of NOAA: http://www.cpc.ncep.noaa.gov/data/indices/tahiti
North Atlantic Oscillation (NAO)	01.1950 - now	Climate Prediction Center of NOAA: ftp://ftp.cpc.ncep.noaa.gov/wd52dg/data/indices/nao_index.tim
Indian Ocean Dipole Mode Index (DMI)	11.1981 - now	Based on NOAA OISST Ver.2 http://www.jamstec.go.jp/frcgc/research/d1/iod/DATA/dmi.monthly.ascii
Oceanic Nino Index (ONI)	02.1950 - now	Based on ERSST.v3b of Climate Prediction Center of NOAA: http://www.cpc.ncep.noaa.gov/products/analysis_monitoring/ensostuff/ensoyears.shtml
Trans Nino Index (TNI)	03.1870 - now	HadSST1.1 until Nov 1981 and NCEP NOAA OI after: http://www.esrl.noaa.gov/psd/gcos_wgsp/Timeseries/Data/tni.long.data
NINO3.4 (HadSST)	1871 - 2011	http://www.esrl.noaa.gov/psd/gcos_wgsp/Timeseries/Data/nino34.long.data

Table 2: Priority definition criteria for runoff gauges in the Limpopo basin.

Criteria	Prioritiy 1	Priority 2	Priority 3
90 % data coverage after 1979	Yes (&)	No	No
More than 30 years observations	Yes (&)	No	No
Catchment area > 4000 km²	Yes (&)	No	No
50 % data coverage after 1979 AND more than 30 years observations AND catchment with > 4000 km²	No	Yes (|)	No
90 % data coverage after 1979 AND missing catchment area	No	Yes (|)	No
Catchment area > 1000 km²	No	No	Yes (&)
More than 20 years of observations	No	No	Yes (&)
Number of stations falling in category (total 454)	13	37	65

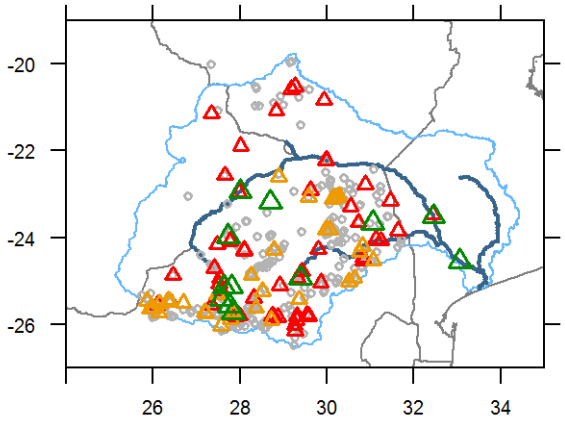

Figure 2-1: Priorities of runoff gauges (GRDC and DWAF) based on length of record and catchment size. Priorities 1,2 and 3 are marked by the green, orange and red triangles, grey mark gauges with no priority due to very short records.

2.1 VALIDATION OF METEOROLOGICAL DROUGHT INDEXES

The validation was performed by investigating the relation of the 3-month aggregated SPEI calculated with the ERA-Interim dataset (Dee et al., 2011) to drought impact. Of the many potential impacts a drought can have, we focused on the impact on vegetation status. Thus, the SPEI was preferred to the SPEI to be able to also account for drought periods that are affected by heat in addition to rainfall anomalies. The normalized difference vegetation index (NDVI) is a MODIS remote sensing product able to capture this information based on the photosynthetically active wavelength range. Hence, NDVI is affected by many ecological factors amongst which water availability is only one. Despite that deficit its use is established in drought monitoring. Here, we used the monthly data of 1km resolution during the time period 2001 to 2010, which was aggregated (arithmetic mean) to the 0.5° resolution grid raster of ERA-Interim (Figure 2-2). Then cell-wise correlations were calculated to highlight regional differences in dependencies.

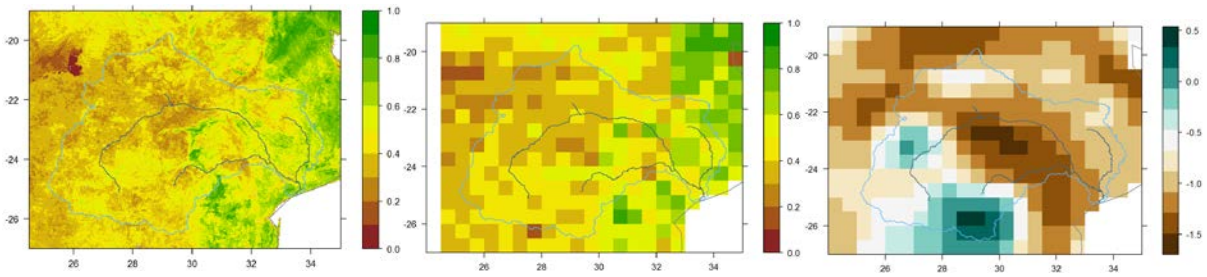

Figure 2-2: Examples of April 2002: NDVI in 1km resolution (left), aggregated to 0.5° resolution (middle) and ERA-Interim SPEI-3 (right).

2.2 PRINCIPAL COMPONENTS ANALYSIS OF SPATIAL PATTERNS

Principal Component Analysis (PCA) is a powerful method to reduce dimensionality of a data set by removing multicollinearity in the data set. It is applied in cases when the data set size has to be reduced without losing essential information, or when dominant modes of variability in a large and complex data set are of interest. Various similar methods exist, following the same general approach but differ by name and to a differing degree by the underlying methods. These are for example Empirical Orthogonal Functions (EOF) and Singular Value Decomposition. Here, Principal Component Analysis was calculated using an R routine based on the Singular Value Decomposition (SVD) method in the package “stats” (R Development Core Team, 2011). However, since the results are the same (Compagnucci & Richman, 2008), it will be referred to the analysis as Principal Component Analysis, for readers convenience.

The PCA output consists of PC loadings, PC scores and the Eigenvalues of the Principal components. The PC loadings are a matrix containing the Eigenvectors in the columns if the Eigenvalue based PCA method is applied and the rotation if the SVD method is applied. The loadings values can be interpreted like correlations, thus a high value indicates that the respective sample has a high resemblance of the "underlying" Principal Component. The PC scores are the patterns associated with every single PC. Matrix multiplication of scores and the transpose of loadings return the original data set: $Z = FA^T$ (Compagnucci & Richman, 2008). The number of resulting PCs equals the number of input variables (dimensions). The number of PCs is reduced by selecting the important ones. Overland & Preisendorfer (1982) presented a test which supports this decision with a test for significance, which was also employed in this study.

In this study PCA was applied on spatiotemporal data, thus two optional analysis approaches exist: PCA can reduce and thus summarize the number of variables either in the spatial or in the temporal dimension. The former case is referred to as T-mode (Compagnucci & Richman, 2008) since the temporal dimension is treated as variables. This leads to principal components which resemble spatial patterns that constitute the variability in the spatial domain. The latter approach is called S-mode and matches the Empirical Ordinary Functions analysis (EOF). In this approach the points in space are treated as variables and as a consequence, the PC scores resemble time series and the loadings contain information on dominance of the PCs in the spatial domain.

PCA in T-mode was applied in this study, since it analyses the spatial domain, returning spatial patterns present in the data set and constituting the spatial variability. The returned principal component scores show the extracted spatial patterns. Based on the Eigenvalues, the explained variation per PC as a part of total variation can be calculated. Significance of the PCs was calculated following the approach of Overland & Preisendorfer (1982).The loadings contain the information to what degree the patterns are present in every time step. Positive values mean a high resemblance of the PC, whereas negative values indicate a high resemblance of an inverted version of the PC pattern. Due to this information contained in the loadings these were used in further analyses.

The loadings of selected principal components were correlated with climate anomaly indexes (for details see Table 4). To identify teleconnected regions, the loadings were correlated with sea surface temperature. Two data sets of sea surface temperature (SST) were employed in this analysis: The ERA-Interim sea surface temperature and the HADSST2 sea surface temperature anomaly data set. The ERA-Interim reanalysis system has SST as a boundary condition and uses SST datasets of the NOAA National Centers for Environmental Prediction

(NCEP) (Dee et al., 2011). For the ERA-Interim data set sea surface temperature anomalies were calculated by removing seasonality. Correlation significance largely depends on the sample size and was calculated by using the t value calculated by $\boldsymbol{t} = \frac{\boldsymbol{r}}{\sqrt{\frac{\mathbf{1}-\boldsymbol{r}^2}{\boldsymbol{N}-\mathbf{2}}}}$, where r is the Pearson correlation coefficient and N is the sample size. The sample size of the analyzed SPEI (3-month aggregation) was 382 and as a consequence correlation coefficients higher than 0.1 are significant at the 0.05 level.

The analysis was based on a 3-month aggregated Standardized Precipitation Evapotranspiration Index (SPEI) calculated from the ERA-Interim dataset over the Limpopo basin. ERA-Interim sea surface temperature and HADSST2 were employed for analysis of teleconnections. Time series of climate anomaly indexes used for correlation analyses are listed in Table 1.

2.3 WAVELET ANALYSIS

Continuous Wavelet analysis was applied as described in (Torrence & Compo, 1998). Continuous Wavelet analysis is a common established tool for the analysis of variability in time series. It is particularly suited for signals which are caused by underlying non-stationary processes. It decomposes a signal locally (in time) into its frequency components. The signal decomposition is powerful tool to understand the components present in a time series in which different frequencies overlay and in which frequencies change over time.

The power of a frequency at a point in time resembles the strength of this frequency at this point in time. However, similar to the Heisenberg uncertainty principle there is a trade off between localisation in time or in the frequency domain. The analysis can be either accurate in the frequency domain or in the time domain. Furthermore, in this context it is essential what type of mother wavelet function is chosen. There are several options available, which have a certain preference to either frequency or time detection. Wavelet bases such as the Mexican hat are more accurate in the temporal domain and less accurate in the frequency domain. Hence, the Mexican hat is appropriate for example in peak detection applications. Though, detection of events was of minor interest in this study, but rather the detection of frequencies present in the runoff signal. Thus, in the present analysis the common Morlet wavelet base was applied, for it is an excellent compromise between time and frequency detection.

In the result and discussion section 3.3 the analysis results of the all Limpopo Standardized Precipitation Index (SPI) based on the ERA-Interim data is presented as well as 5 runoff

stations. Here, SPI was preferred to SPEI, since SPEI needs an estimation of evapotranspiration (ET_p) of the whole basin. By restricting the analysis to SPI the problem of choosing an appropriate large scale ET_p estimation method was circumvented.

In statistical prediction models external predictors are used. The relation to external factors can be complex and non-stationary. The relation and similarity of two variables can be analysed using Wavelet coherence analysis (Grinsted, Moore, & Jevrejeva, 2004). The method analyses common signal properties in the time and frequency domain. Hereby, the relative phase lag between the two time series is analysed, too.

Wavelet coherence plots are similar to the wavelet analysis plot. They differ in that the Wavelet coherence plots show the frequencies that both time series have in common over time. Wavelet coherence can be interpreted as a localized correlation coefficient in time frequency space (Grinsted et al., 2004). Additionally, arrows angles indicate the phase relationship. Arrows directions have the following meaning: right is in phase, up indicates a lead by the black coloured time series, left indicates an anti-phase relation and down indicates a lead by the red highlight time series. For illustrative purpose there is an example shown in Figure 2-3 of two generated oscillating time series of different frequencies. Both have a common frequency of a 1 year period. However the little frequency difference causes a shifting phase throughout the time series which can be observed by the changing arrow directions in the one year band.

Wavelet analysis algorithms require complete records and cannot deal with missing data. The analysis was focused on records without long gaps. In some cases, gaps were filled with zeros after SRI was calculated. It is indicated in the figure captions when time series are presented, which had to be manipulated in this way.

The analysis was performed in R using the packages “dplR” and “WaveletCo”. Figures were adapted from code examples available within the packages.

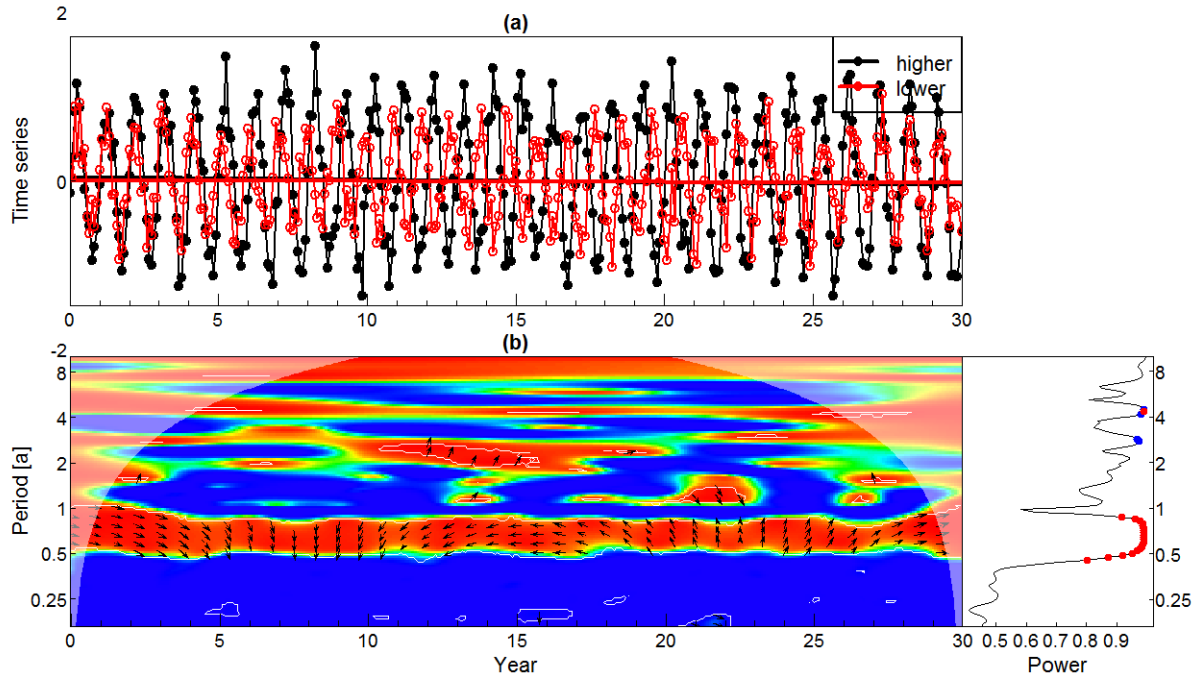

Figure 2-3: Wavelet coherence analysis of two time series (a) one of higher frequency (black) and one of lower frequency (red), this example illustrates the phase angle visualisation by the arrows in the wavelet coherence plot (b). Arrow direction indicate: in phase (right), antiphase (left), red leading black (down), black leading red (up).

3. RESULTS AND DISCUSSION

3.1 VALIDATION OF SPEI WITH NDVI

One of the main challenges in drought early warning is the wide range of impacts. Meteorological monitoring products and drought indexes are excellent for the description of meteorological drought. However, if they are used for drought early warning, an assessment of the triggered drought impact is necessary. Here, we work on the validation of the drought index SPEI with the vegetation index Normalized Difference Vegetation Index (NDVI). NDVI represents vegetation status based on the light absorption in the photosynthetically active wavelength range. Hence, NDVI is affected by many ecological factors amongst which water availability is only one. A reaction by NDVI can be expected when the water deficit reaches a certain minimum threshold. Depending on vegetation type but also time of the season, the relation can differ. Analysing the relation of vegetation status and water deficit locally can improve drought warning systems by providing information on how drought indexes can be interpreted locally.

Here, we show Pearson correlations of SPEI (3 month aggregation) and NDVI. There are strong differences of the correlation throughout the Limpopo basin. High correlation are found in south eastern transect whereas the correlation in the north east and in the southwest are lower. Low correlations can be caused by intense irrigation within a grid cell, but also vegetation type is of importance. For example in sparsely vegetated desert areas, there is only little difference depending on water deficit. This is visible in the cell of lowest correlation in the northwest where NDVI never exceeded 0.3 (see Figure 3-2, right). On the other hand natural vegetation or strictly rainfed agriculture is likely to show stronger dependency on water deficit. This is shown in the example of the cell with highest correlation (see Figure 3-2, left). Due to the coarse resolution most cells are likely to show a less expressed correlation (see Figure 3-2, middle).

Both examples of the maximum and median correlation share properties in the scatterplot patterns. At low values of SPEI the vegetation status decreases and shows less variation. Both figures indicate that below a value of SPI < -1 vegetation is affected by drought. This is a potential way to decide for a drought threshold in drought early warning. In order to develop a stronger framework the relationships will be further investigated to identify potential differences in the threshold.

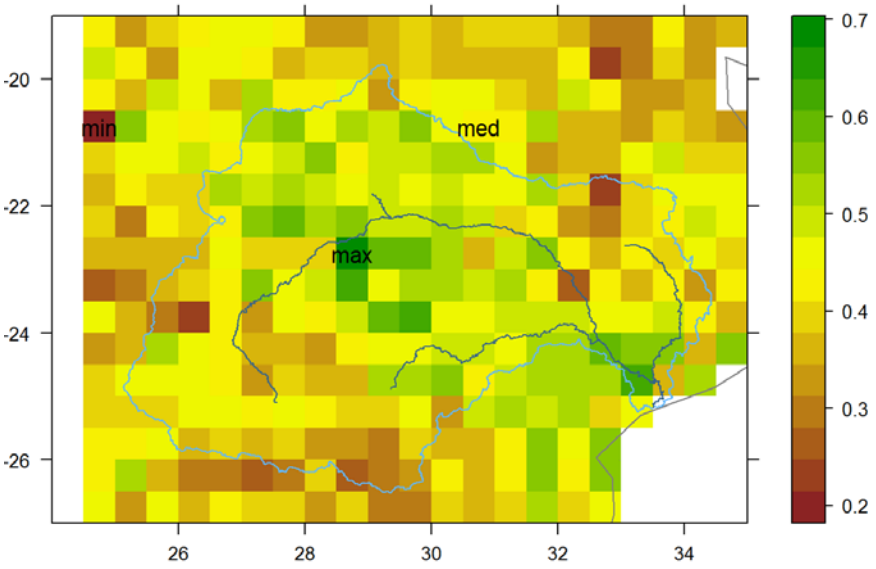

Figure 3-1: Correlation of NDVI and ERA-Interim SPEI 3, cells of minimum, median and maximum correlation are marked.

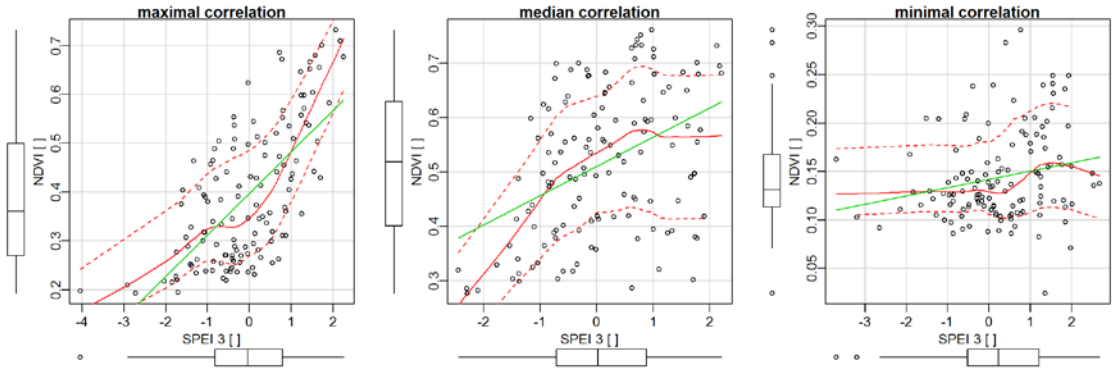

Figure 3-2: NDVI vs. SPEI3: Scatterplots of three exemplary grid cells of maximal, median and minimal correlation. Red lines show a locally weighed fit; the green line shows a linear regression model fit.

3.2 VARIABILITY OF SPATIAL DROUGHT PATTERNS

The spatial variability of meteorological drought within the Limpopo basin was analysed using principal component analysis. The resulting PCs indicate spatial patterns that are dominant modes of the spatial variation. In total there were 334 PCs of which 13 were significant (see Figure 3-3, right). These explained 91 % of the total variation. Here, only the first 6 PCs which sum up to 78 % of total variance are discussed in more detail. PC 1 and PC 2 are simple patterns that divide the region in two. PC 1 shows a drought pattern with a strong south-western gradient (see Figure 3-3). PC 2 shows an orthogonal north-western gradient but also has negative values along the coastline in the East. These first two patterns are very simple thus easy to comprehend and account for 53 % of the total variation.

The subsequent PCs 3 to 5 contribute 8 %, 7 % and 5 % to the total explained variation and exhibit more complex patterns. All three show patterns that divide the region in three (Figure 3-3). The third PC has a depression central over the Limpopo and positive values in the Northeast and Southwest. PC 4 shows a pattern of low values over Limpopo in an area stretching in a North-eastern direction and positive values in the NW and SE. PC 5 has a pattern that has a North-South transect of lower values and high values in the East and West margins. Hence, the PCs one to five all show rather simple patterns. Based on these five patterns 74 % of the total variation can be explained.

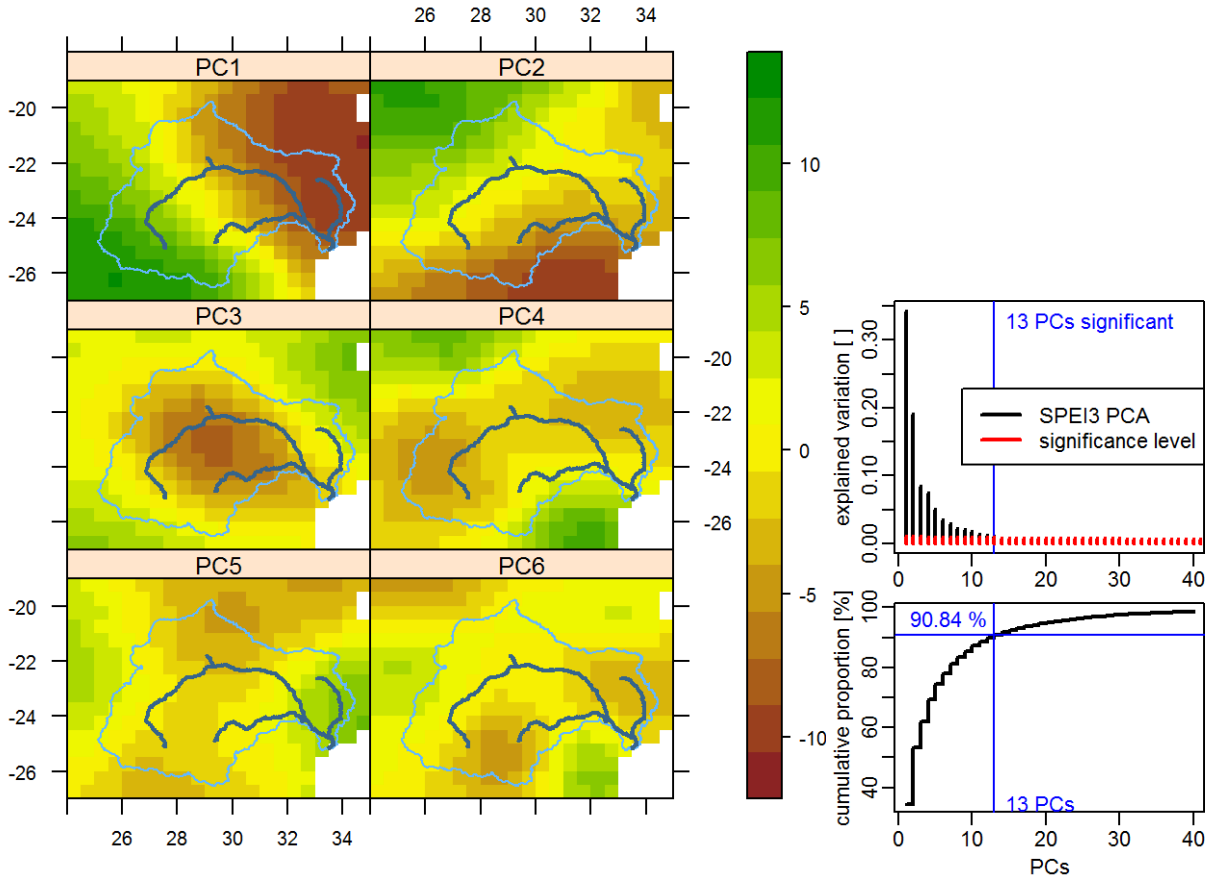

Figure 3-3 Limpopo: Principal component analysis in T-mode of SPEI in 1 month aggregation. Presented are the scores of the principal components 1-6 (left figures) and the explained variation (right figures).

Table 3: Spearman rank correlation of Limpopo SPI (ERA-Interim) and a selection of climate anomaly indexes.

Climate anomaly index	SPI1	SPI3	SPI6	SPI9	SPI12	SPI18	SPI24
SOI anomaly	0,16	0,26	0,27	0,27	0,29	0,31	0,28
NINO1.2 anomaly (OISST)	-0,16	-0,24	-0,27	-0,33	-0,34	-0,29	-0,22
NINO3 anomaly (OISST)	-0,20	-0,26	-0,32	-0,36	-0,35	-0,29	-0,23
NINO4 anomaly (OISST)	-0,21	-0,27	-0,31	-0,30	-0,29	-0,24	-0,22
NINO3.4 anomaly (OISST)	-0,23	-0,29	-0,32	-0,35	-0,33	-0,29	-0,24
NINO1.2 anomaly (ERSST)	-0,15	-0,22	-0,25	-0,31	-0,31	-0,25	-0,18
NINO3 anomaly(ERSST)	-0,22	-0,28	-0,31	-0,35	-0,34	-0,28	-0,22
NINO4 anomaly(ERSST)	-0,18	-0,25	-0,27	-0,26	-0,25	-0,20	-0,18
NINO3.4 anomaly(ERSST)	-0,24	-0,30	-0,33	-0,35	-0,34	-0,30	-0,26
DARWIN SLP anomaly	-0,15	-0,24	-0,23	-0,20	-0,20	-0,21	-0,20
TAHITI SLP anomaly	0,11	0,19	0,22	0,24	0,26	0,29	0,25
Oceanic Nino Index	-0,24	-0,31	-0,35	-0,38	-0,37	-0,32	-0,28

Table 4: Spearman rank correlation of PC loadings and a selection of climate anomaly indexes.

Climate anomaly index	PC1	PC2	PC3	PC4	PC5	PC6
SOI anomaly	-0,06	-0,03	-0,17	-0,01	-0,30	0,13
NINO3 anomaly (OISST)	0,15	0,01	0,18	0,08	0,26	-0,06
NINO4 anomaly(OISST)	0,16	0,05	0,19	0,00	0,25	-0,09
NINO3.4 anomaly (OISST)	0,15	0,03	0,18	0,02	0,27	-0,10
NINO3 anomaly (ERSST)	0,14	0,01	0,22	0,08	0,25	-0,05
NINO4 anomaly (ERSST)	0,18	0,05	0,18	-0,01	0,25	-0,07
NINO3.4 anomaly (ERSST)	0,17	0,02	0,20	0,02	0,28	-0,09
Darwin SLP anomaly	0,05	0,00	0,17	0,05	0,32	-0,11
Dipole Mode Index	-0,01	0,06	0,00	0,01	0,21	0,11
Oceanic Nino Index	0,17	0,02	0,20	0,03	0,26	-0,09

The extracted major patterns can be used to reconstruct the original data based on reduced number of PCs, which reduces noise in the time series. In this process the loadings resemble the strength of the selected pattern at each time step. Thus, the loadings are time series for every PC, in contrast to the spatial patterns shown in Figure 3-3 presenting the PC scores.

SPI calculated for the whole Limpopo basin shows low correlation with atmospheric anomalies (Table 4). If the extracted patterns are related to physical processes or to atmospheric anomalies then the loadings should be correlated with indexes that represent these anomalies. Correlations were found up to a value of 0.32 for PC 5 with Darwin sea level pressure (Table 4). This is in a similar order as correlations of all-Limpopo SPI3 which had a maximal correlation of 0.31 (Table 3). Of the PCs PC 5 had the highest correlation with all the climate anomaly indexes. All but the Indian Ocean Dipole Mode Index (DMI) are Pacific Ocean anomalies, hence they have some collinearity and it is expected that PC5 has correlation with all of them. In contrast, DMI has less collinearity with the ENSO related

indices but it still correlated with PC5. We expect, that this is rather indicative of the all in all low correlation of PC5 then an indication of similar influence of DMI and ENSO on the SPI pattern of PC5.

The correlation analysis of PC loadings with climate anomaly indexes ignored two important aspect of teleconnections. First, sea surface temperature might be a better predictor than the indexes and second the relationship could have some time lag. As a consequence, here we present the correlations of Sea Surface Temperature (SST) anomalies and the PC loadings in Figure 3-4 to Figure 3-9. However, correlations rarely exceed 0.3 either, but all PCs have different correlation patterns. PC1 shows significant correlations all over the planet (Figure 3-4) in contrast to PC2 and PC3 which have the strongest correlations in the northern Atlantic and the southern Atlantic, respectively (Figure 3-5 and Figure 3-6). PC4 has small spots of significant correlation all over the globe with a tendency to the southern Indian Ocean and Atlantic (Figure 3-7). PC 5 shows a dominance of correlations with the Pacific ocean SST (Figure 3-8). PC6 exhibits the strongest correlations with SST in the northern Indian Ocean and Atlantic (Figure 3-9). Thus, regarding the first hypothesis that SST might be suited better than climate anomaly indexes, it can be stated that SST correlations are able to highlight specific important regions. Though, correlations are still very low and thus add little information.

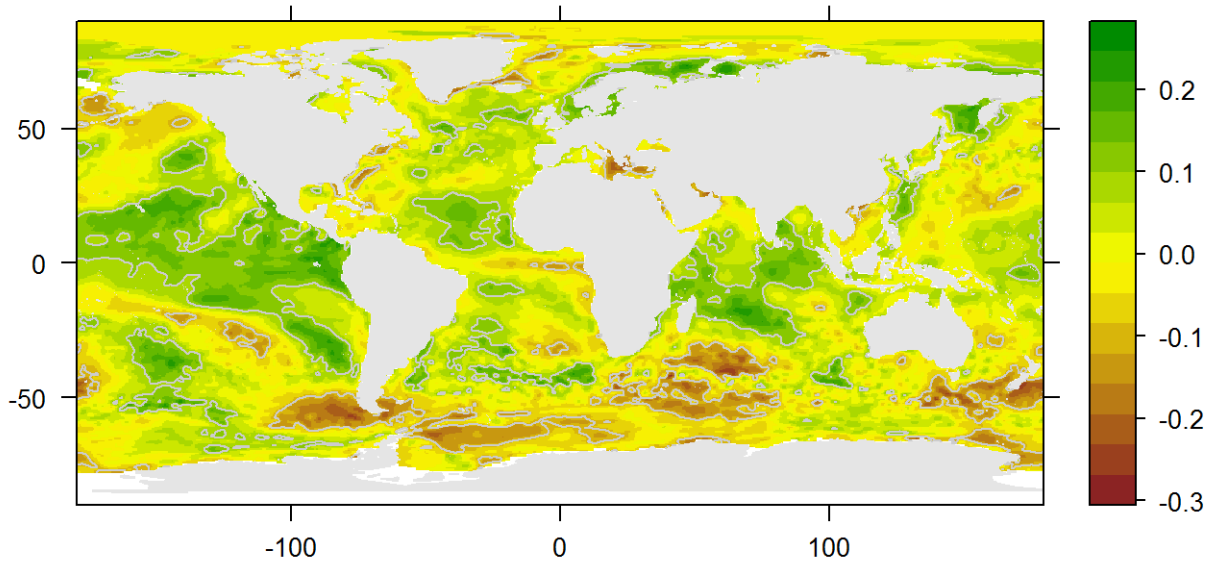

Figure 3-4: ERA-Interim SST anomaly correlation with **PC1** loadings of SPEI in 3 month aggregation (Limpopo basin). Grey contours denote 0.95 level of correlation significance.

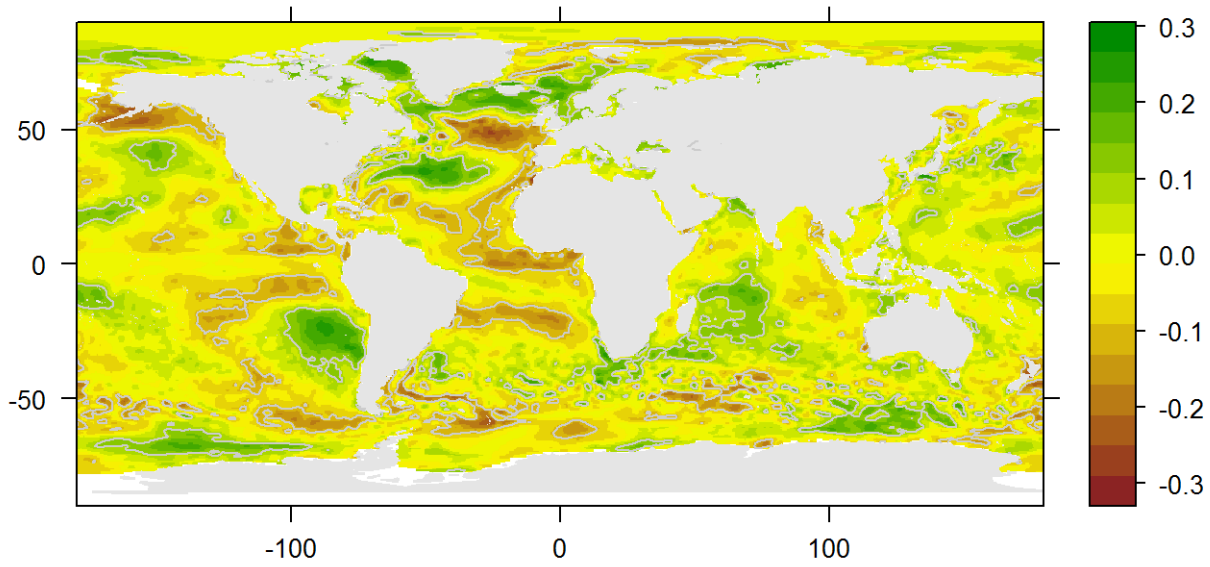

Figure 3-5: ERA-Interim SST anomaly correlation with **PC2** loadings of SPEI in 3 month aggregation (Limpopo basin). Grey contours denote 0.95 level of correlation significance.

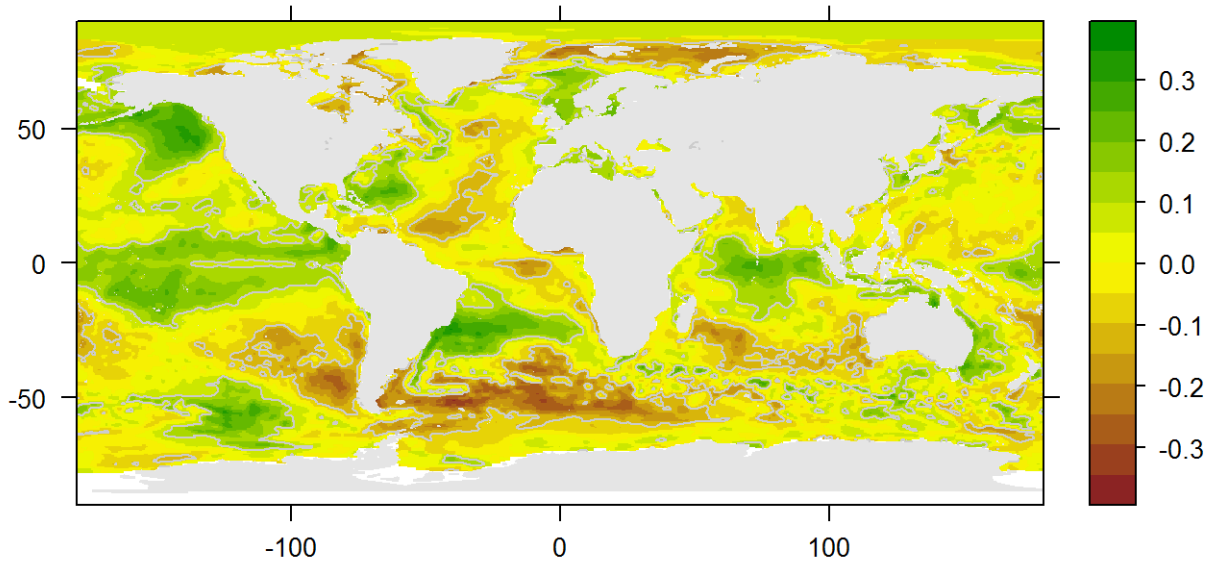

Figure 3-6: ERA-Interim SST anomaly correlation with **PC3** loadings of SPEI in 3 month aggregation (Limpopo basin). Grey contours denote 0.95 level of correlation significance.

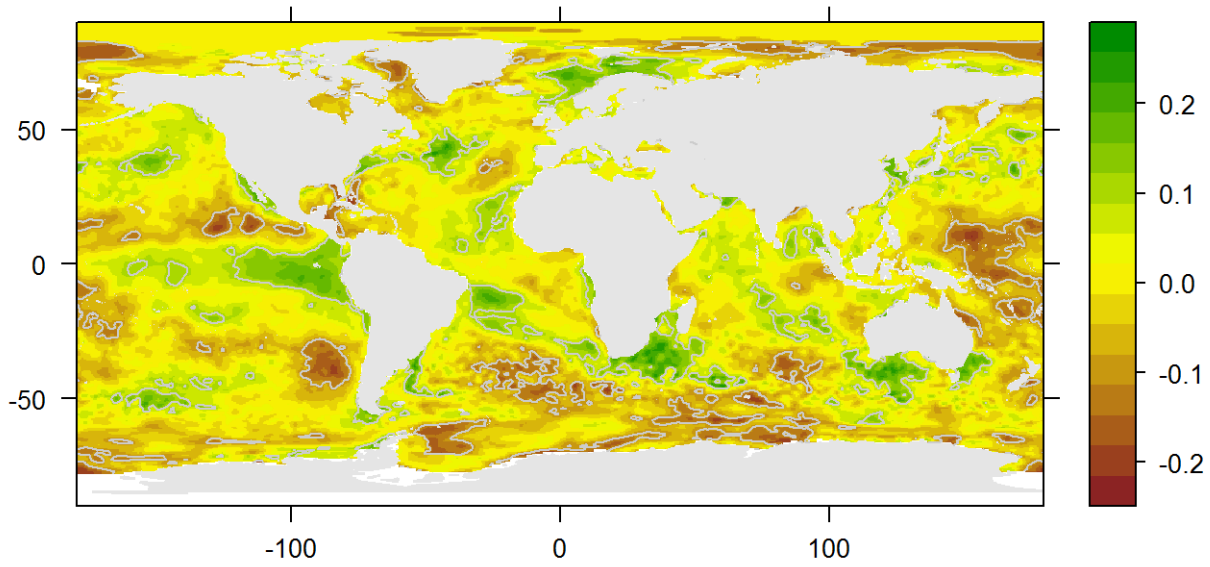

Figure 3-7: ERA-Interim SST anomaly correlation with **PC4** loadings of SPEI in 3 month aggregation (Limpopo basin). Grey contours denote 0.95 level of correlation significance.

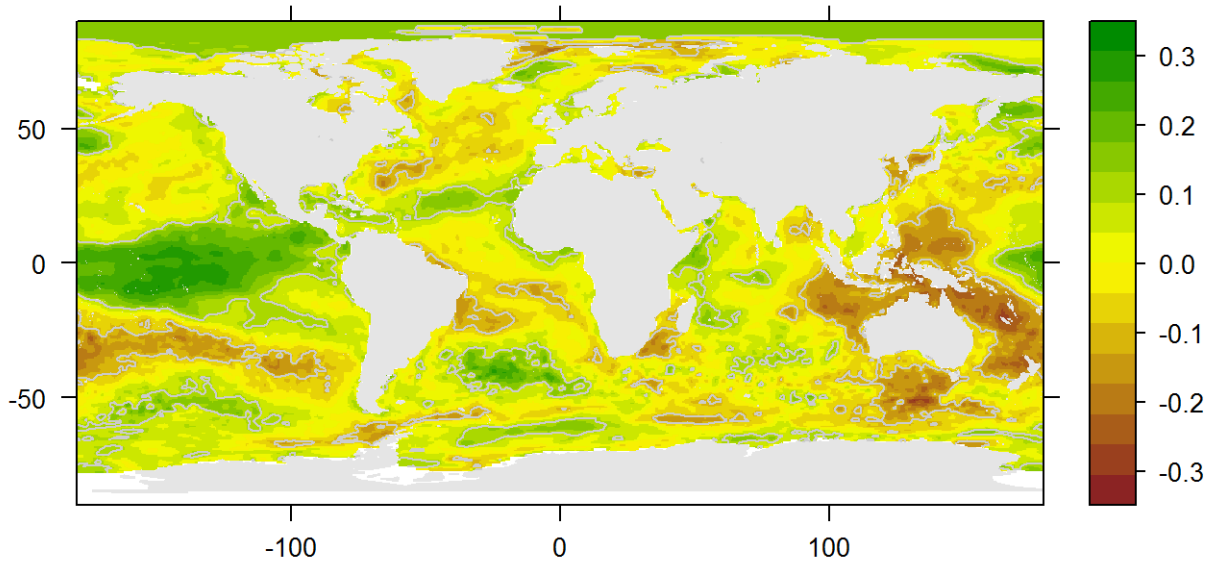

Figure 3-8: ERA-Interim SST anomaly correlation with **PC5** loadings of SPEI in 3 month aggregation (Limpopo basin). Grey contours denote 0.95 level of correlation significance.

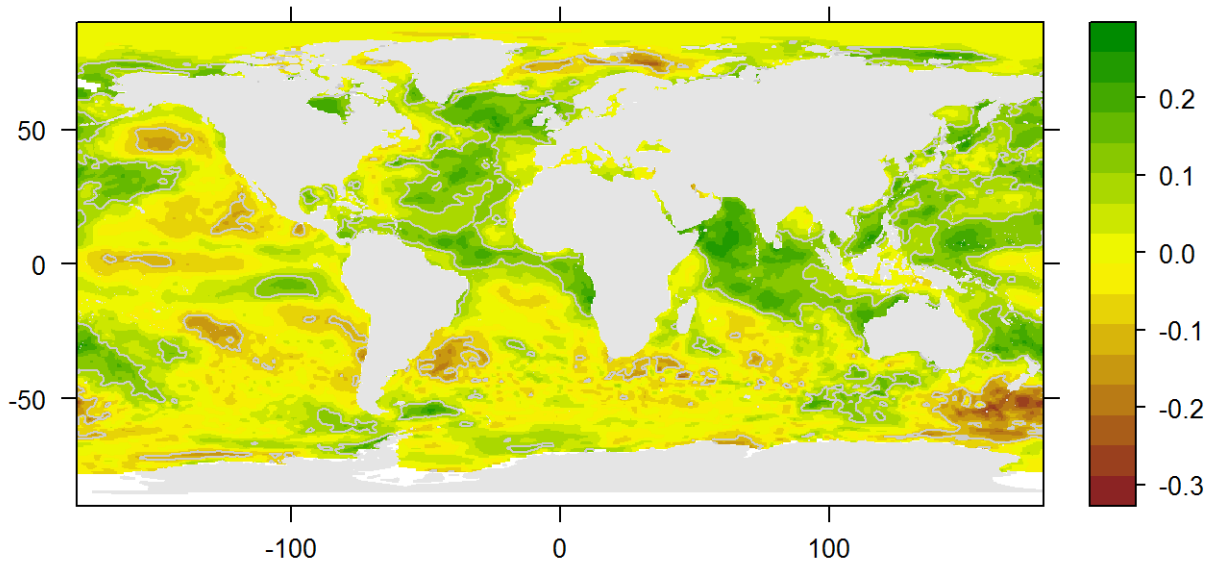

Figure 3-9: ERA-Interim SST anomaly correlation with **PC6** loadings of SPEI in 3 month aggregation (Limpopo basin). Grey contours denote 0.95 level of correlation significance.

It remains to test the second hypothesis, whether the introduction of time lags increase correlations. In order to test this, crosscorrelations of the SST field and the PC loadings were calculated. In Figure 3-10 to Figure 3-15 we present for every grid cell the highest correlation and the respective lag. Here, negative lags indicate leading SST anomalies. The correlations were higher than with contemporary correlations only, and all PCs had correlations of more than 0.3 magnitude. A few regions exceeded 0.4 which shows, that some teleconnections have a time lag. In the following paragraph the most important SST regions that have a negative lag (leading the PC loadings) will be highlighted.

PC1 SST correlations show negative lags in the Atlantic greater Cape Verde region. Amongst many small regions all around the globe the Atlantic shore of Southern Africa and the western equatorial Indian Ocean point out. All three regions are confirmed by correlations with the HADSST2 dataset (see appendix Figure 6-26). PC2 shows the main regions of negative lag in the Caribbean Sea extending into the Atlantic (Figure 3-11), which is confirmed by the HADSST2 dataset (appendix Figure 6-27). PC3 has regions with negative lag in the Southern Atlantic and the Western equatorial Pacific (Figure 3-12). PC4 shows no larger regions with high negatively lagged correlations (Figure 3-13). It is interesting to note that PC5 is correlated with contemporary equatorial Pacific, with a tendency to negative lag in the East (Figure 3-14), which is also shown with the HADSST2 dataset (appendix Figure 6-30). Additionally, some regions in the south-western and south-eastern Pacific are correlated with negative lag. For PC6 the strongest correlations with negative lag are in the South Atlantic. Furthermore several regions in the northern and southern Pacific show negative lags.

All patterns have different SST regions that show negative lags. It is common to all different correlation analyses within this study that correlations were weak. There are several potential reasons for that. One explanation might by the chosen approach. Spatial drought variability as decomposed by the T-mode PCA might not be affected by these large scale teleconnections. Another possible reason is, that in the given approach, seasonally changing teleconnections are not represented. For example a strong isolated effect of ENSO on June precipitation might be masked by the integrated correlation approach. Here, analyses of the all Limpopo SPI support this hypothesis (data not shown). Although correlations are low in the approach presented here, there might be predictive power in the combination of the regions, which will be tested in future work.

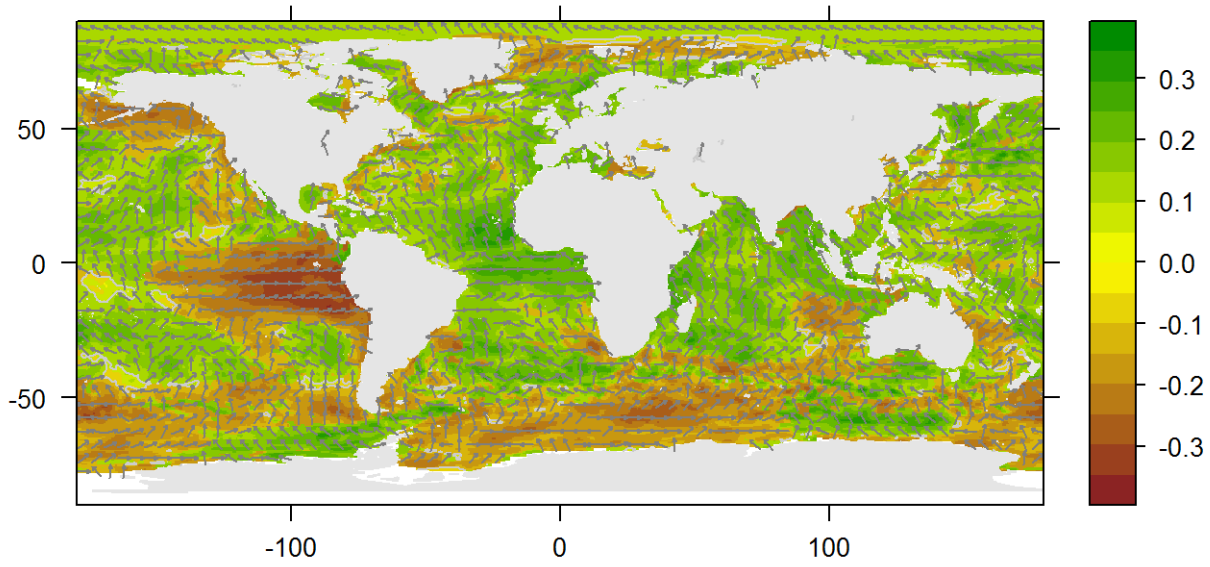

Figure 3-10: Crosscorrelations of **PC1** loadings of SPEI in 3 month aggregation (Limpopo basin) and ERA-Interim SST anomaly. The maximal correlation within a lag of 2 years is shown and arrow directions represent the respective lag. Arrows pointing left indicate negative lags, thus leading SST anomaly. Arrows pointing right indicate positive lags, thus leading PC loadings. Grey contours denote 0.95 level of correlation significance.

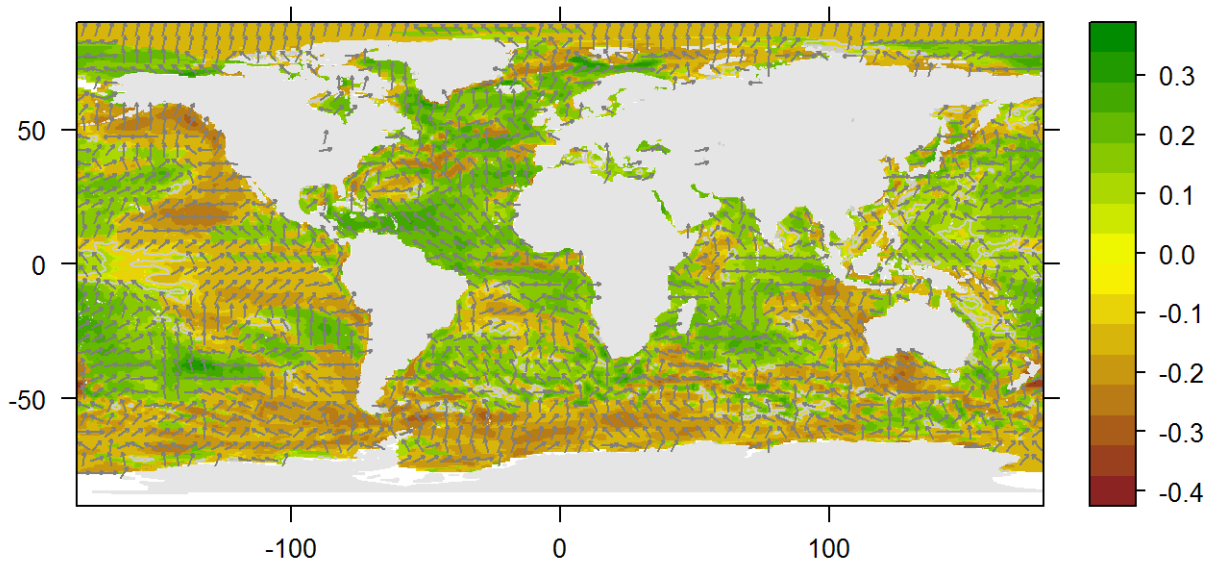

Figure 3-11: Crosscorrelations of **PC2** loadings of SPEI in 3 month aggregation (Limpopo basin) and ERA-Interim SST anomaly. The maximal correlation within a lag of 2 years is shown and arrow directions represent the respective lag. Arrows pointing left indicate negative lags, thus leading SST anomaly. Arrows pointing right indicate positive lags, thus leading PC loadings. Grey contours denote 0.95 level of correlation significance.

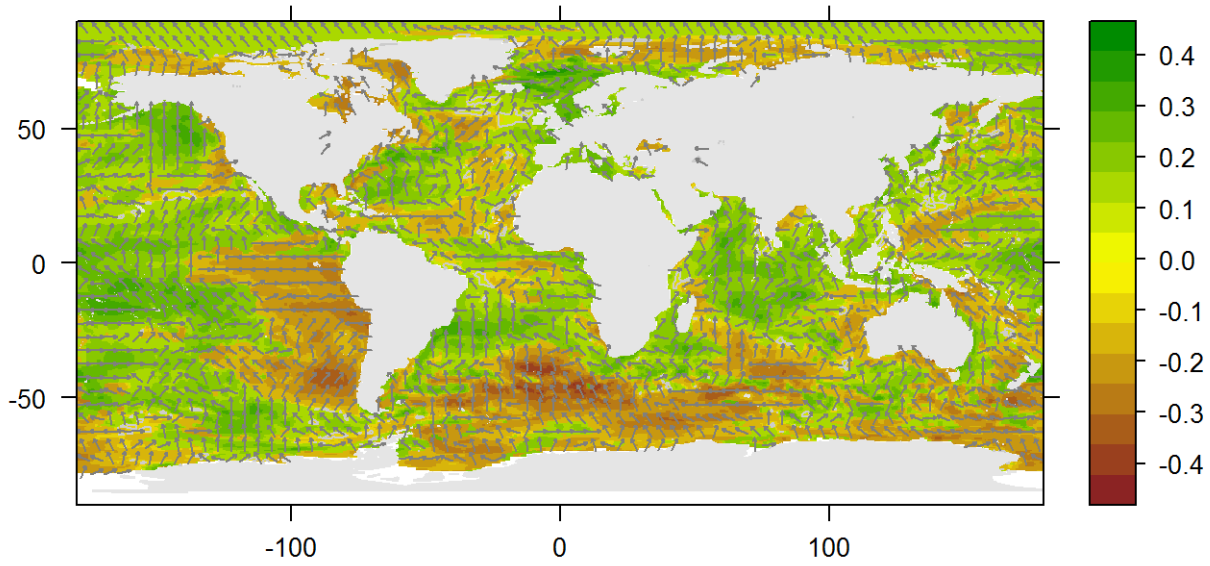

Figure 3-12: Crosscorrelations of **PC3** loadings of SPEI in 3 month aggregation (Limpopo basin) and ERA-Interim SST anomaly. The maximal correlation within a lag of 2 years is shown and arrow directions represent the respective lag. Arrows pointing left indicate negative lags, thus leading SST anomaly. Arrows pointing right indicate positive lags, thus leading PC loadings. Grey contours denote 0.95 level of correlation significance.

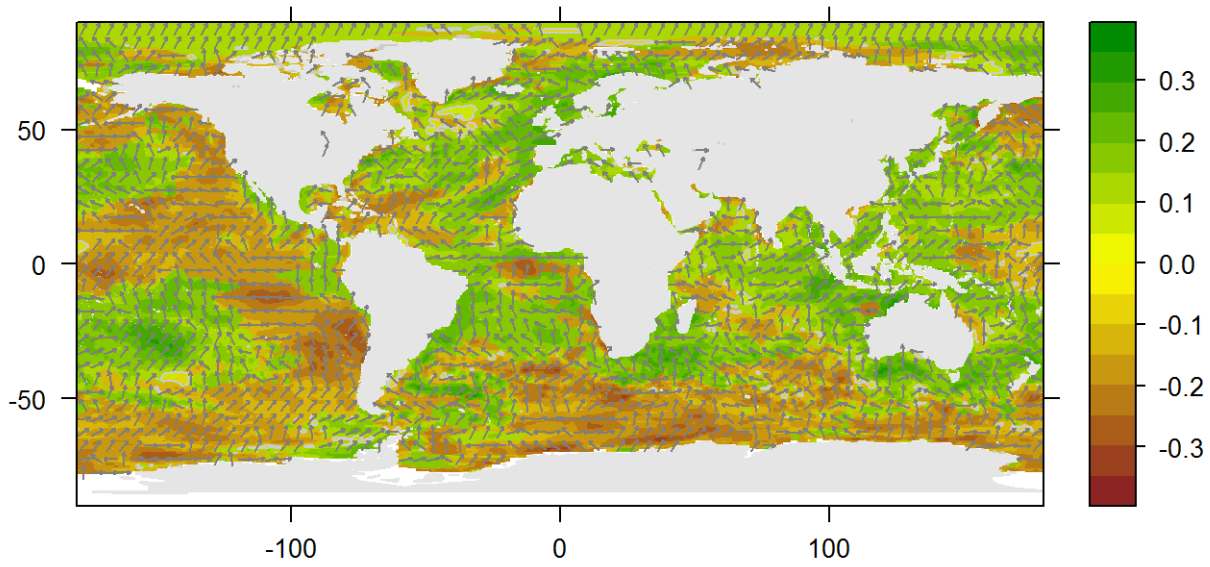

Figure 3-13: Crosscorrelations of **PC4** loadings of SPEI in 3 month aggregation (Limpopo basin) and ERA-Interim SST anomaly. The maximal correlation within a lag of 2 years is shown and arrow directions represent the respective lag. Arrows pointing left indicate negative lags, thus leading SST anomaly. Arrows pointing right indicate positive lags, thus leading PC loadings. Grey contours denote 0.95 level of correlation significance.

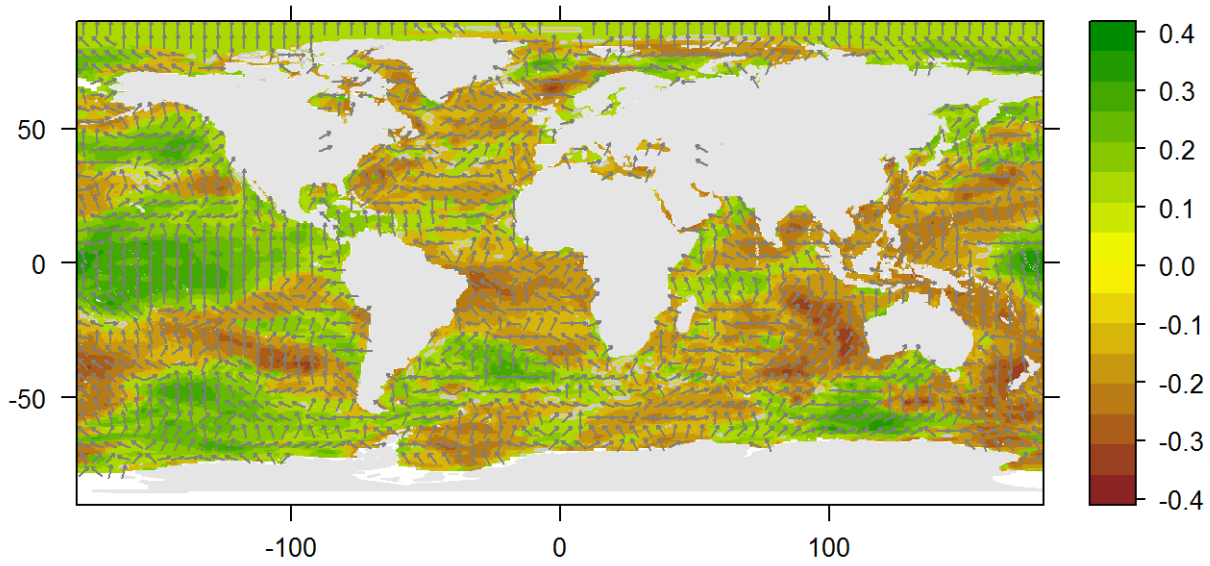

Figure 3-14: Crosscorrelations of **PC5** loadings of SPEI in 3 month aggregation (Limpopo basin) and ERA-Interim SST anomaly. The maximal correlation within a lag of 2 years is shown and arrow directions represent the respective lag. Arrows pointing left indicate negative lags, thus leading SST anomaly. Arrows pointing right indicate positive lags, thus leading PC loadings. Grey contours denote 0.95 level of correlation significance.

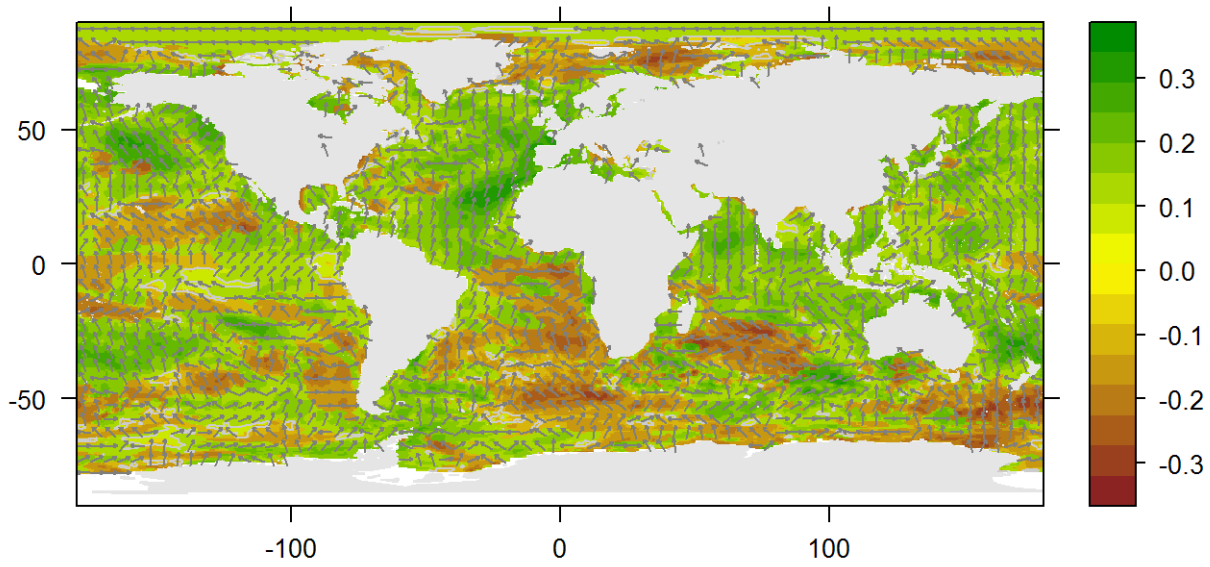

Figure 3-15: Crosscorrelations of **PC6** loadings of SPEI in 3 month aggregation (Limpopo basin) and ERA-Interim SST anomaly. The maximal correlation within a lag of 2 years is shown and arrow directions represent the respective lag. Arrows pointing left indicate negative lags, thus leading SST anomaly. Arrows pointing right indicate positive lags, thus leading PC loadings. Grey contours denote 0.95 level of correlation significance.

Table 5: SST regions that have negatively lagged correlations the PCs, which indicates a potential lead time in statistical models.

	Cape Verde	South African Atlantic	East African Indian	Carribbean Sea	Western equ. Pacific	Southern Atlantic	eastern equ. Pacific	northern Pacific	southern Pacific
PC1	X	X	X						
PC2				X					
PC3					X	X			
PC4									
PC5							X		X
PC6						X		X	X

3.3 TEMPORAL VARIABILITY: WAVELET ANALYSIS

With higher aggregation order, the SPI time series show less power in shorter periods. For example, the SPI1 time series (Figure 3-16) has events within the low 4 to 16 months periodicity range (approx. one year), which are longer present in the 18 month aggregation SPI (Figure 3-18). This is expected, since the SPI aggregation has an effect similar to a moving average. However, both SPI time series (SPI1 and SPI18) have power in the higher period range of 32 to 64 months (approx. 2-6 years). The longer periodicity is clearly visible in the SPI18 time series, but not in the SPI1 time series. This shows the strength of wavelet analysis, which is capable of isolating signals that are directly apparent viewing the original time series.

In addition the variability the timing of events is affected by the SPI-aggregation. Here, wavelet coherency will be applied in the next section to analyse wavelet coherence of SPI and climate anomalies.

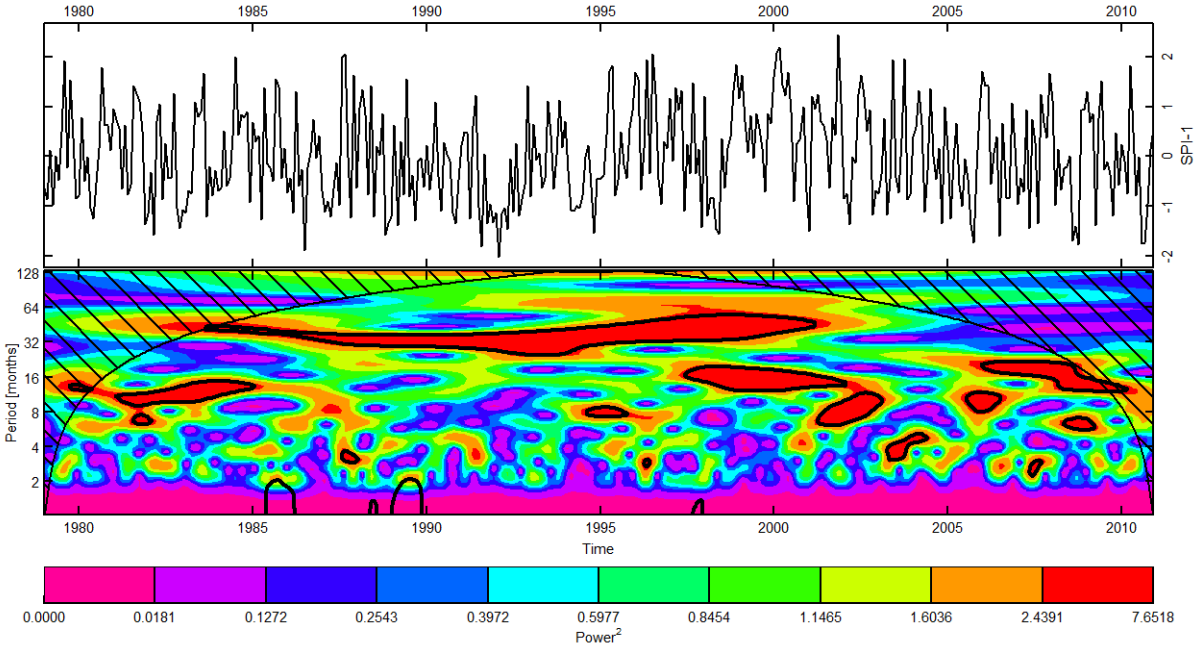

Figure 3-16: Wavelet analysis: Limpopo 1-month-SPI (upper) and wavelet power spectrum (lower) with contours showing significance.

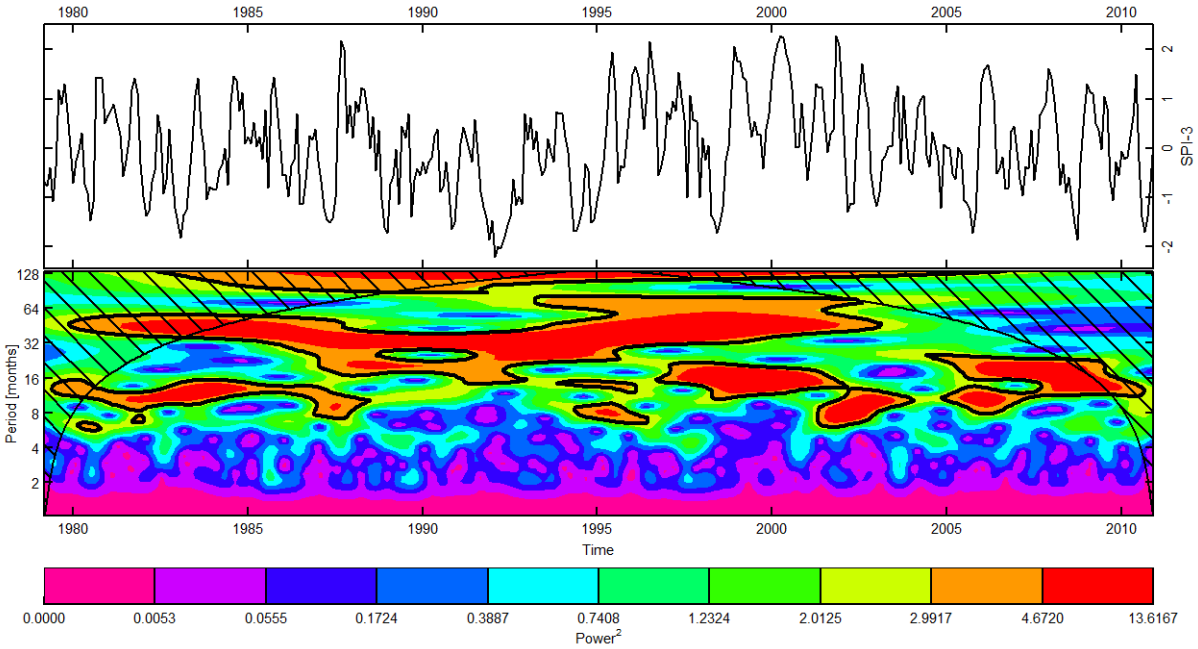

Figure 3-17: Wavelet analysis: Limpopo 3-month-SPI (upper) and wavelet power spectrum (lower) with contours showing significance.

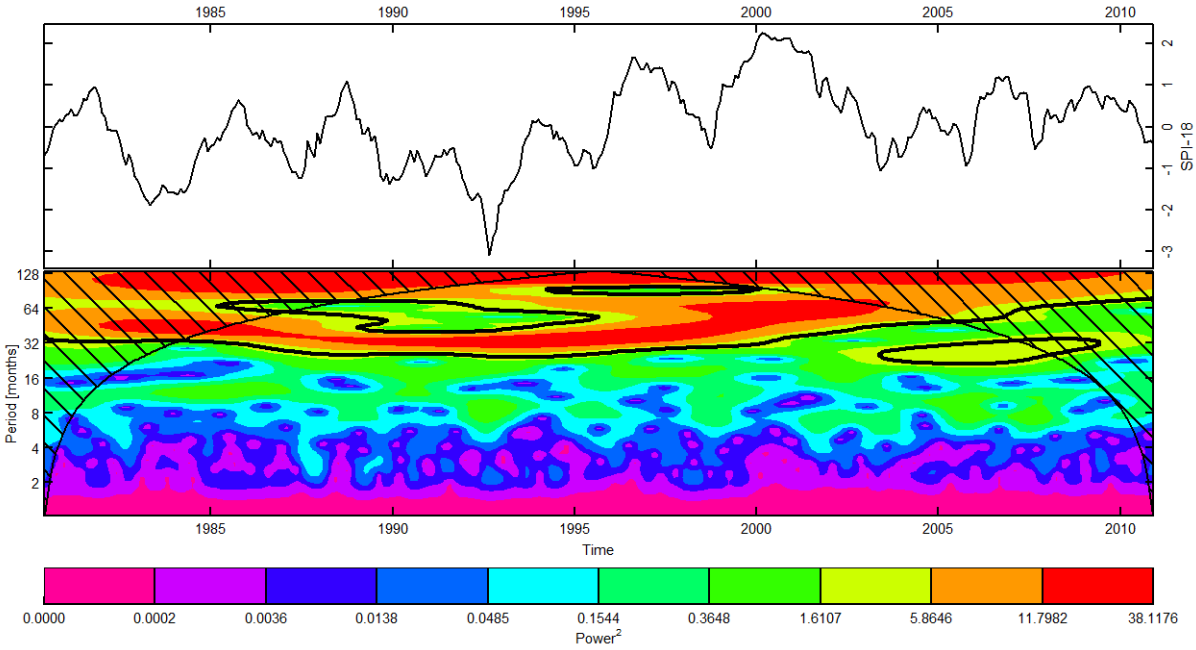

Figure 3-18: Wavelet analysis: Limpopo 18-month-SPI (upper) and wavelet power spectrum (lower) with contours showing significance.

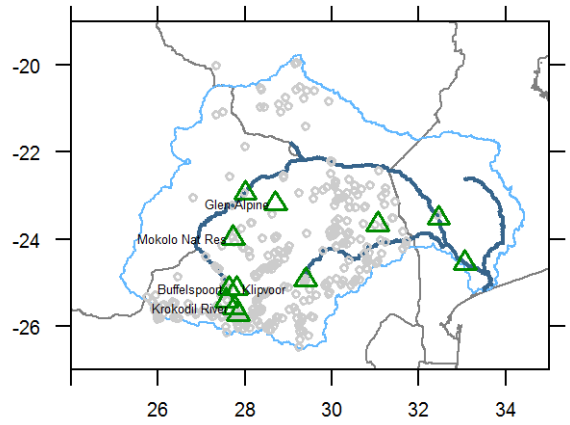

Figure 3-19 First priority runoff gauges with complete record.

Runoff stations with complete and long records and minimum catchment size of 4000 km² were chosen (see Table 2 in section 2 for details) for wavelet analysis of hydrological droughts in the Limpopo.

Southern Africa experienced a long period of decreased rainfall from 1965 to 1997. During that time intense drought struck the basin. This long time frame was intermitted by aperiod of higher rainfall between 1985 and 1990 which Mwale, Gan, Shen, Shu, & Kim, 2007 partly attributed to ENSO and cooling in the surrounding Oceans. The SPEI calculated based on ERA-Interim data also shows this pattern (Figure 3-18). Runoff during that time decreased in most stations. For example, the Pienaars River in South showed this and the Mogalakwena River laying central in the Limpopo also had decreased runoff in the rainy season and the dry

season as well (Figure 3-22). In Krokodil River the decrease in runoff was also very strong between 1985 and 1995 (Figure 3-21). Additionally to the change in quantity, there was an obvious change the frequency domain during these periods. All the examples below (Figure 3-20 to Figure 3-22) have periods with high power in the 16 to 32 month band (approx.. 2-3 years). During the 80ies and early 90ies the power is very much reduced. In this respect, Mogalakwena River is different, since the power in the 32 month band was retained during this period, while lower periods lost power.

The change in the power spectrum during that period is obvious. Causes are not apparent here, though it could be connected to a change in the atmospheric systems' dynamic. Hence, to test this, in the next section wavelet coherence analysis will be applied to analyse the relation to climate anomalies.

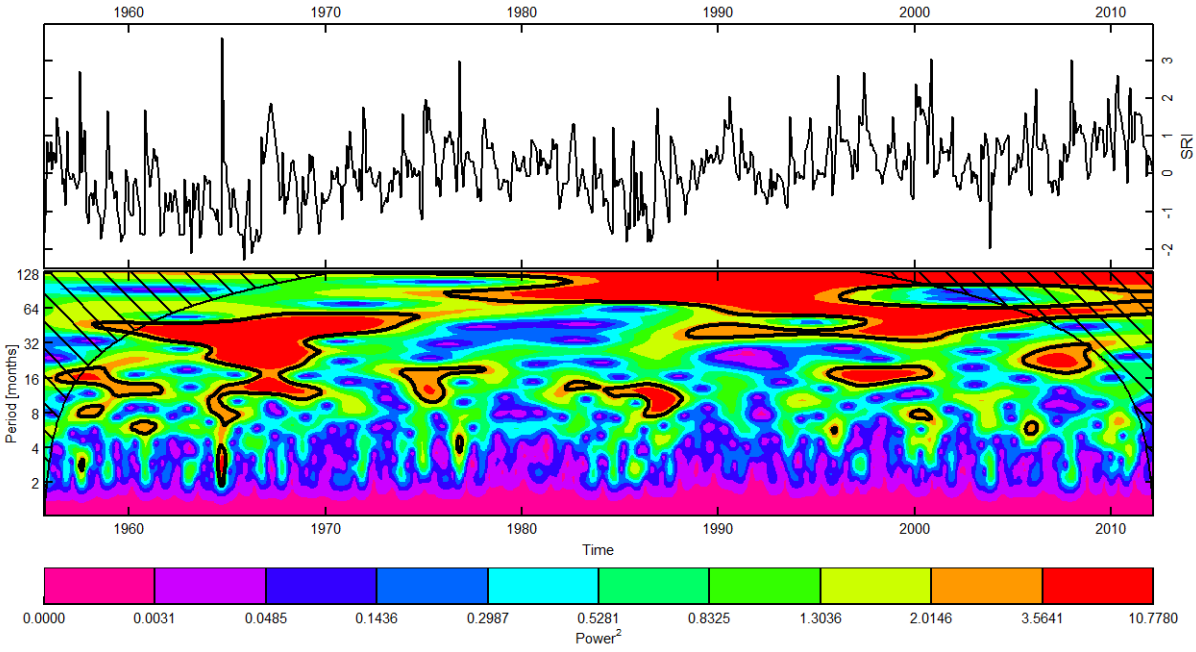

Figure 3-20: Pienaars River (Buffelspoort): standardized runoff index time series (upper) and wavelet analysis power spectra (lower).

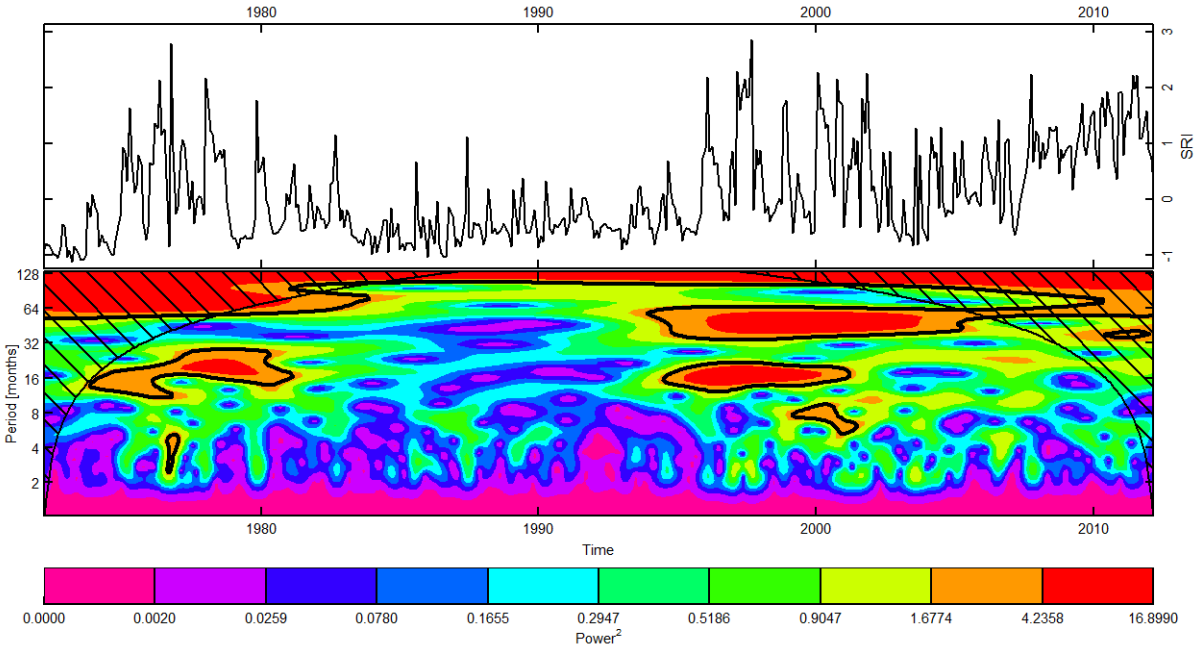

Figure 3-21: Krokodil River: standardized runoff index time series (upper) and wavelet analysis power spectra (lower).

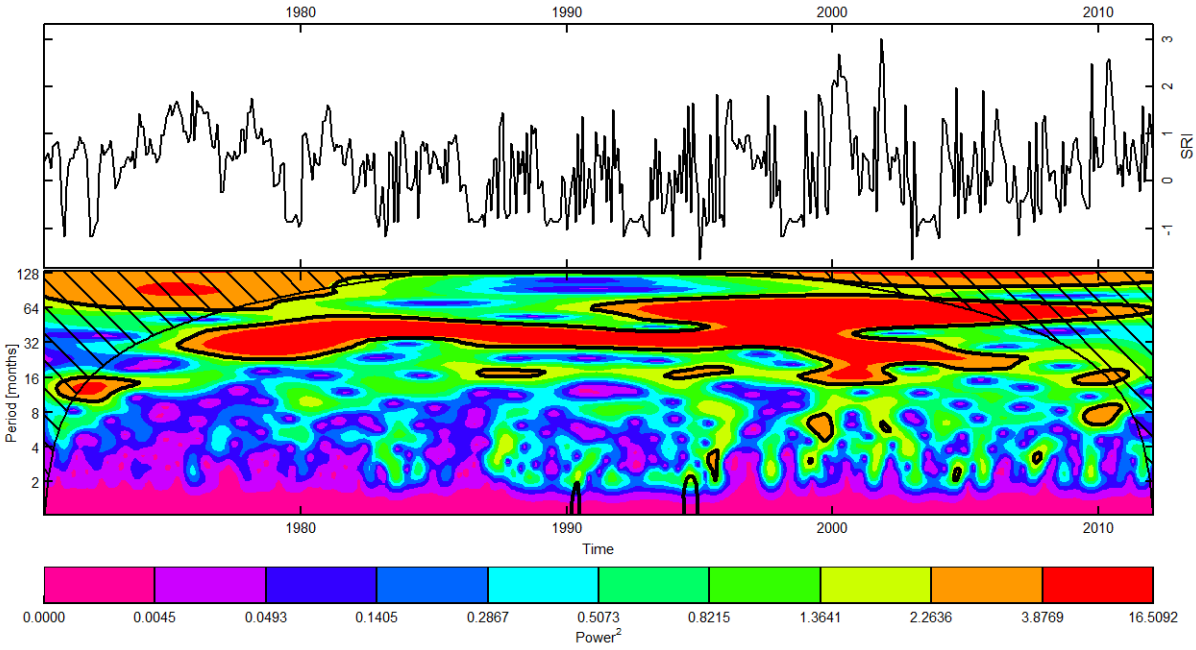

Figure 3-22: Mogalakwena River (Glen Alpine): standardized runoff index time series (upper) and wavelet analysis power spectra (lower).

3.4 WAVELET COHERENCY ANALYSIS

The relation of rainfall anomalies in Africa (here represented by SPI) and ENSO is known to be complex (Nicholson & Kim, 1997). For example, it depends on the season and also vary in different events. Here we analyse the relationship of Limpopo rainfall anomalies and runoff in selected stations in the Limpopo basin using wavelet coherence analysis.

The droughts in years 1983, 1987, 1992 and 1998 were severe droughts in South Africa (Rouault, 2005). These drought events were also coinciding with El-Nino phases (Figure 3-23 a). The wavelet coherence analysis shows, that SPI3 also shares signal properties with ENSO of periods between 2 and 4 years. Furthermore, these frequency coherencies are out of phase for the two time series. However, it is also obvious that the power of frequency coherencies is not stable and changes over time and from one event to another. For example during the El Nino phase of 1987 the SPI3 signal was closely linked and both time series show coherence power over a period range from 0.5 to 4 years. 1992 is the drought event with highest intensity in the presented SPI3 time series and shows a special wavelet coherence pattern. The coherence period is narrowed to a distinct band of 4 years, which is probably caused by little noise in the SPI3 signal during that event.

In Figure 3-23 we present the wavelet coherence with the Oceanic Nino Index (ONI). With other ENSO indices the coherence patterns generally are very similar (see appendix 6.1.3). Sometimes they also complement each other. For example, the NINO 1.2 region has a very similar wavelet coherence pattern, but there are obvious differences in the band between 4 and 5 years. In this band, ONI has no power earlier than 1995 and later than 1995 this gap is narrowing. On the other hand, NINO 1.2 has power in the 4 to 5 years band earlier than 1995, which disappears thereafter. This can serve as a hint that different sea surface regions can complement each other in explaining the variation in Limpopo rainfall.

In addition to analysis of reanalysis precipitation data, we present single station runoff analysis. On the one hand this provides the analysis of longer time series and on the other hand this highlights what signal coherence patterns are still present in the runoff signal.

It is common to most wavelet coherence power spectra of runoff stations and climate anomaly indexes to have more segregated patterns than with the reanalysis precipitation presented above. Consistent bands of frequency coherence with ONI – if present at all – are often interrupted during the period of 1985 to 1995 (Figure 3-25, Figure 3-26 and Figure 3-27). However, many stations retain a common power in a band of periods longer than 16 years.

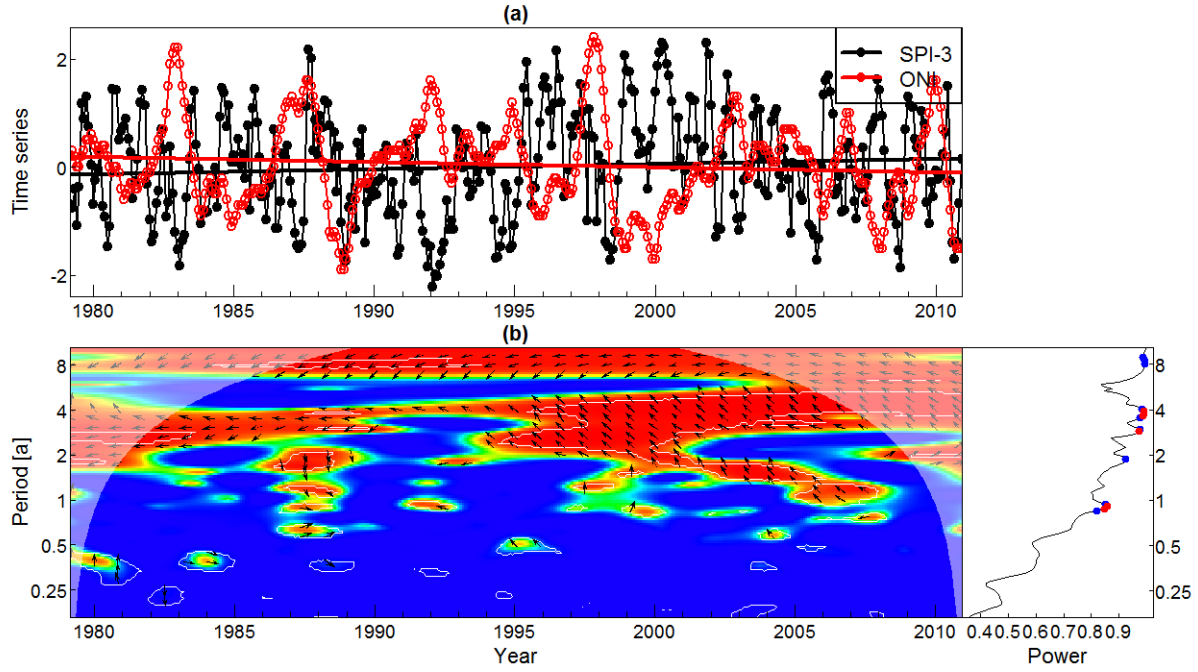

Figure 3-23: 3-month Standardized precipitation index (SPI-3) and Oceanic NINO Index (ONI) time series (upper) and wavelet coherence plot (lower). Arrow directions indicate the phase relationship: in phase (right), antiphase (left), red leading black (down), black leading red (up).

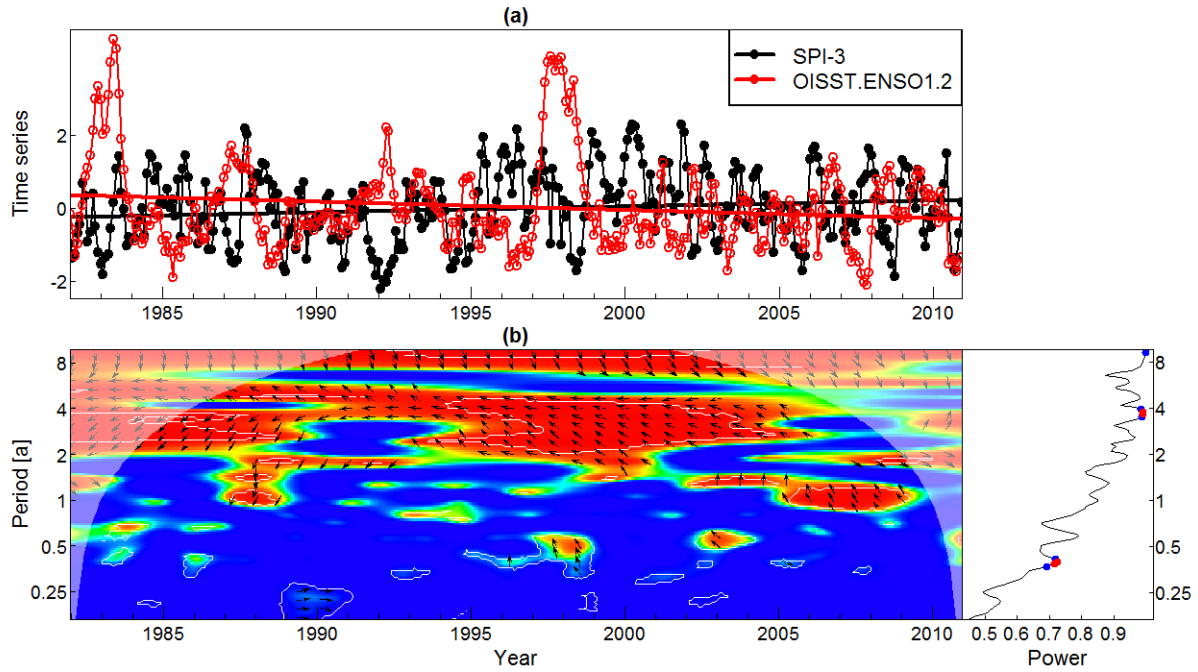

Figure 3-24: 3-month Standardized precipitation index (SPI-3) and NINO1.2 region (OISST2) time series (upper) and wavelet coherence plot (lower). Arrow directions indicate the phase relationship: in phase (right), antiphase (left), red leading black (down), black leading red (up).

The Pienaars River runoff has strong power on a band of approx. 8 years with the ONI index (Figure 3-25). During the 1985 to 1995 period the coherence is broken. Several events show coherence with ONI in shorter periods of 4 years. These events are in the late 70ies and late 90ies. The Krokodil River (Figure 3-26) shows the same property in the late 90ies with

coherence power over a wide range of periods. In the Krokodil River the runoff during 1985 and 1995 is greatly reduced, which coincides with an almost complete absence of wavelet coherence power. However, this might be caused by general reduction of power in the SRI signal during that period (see also Figure 3-21). In contrast to the other stations presented here there is no power on 16 years period coherence periods. The Mogalakwena River (Figure 3-27) - on the other hand - shows all these features: power on longer period, high power in late 90ies. It also has coherence power in lower periods during the early 80ies.

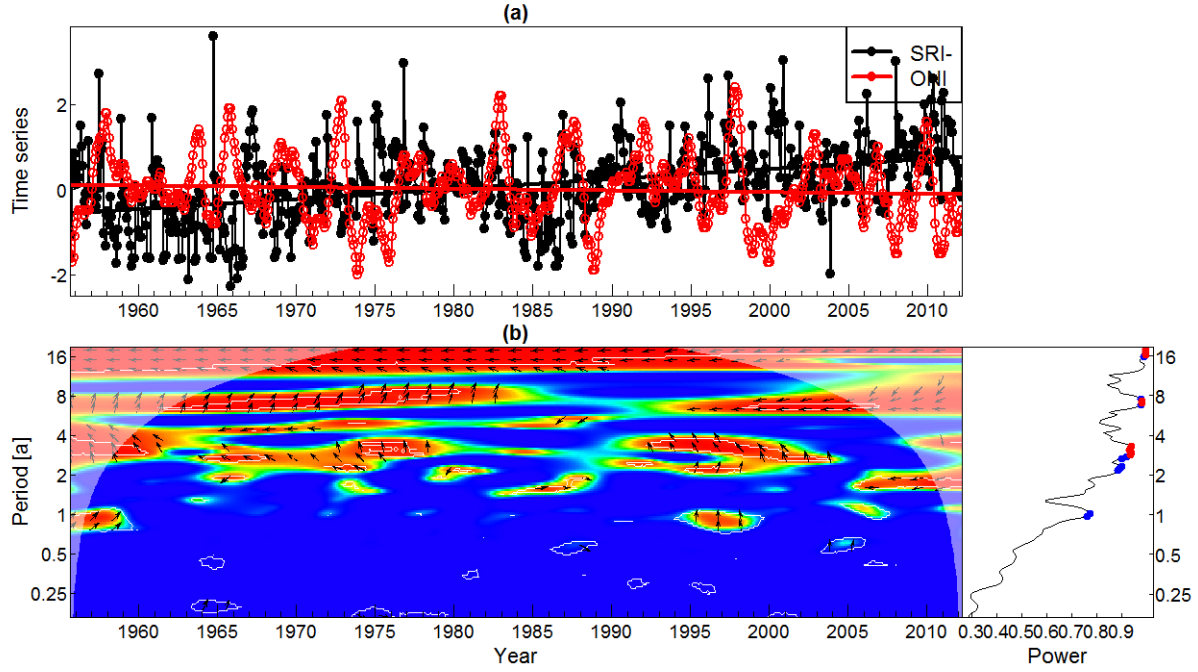

Figure 3-25: Pienaars River (Buffelspoort): 1-month Standardized Runoff Index (SRI) and Oceanic NINO Index (ONI) time series (upper) and wavelet coherence plot (lower). Arrow directions indicate the phase relationship: in phase (right), antiphase (left), red leading black (down), black leading red (up).

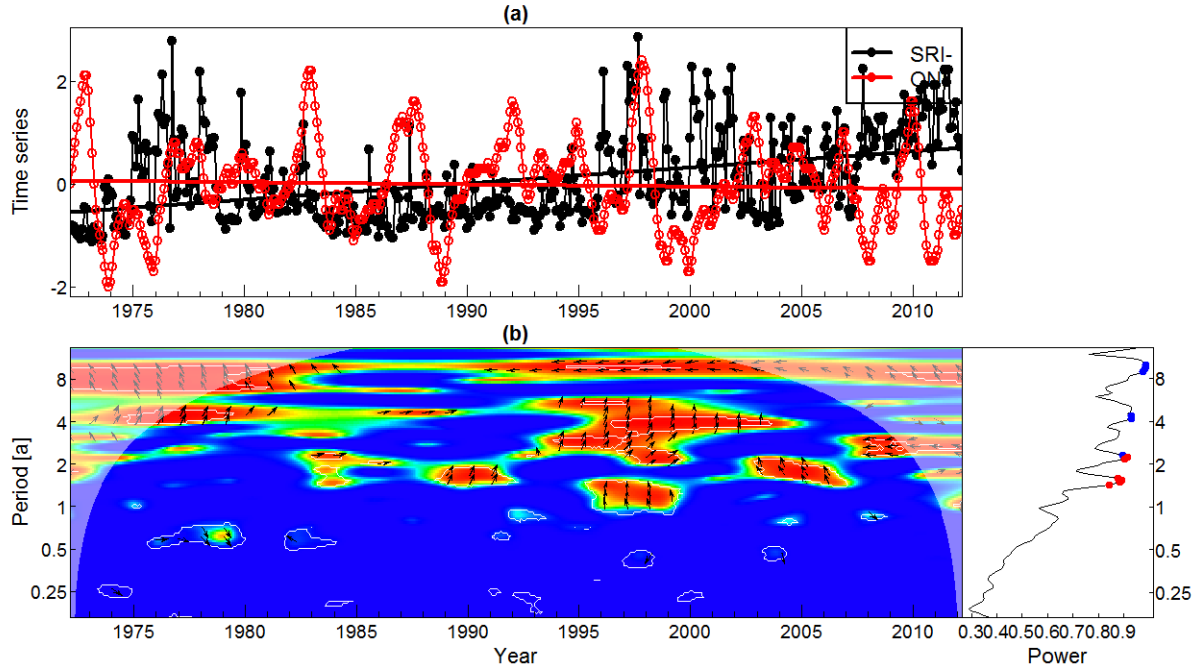

Figure 3-26 Krokodil River: 1-month Standardized Runoff Index (SRI) and Oceanic NINO Index (ONI) time series (upper) and wavelet coherence plot (lower). Arrow directions indicate the phase relationship: in phase (right), antiphase (left), red leading black (down), black leading red (up).

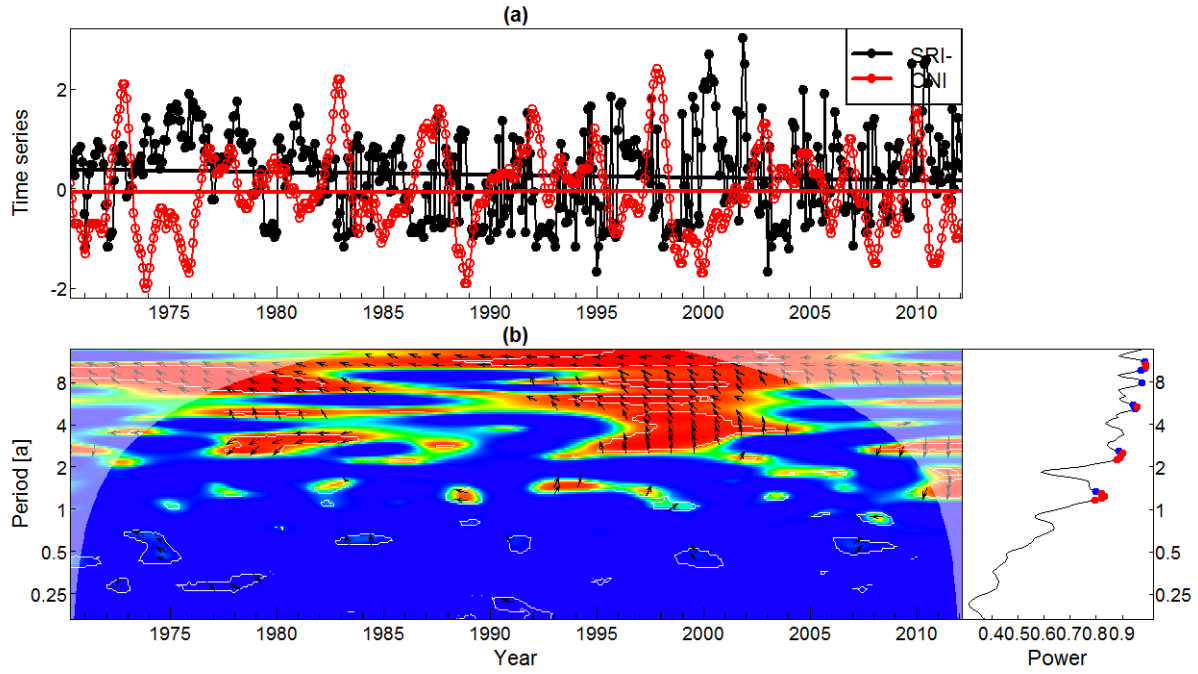

Figure 3-27: Mogalakwena River (Glen Alpine): 1-month Standardized Runoff Index (SRI) and Oceanic NINO Index (ONI) time series (upper) and wavelet coherence plot (lower). Arrow directions indicate the phase relationship: in phase (right), antiphase (left), red leading black (down), black leading red (up).

The Chokwe station in Mozambique has a long record but some short periods of the SRI had to be interpolated using zeros in order to perform wavelet coherence analysis (Figure 3-28). We estimate that this has little effect on the presented results. The Chokwe station SRI has

high power on the 16 years band. During the 70ies it also exhibits high power over a wide range of periods between 2 and 5 years. In the period between 1985 and 1995 the coherence band is changed and narrowed, but single events still show coherent signal properties. This is in strong contrast to the observation made for example with the Krokodil River which shows very little coherence during that period.

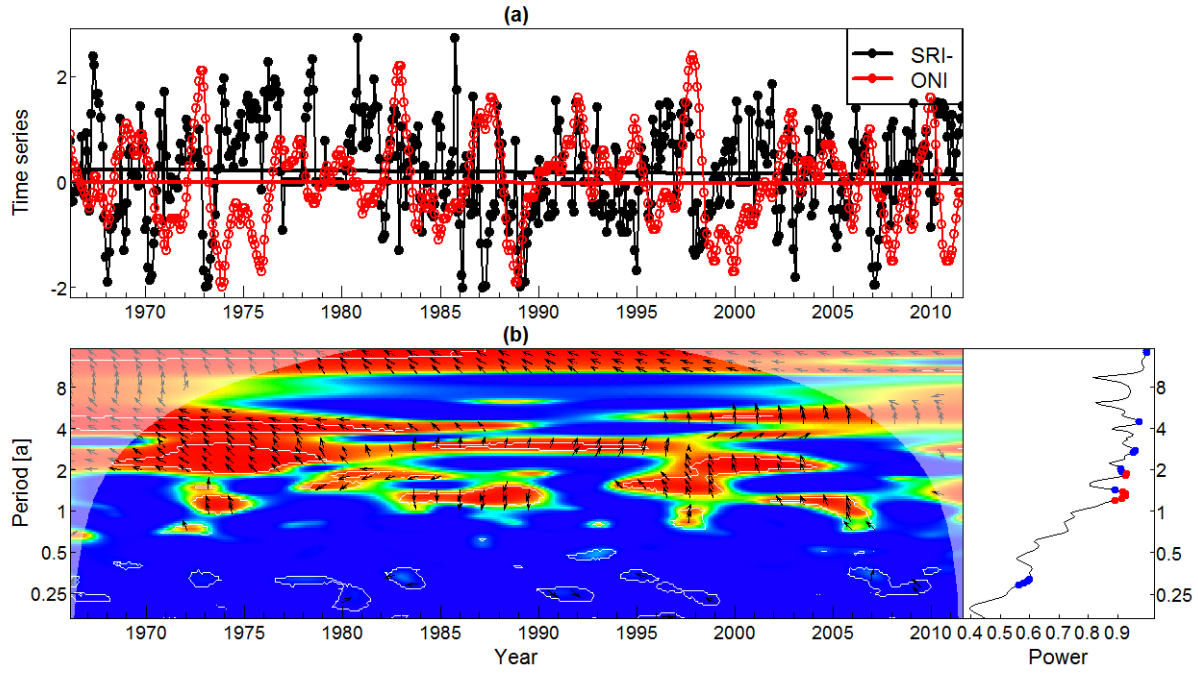

Figure 3-28: Limpopo River (Chokwe, Mozambique): 1-month Standardized Runoff Index (SRI) and Oceanic NINO Index (ONI) time series (upper) and wavelet coherence plot (lower). The SRI time series had to be interpolated using zeros to create a complete record. Arrow directions indicate the phase relationship: in phase (right), antiphase (left), red leading black (down), black leading red (up).

4. CONCLUSIONS

In this report we present the analysis of drought variability in meteorological and hydrological data. Drought was represented by standardised time series of precipitation and runoff to represent anomalies. The analysis investigates the complexity that characterises the relationship of drought in the Limpopo basin with climate anomalies. Since these atmospheric anomalies are known to cause drought they are at the heart of various statistical methods of rainfall prediction. This work serves as preliminary analysis to assess the complexity of drought variability. Drought variability was accessed here both in the spatial as well in the temporal domain. The multitude of analysis methods provides a wide view on drought variability.

We showed SPEI is able to capture the impact on vegetation status which makes it generally useful for drought monitoring and underlines the usefulness for drought variability analysis. We presented examples of independent data sets that indicate that it is possible to develop a drought threshold for an index like SPEI. However, the strength of the relationship depends on local factors, which need further investigations if these need to be understood. For example, we expect that vegetation type and water management have great influence on the vegetation's sensitivity to rainfall anomalies.

The application of principal component analysis aimed at understanding spatial variability. Spatial precipitation anomaly fields were dissembled to dominating patterns. The dominating spatial patterns in rainfall anomalies can be reduced to five patterns which account for 74 % of the total variation. They were analysed in an attempt to relate them with atmospheric anomalies and sea surface temperature (SST) anomalies. The results support two conclusions: First, the dominating spatial patterns cannot be linked to specific climate anomalies. Every drought event very likely is a unique combination of many factors of influence. Second, promising regions of SST were identified, which are potential predictors, because they exhibit lead times for the Limpopo region precipitation. Consequently they may be used for statistical drought prediction.

The temporal variability was analysed based on meteorological and hydrological data. The analysis of the Limpopo wide SPI provided a large scale of temporal variability. The signals available for runoff and precipitation showed inconsistent properties. The analysis of runoff added an impression of how variability can change in subcatchments. Frequencies present in the signals had only little consistency in time and space. The period 1985 to 1995 is marked by strong changes in precipitation total and signal properties. In contrast to analyses by (Mwale et al., 2007) we were not able to find evidence that this change is related to ENSO. Some stations seemed to be disconnected of the ENSO during this period. This strongly

differed between runoff stations, which indicates that every subcatchment has local factors that affect rainfall anomaly and some regions can be affected more by an anomaly and others less.

In combination the two analyses, a picture of complex spatial and temporal variability and relationships evolves. Prediction models have to able to deal with nonlinear and interacting relationships with climate anomalies. Neither could certain anomalies be associated with spatial patterns nor could certain anomalies be isolated. It is very likely that every drought event is caused by a unique combination of different atmospheric anomalies.

In the presented analysis correlation and wavelet analysis were important applied methods. Thus, it is necessary to add a critical note regarding the interpretation: Correlations between variables do not imply a causal link. Rather, causally linked variables are likely to be correlated. Hence, correlation can only serve as an indication of a potential causal and above all linear link. The same is valid for wavelet coherence analysis. Neither wavelet coherences imply a causally linked relationship, nor single event wise coherences. They only highlight signal similarities in frequency space. This can only be taken as an indicator for relationships between variables.

5. REFERENCES

Compagnucci, R. H., & Richman, M. B. (2008). Can principal component analysis provide atmospheric circulation or teleconnection patterns ? *International Journal of Climatology*, *726*(July 2007), 703–726. doi:10.1002/joc

Dee, D. P., Uppala, S. M., Simmons, a. J., Berrisford, P., Poli, P., Kobayashi, S., Andrae, U., et al. (2011). The ERA-Interim reanalysis: configuration and performance of the data assimilation system. *Quarterly Journal of the Royal Meteorological Society*, *137*(656), 553–597. doi:10.1002/qj.828

Grinsted, A., Moore, J. C., & Jevrejeva, S. (2004). Application of the cross wavelet transform and wavelet coherence to geophysical time series. *Nonlinear Processes in Geophysics*, *11*, 561–566.

Landman, W. A., & Mason, S. J. (1999). OPERATIONAL LONG-LEAD PREDICTION OF SOUTH AFRICAN RAINFALL USING CANONICAL CORRELATION ANALYSIS. *INTERNATIONAL JOURNAL OF CLIMATOLOGY*, *19*, 1073–1090.

Mwale, D., Gan, T. Y., Shen, S. S. P., Shu, T. T., & Kim, K.-M. (2007). Wavelet empirical orthogonal functions of space-time-frequency regimes and predictability of southern Africa summer rainfall. *Journal of Hydrologic Engineering*, 513 – 523. doi:10.1061/(ASCE) 1084-0699(2007)12:5(513)

Mwale, D., Yew Gan, T., & Shen, S. S. P. (2004). A new analysis of variability and predictability of seasonal rainfall of central southern Africa for 1950-94. *International Journal of Climatology*, *24*(12), 1509–1530. doi:10.1002/joc.1062

Nicholson, S. E., & Kim, J. (1997). The relationship of the El Nino-Southern oscillation to African rainfall. *International Journal of Climatology*, *17*(2), 117–135. Retrieved from http://dweb.met.fsu.edu/people/nicholson/papers/elnino.pdf

Overland, E. J., & Preisendorfer, R. W. (1982). A Significance Test for Principal Components Applied to a Cyclone Climatology. *Monthly Weather Review*, *110*(1), 1 – 4.

R Development Core Team. (2011). R: A language and environment for statistical computing. Vienna: R Foundation for Statistical Computing. Retrieved from http://www.r-project.org/

Rouault, M. (2005). Intensity and spatial extent of droughts in southern Africa. *Geophysical Research Letters*, *32*(15), 2–5. doi:10.1029/2005GL022436

Shukla, S., & Wood, A. W. (2008). Use of a standardized runoff index for characterizing hydrologic drought. *Geophysical Research Letters*, *35*(2), 1–7. doi:10.1029/2007GL032487

Torrence, C., & Compo, G. P. (1998). A practical guide to wavelet analysis. *Bulletin of the American*, *79*(1), 61 – 78.

Vicente-Serrano, S. M., Beguería, S., & López-Moreno, J. I. (2010). A Multiscalar Drought Index Sensitive to Global Warming: The Standardized Precipitation Evapotranspiration Index. *Journal of Climate*, *23*(7), 1696–1718. doi:10.1175/2009JCLI2909.1

Özger, M., Mishra, A. K., & Singh, V. P. (2012). Long Lead Time Drought Forecasting Using a Wavelet and Fuzzy Logic Combination Model: A Case Study in Texas. *Journal of Hydrometeorology*, *13*(1), 284–297. doi:10.1175/JHM-D-10-05007.1

6. APPENDICES

6.1 APPENDIX A: ANALYSIS RESULTS

6.1.1 Principal component analysis and Sea Surface Temperature correlations

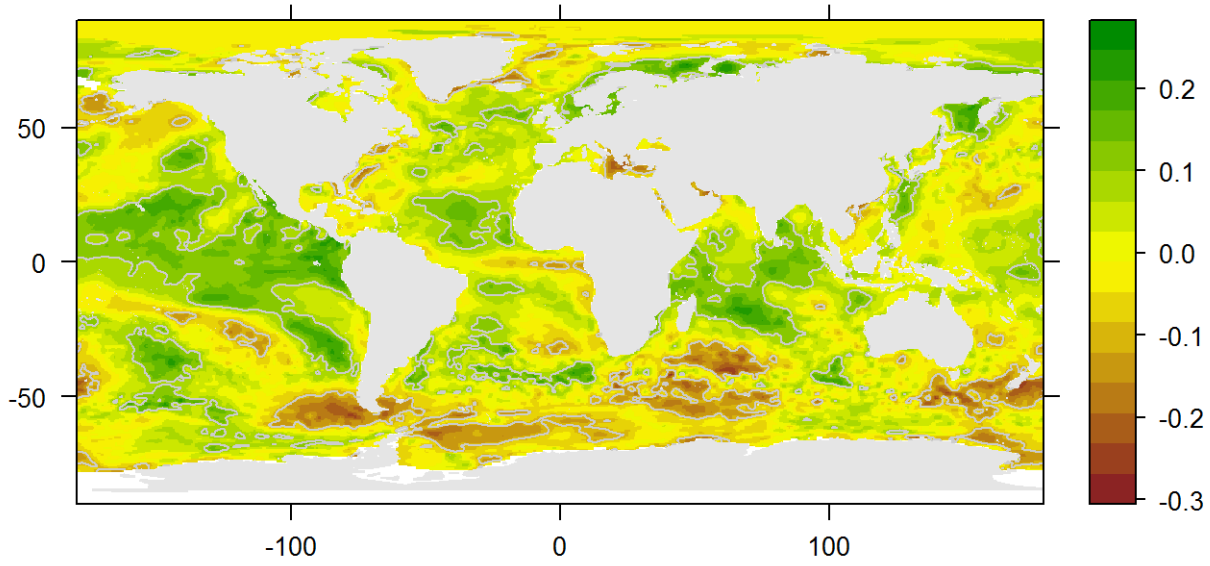

Figure 6-1: ERA-Interim SST anomaly correlation with **PC1** loadings of SPEI in 3 month aggregation (Limpopo basin). Grey contours denote 0.95 level of correlation significance.

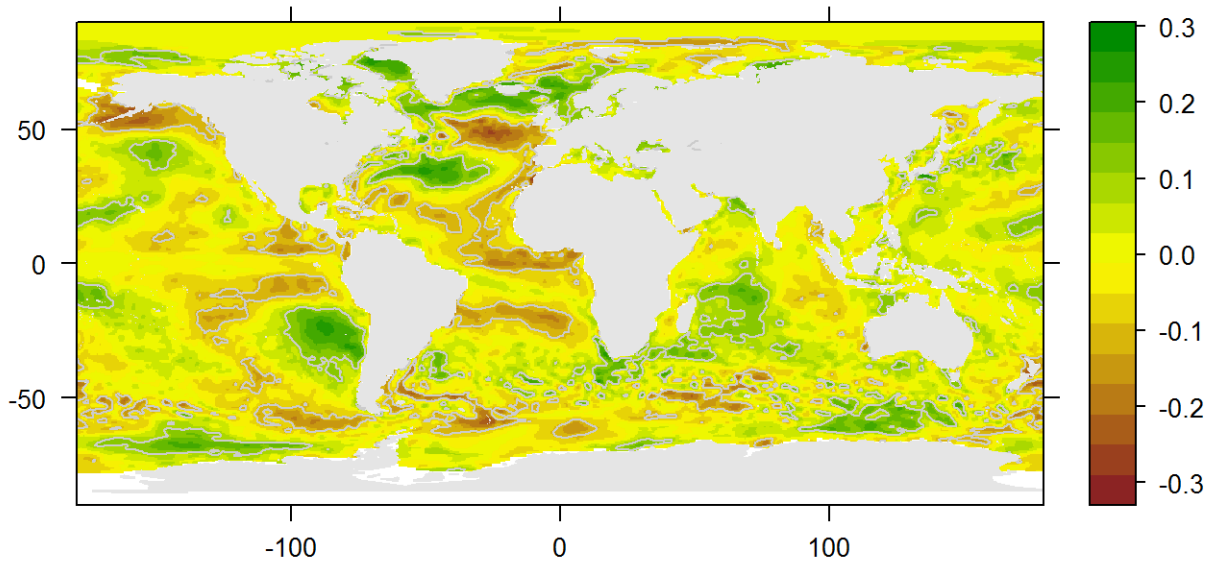

Figure 6-2: ERA-Interim SST anomaly correlation with **PC2** loadings of SPEI in 3 month aggregation (Limpopo basin). Grey contours denote 0.95 level of correlation significance.

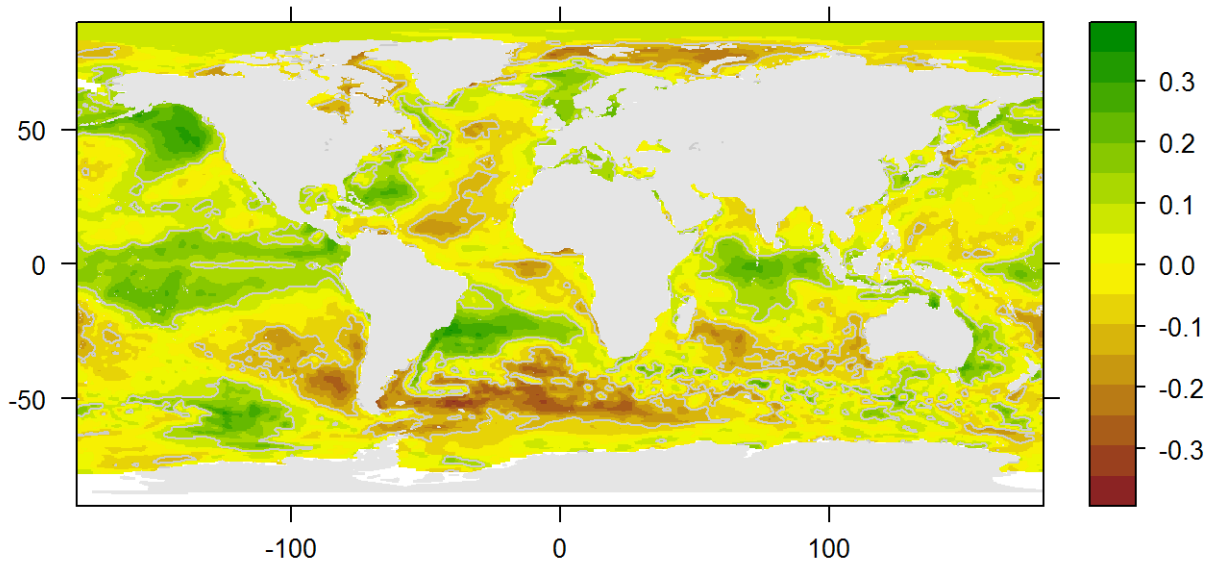

Figure 6-3: ERA-Interim SST anomaly correlation with **PC3** loadings of SPEI in 3 month aggregation (Limpopo basin). Grey contours denote 0.95 level of correlation significance.

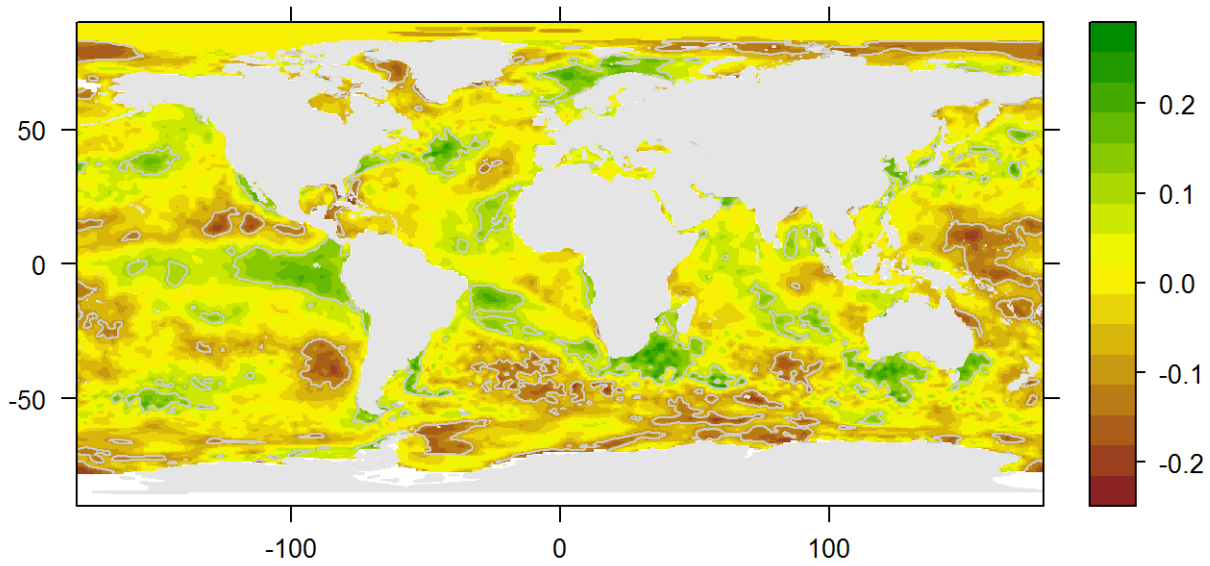

Figure 6-4: ERA-Interim SST anomaly correlation with **PC4** loadings of SPEI in 3 month aggregation (Limpopo basin). Grey contours denote 0.95 level of correlation significance.

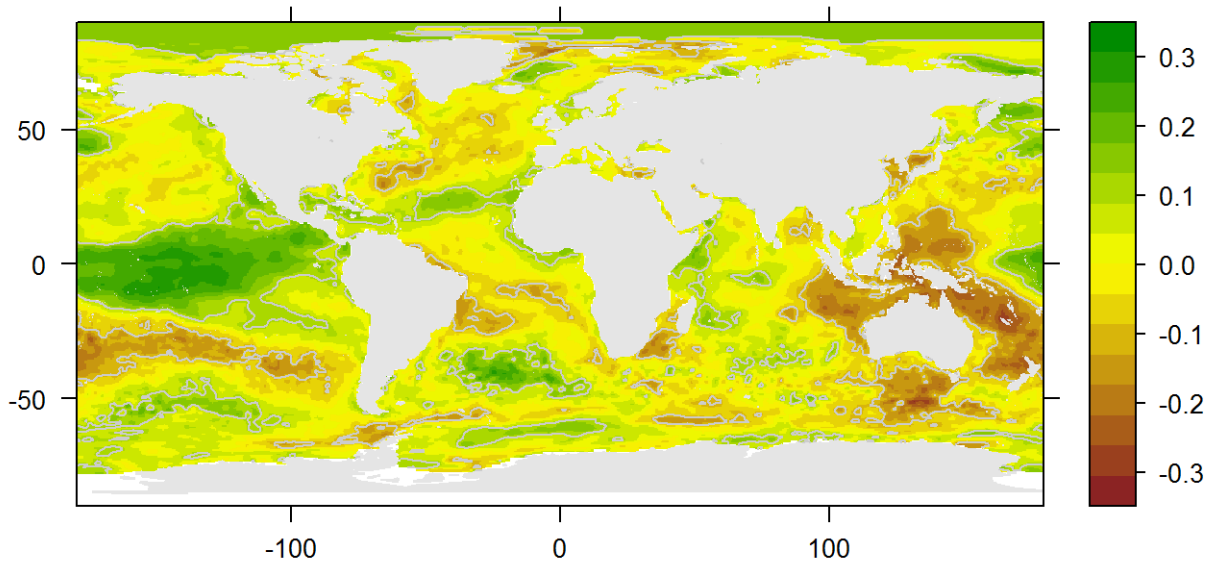

Figure 6-5: ERA-Interim SST anomaly correlation with **PC5** loadings of SPEI in 3 month aggregation (Limpopo basin). Grey contours denote 0.95 level of correlation significance.

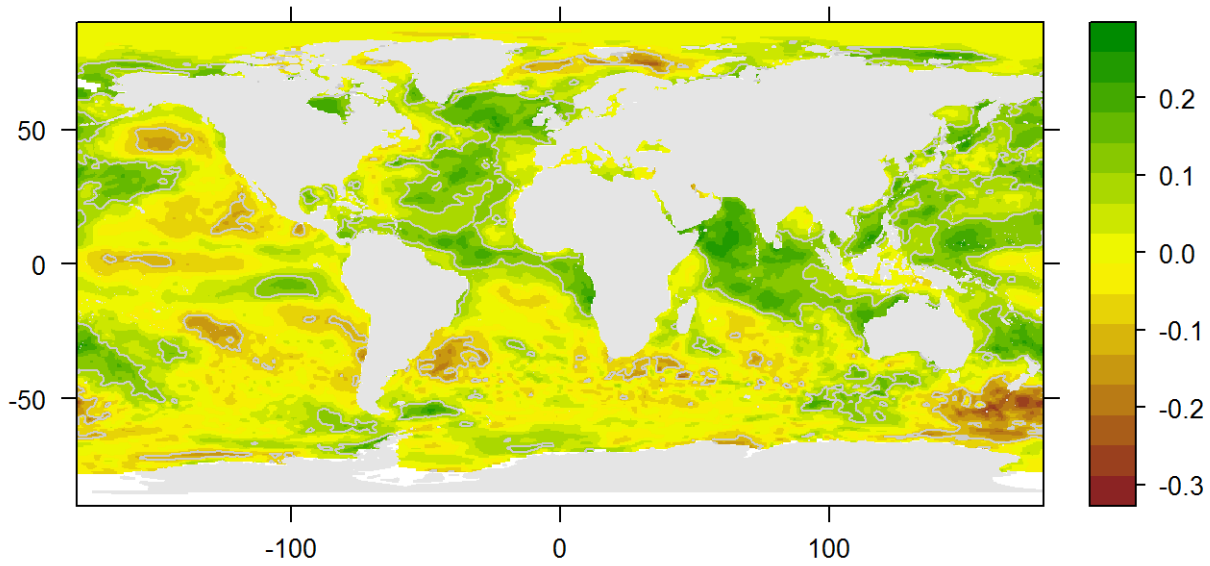

Figure 6-6: ERA-Interim SST anomaly correlation with **PC6** loadings of SPEI in 3 month aggregation (Limpopo basin). Grey contours denote 0.95 level of correlation significance.

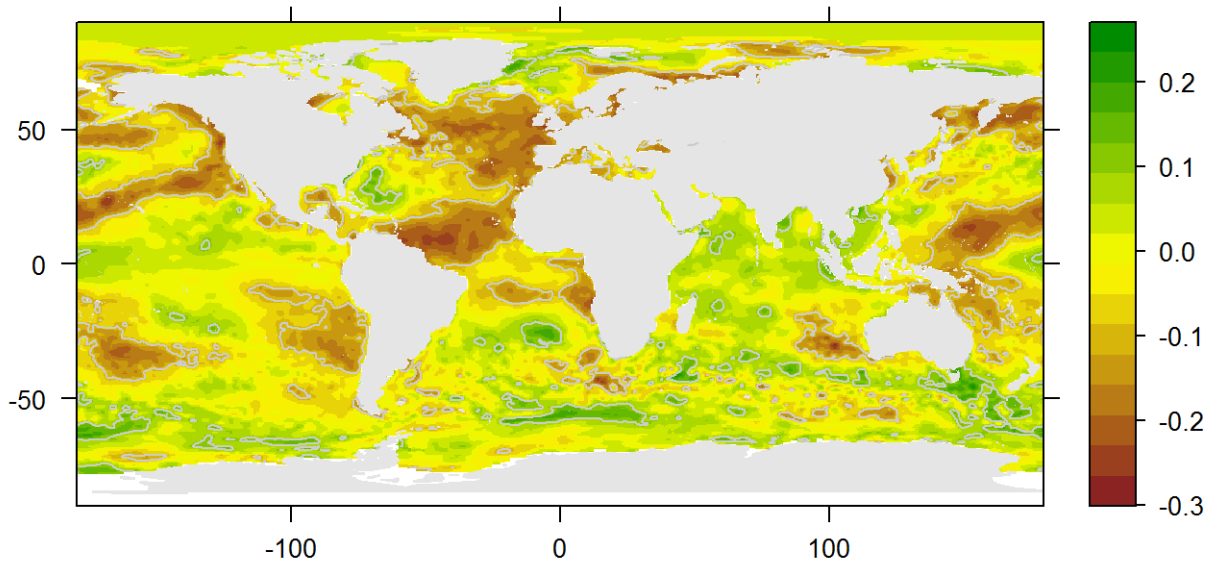

Figure 6-7: ERA-Interim SST anomaly correlation with **PC7** loadings of SPEI in 3 month aggregation (Limpopo basin). Grey contours denote 0.95 level of correlation significance.

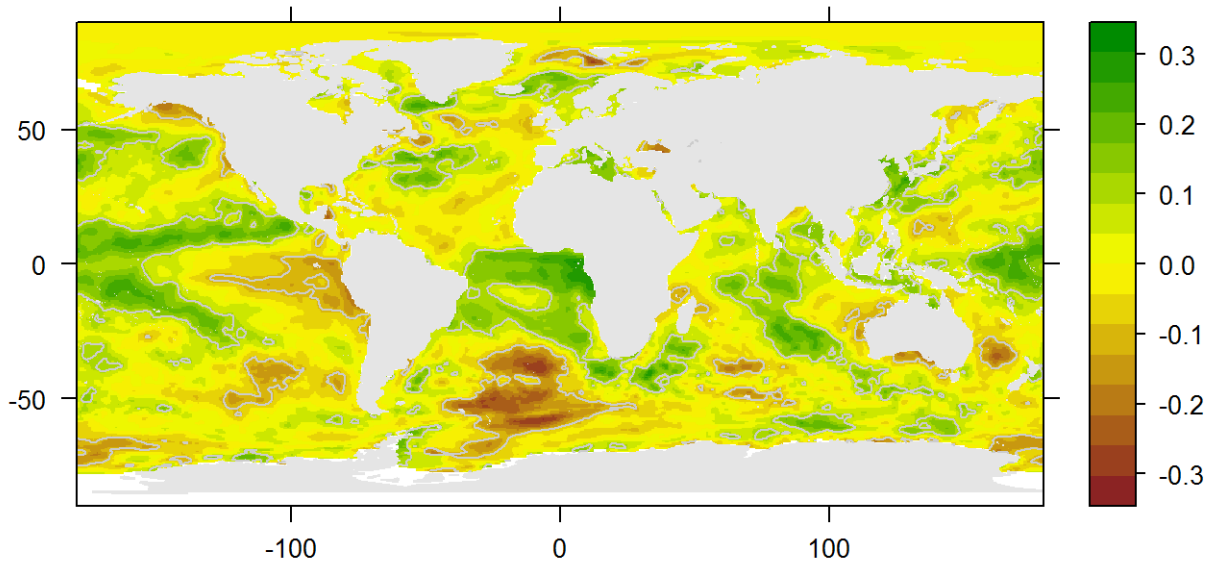

Figure 6-8: ERA-Interim SST anomaly correlation with **PC8** loadings of SPEI in 3 month aggregation (Limpopo basin). Grey contours denote 0.95 level of correlation significance.

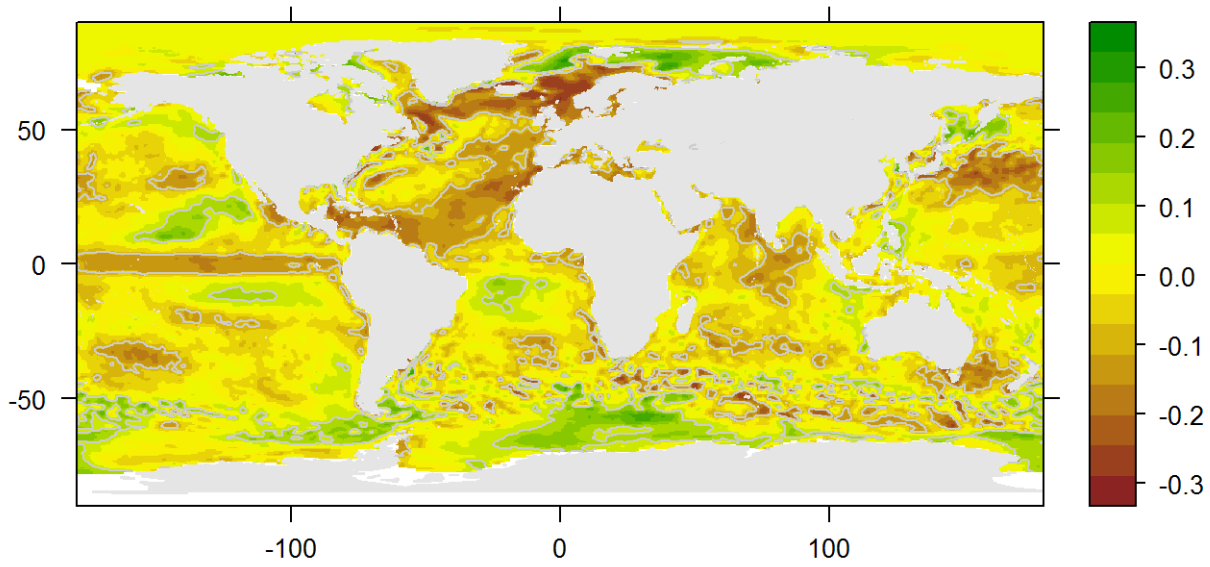

Figure 6-9: ERA-Interim SST anomaly correlation with **PC9** loadings of SPEI in 3 month aggregation (Limpopo basin). Grey contours denote 0.95 level of correlation significance.

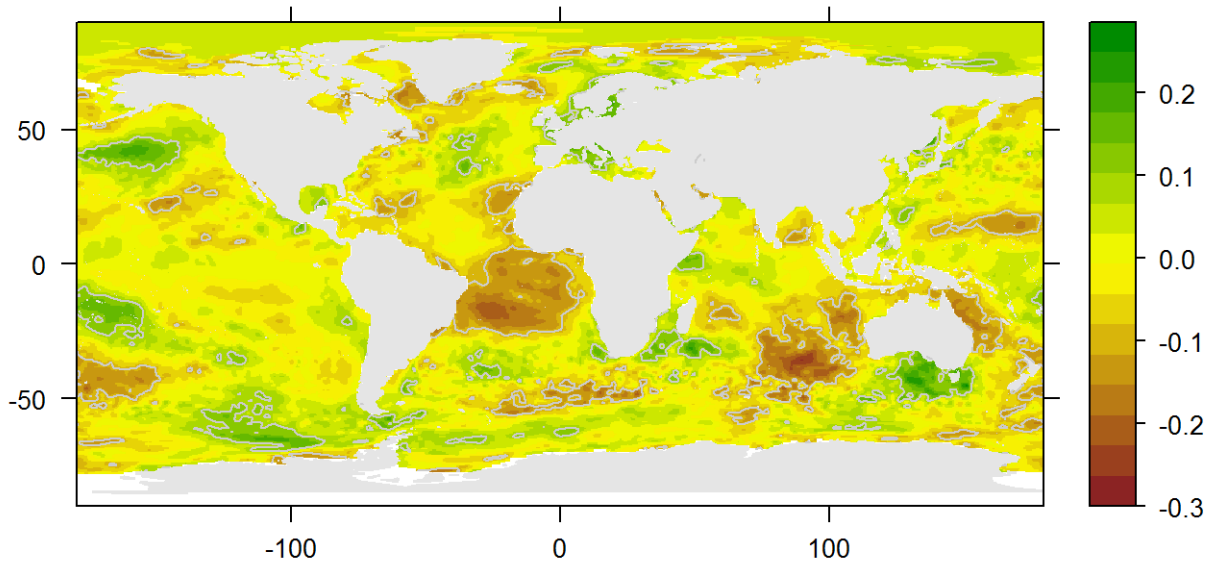

Figure 6-10: ERA-Interim SST anomaly correlation with **PC10** loadings of SPEI in 3 month aggregation (Limpopo basin). Grey contours denote 0.95 level of correlation significance.

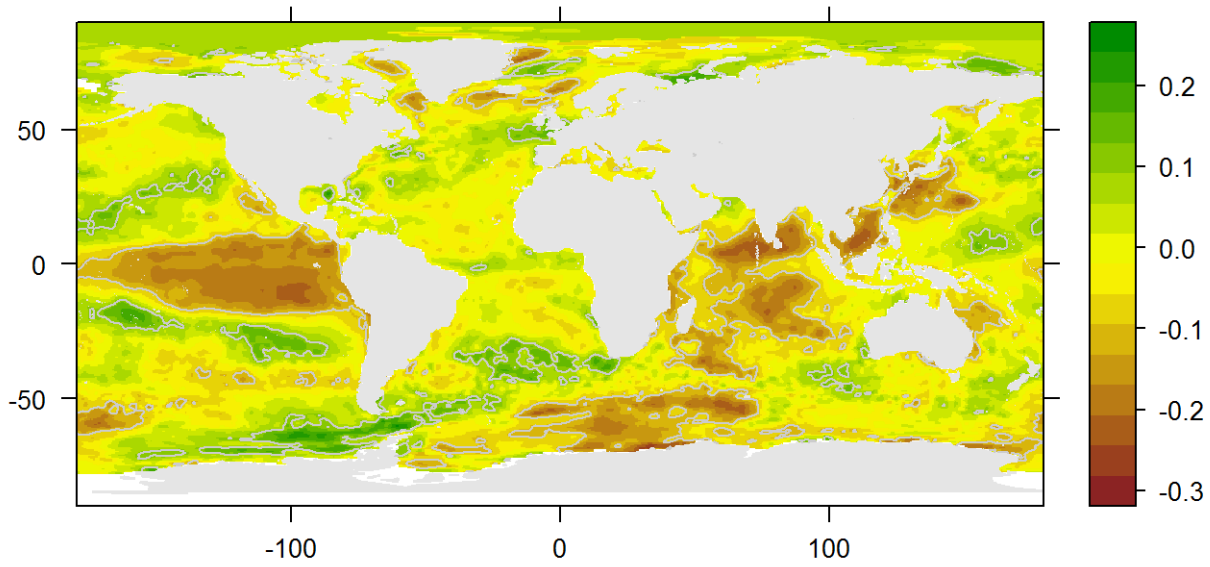

Figure 6-11: ERA-Interim SST anomaly correlation with **PC11** loadings of SPEI in 3 month aggregation (Limpopo basin). Grey contours denote 0.95 level of correlation significance.

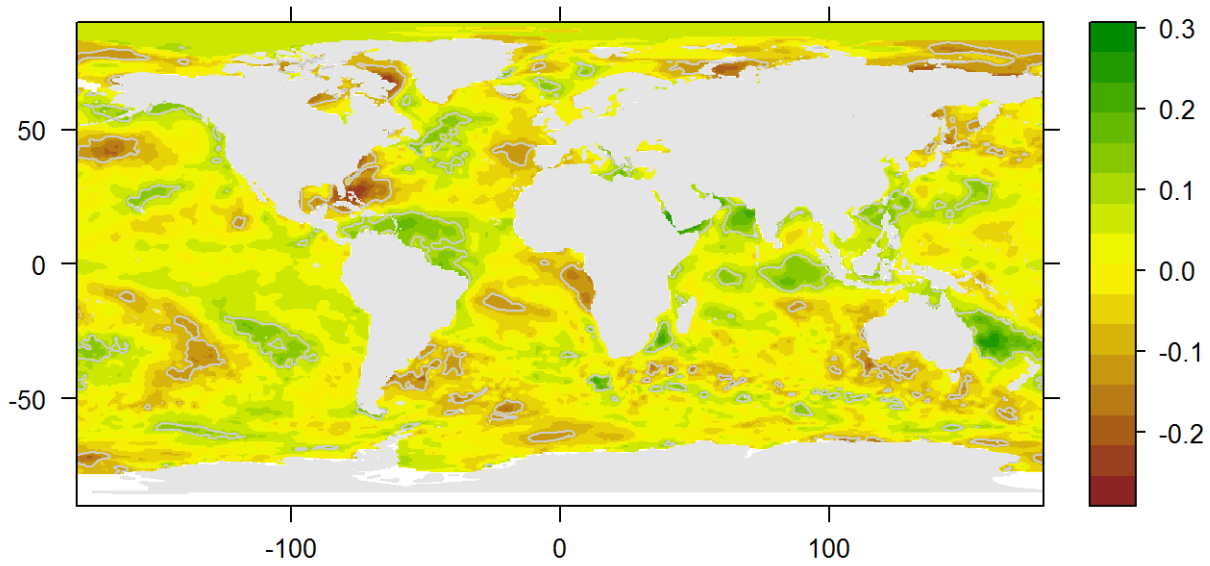

Figure 6-12: ERA-Interim SST anomaly correlation with **PC12** loadings of SPEI in 3 month aggregation (Limpopo basin). Grey contours denote 0.95 level of correlation significance.

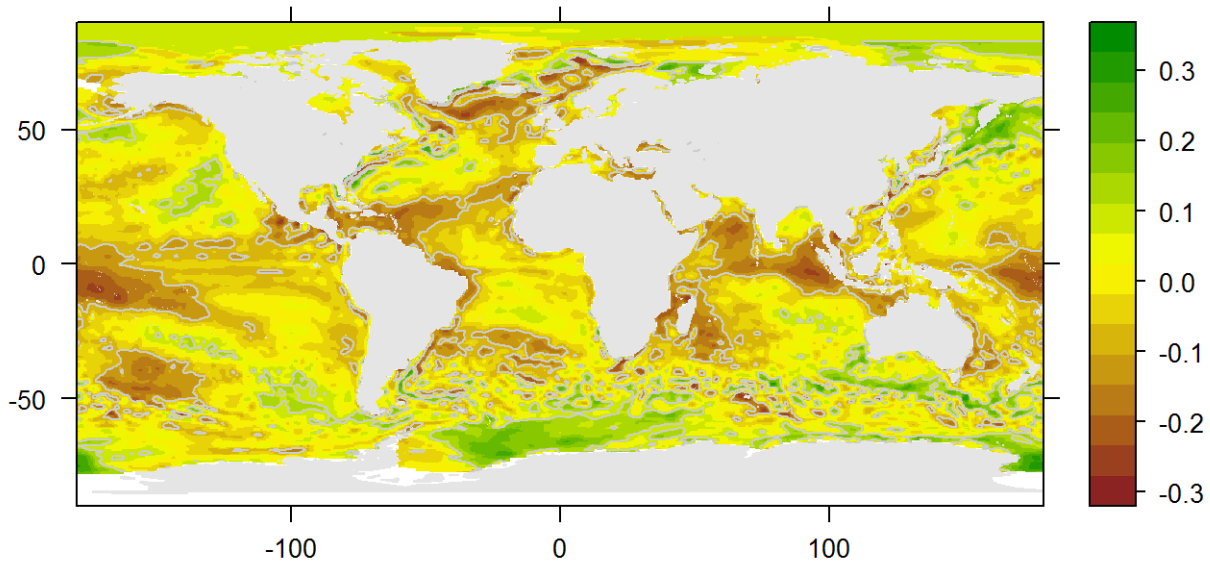

Figure 6-13: ERA-Interim SST anomaly correlation with **PC13** loadings of SPEI in 3 month aggregation (Limpopo basin). Grey contours denote 0.95 level of correlation significance.

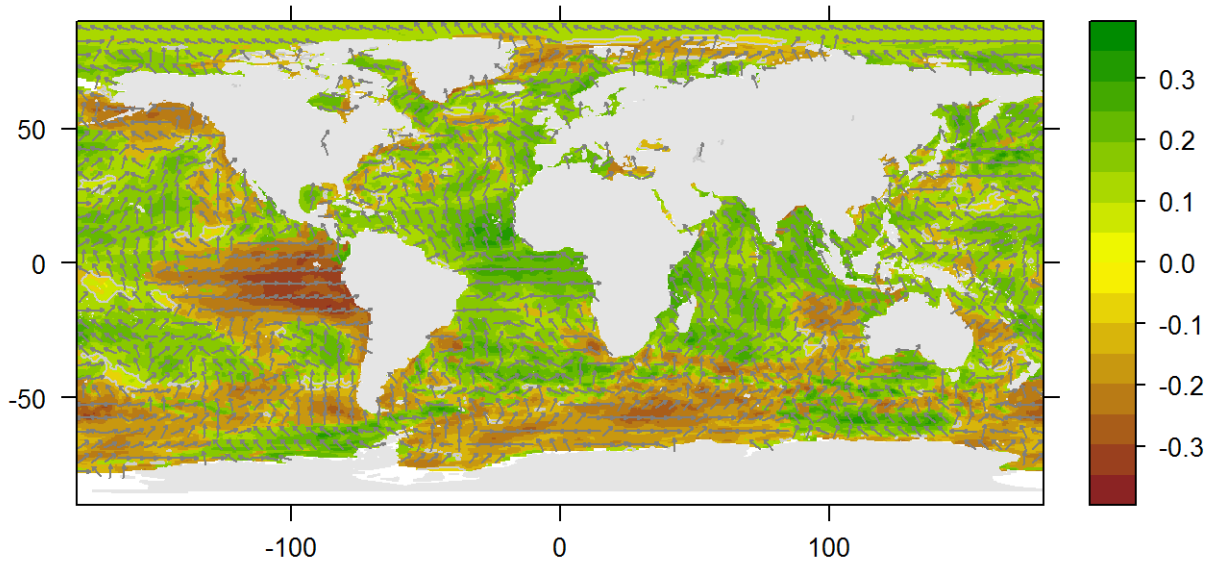

Figure 6-14: ERA-Interim SST anomaly crosscorrelation with **PC1** loadings of SPEI in 3 month aggregation (Limpopo basin). The maximal correlation within a lag of 2 years is shown. Arrows pointing left indicate negative lags. Grey contours denote 0.95 level of correlation significance.

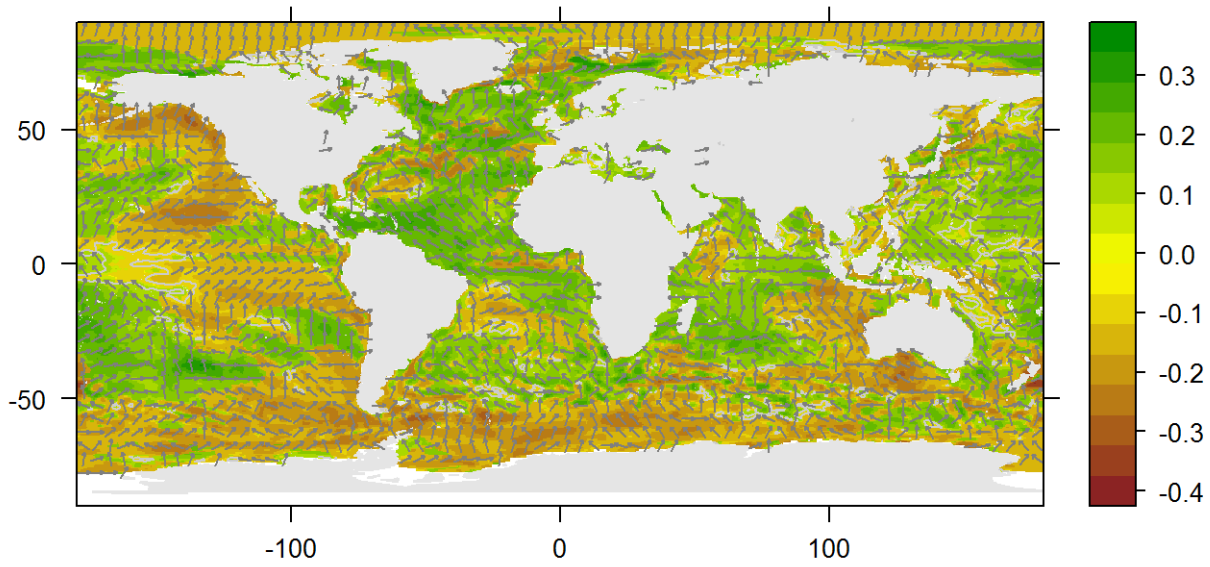

Figure 6-15: ERA-Interim SST anomaly crosscorrelation with **PC2** loadings of SPEI in 3 month aggregation (Limpopo basin). The maximal correlation within a lag of 2 years is shown. Arrows pointing left indicate negative lags. Grey contours denote 0.95 level of correlation significance.

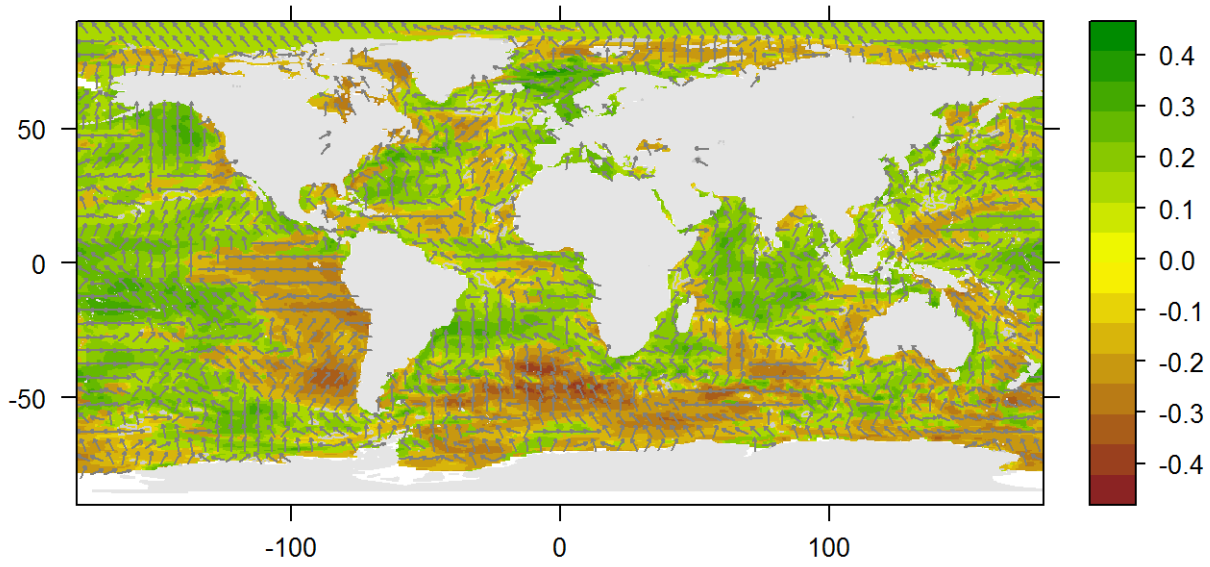

Figure 6-16: ERA-Interim SST anomaly crosscorrelation with **PC3** loadings of SPEI in 3 month aggregation (Limpopo basin). The maximal correlation within a lag of 2 years is shown. Arrows pointing left indicate negative lags. Grey contours denote 0.95 level of correlation significance.

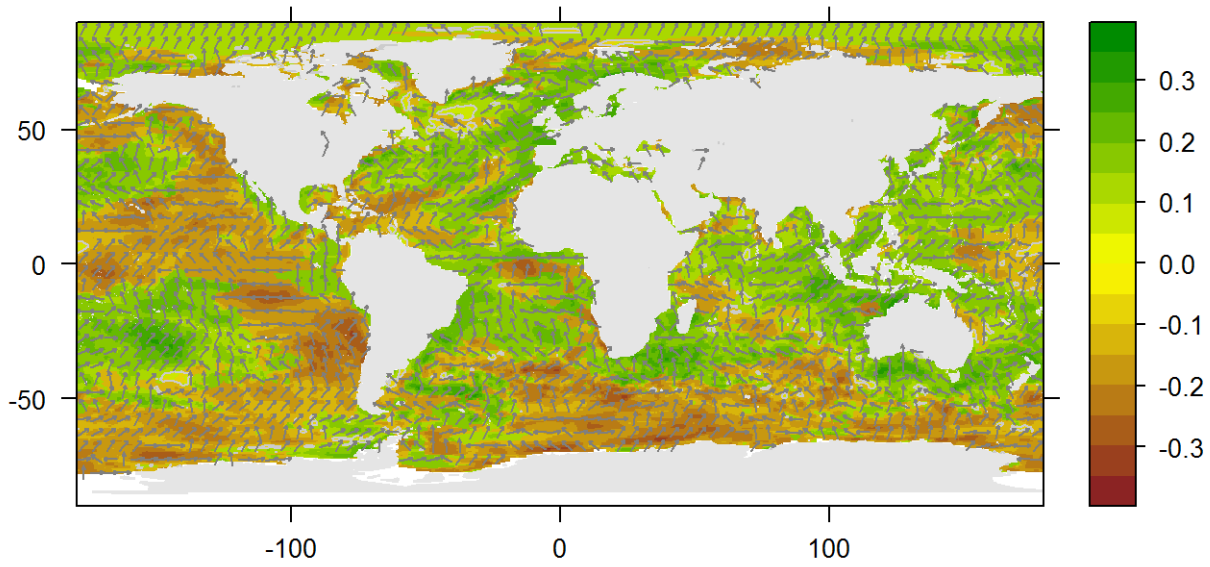

Figure 6-17: ERA-Interim SST anomaly crosscorrelation with **PC4** loadings of SPEI in 3 month aggregation (Limpopo basin). The maximal correlation within a lag of 2 years is shown. Arrows pointing left indicate negative lags. Grey contours denote 0.95 level of correlation significance.

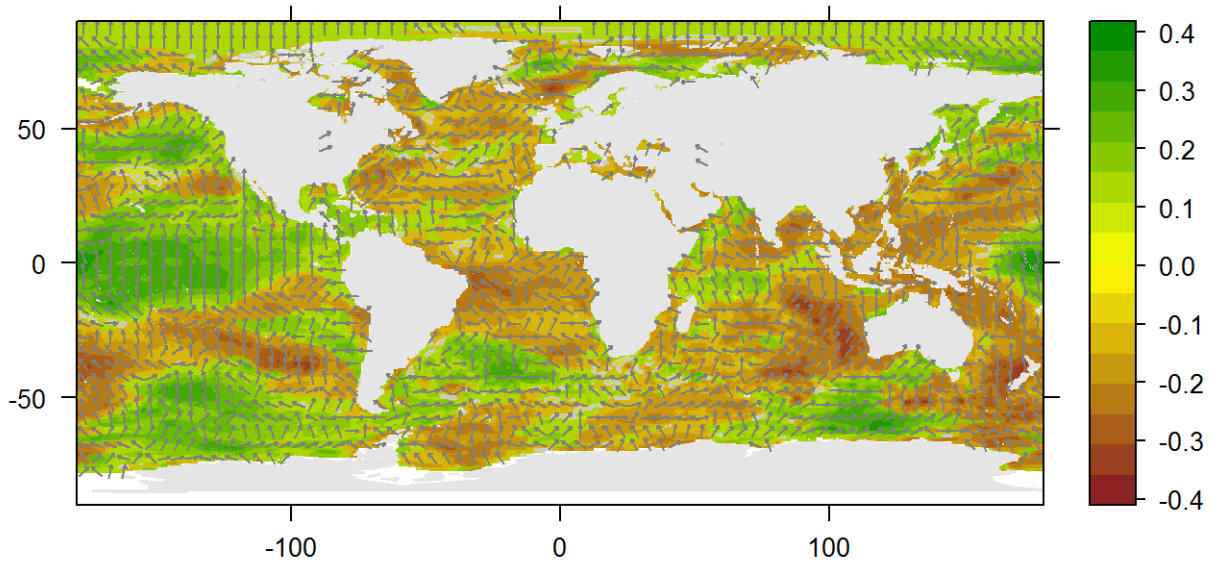

Figure 6-18: ERA-Interim SST anomaly crosscorrelation with **PC5** loadings of SPEI in 3 month aggregation (Limpopo basin). The maximal correlation within a lag of 2 years is shown. Arrows pointing left indicate negative lags. Grey contours denote 0.95 level of correlation significance.

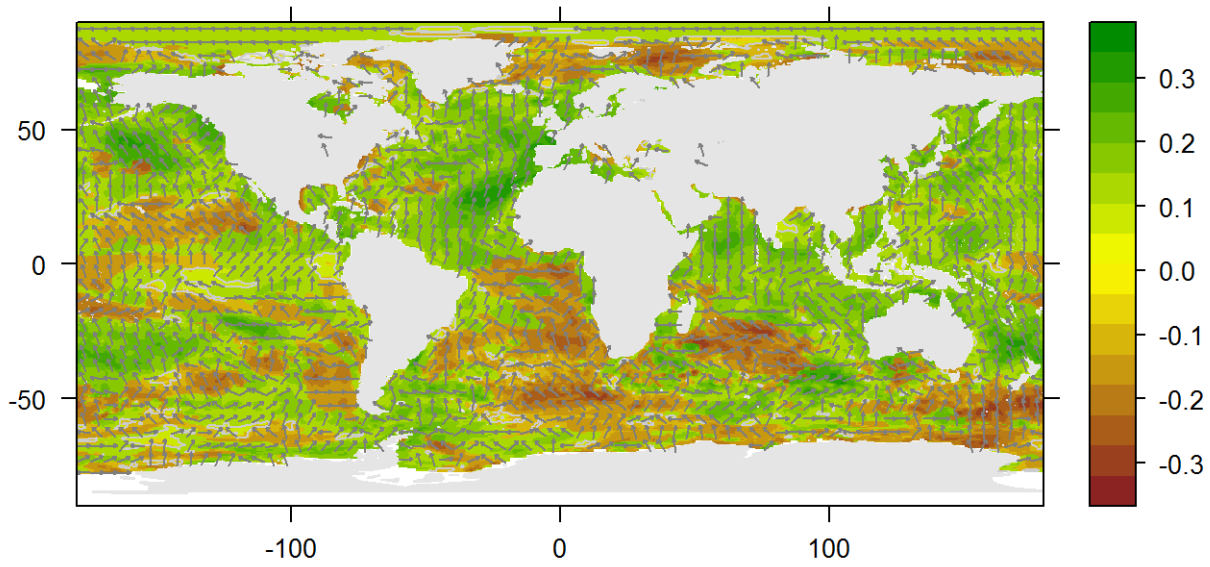

Figure 6-19: ERA-Interim SST anomaly crosscorrelation with **PC6** loadings of SPEI in 3 month aggregation (Limpopo basin). The maximal correlation within a lag of 2 years is shown. Arrows pointing left indicate negative lags. Grey contours denote 0.95 level of correlation significance.

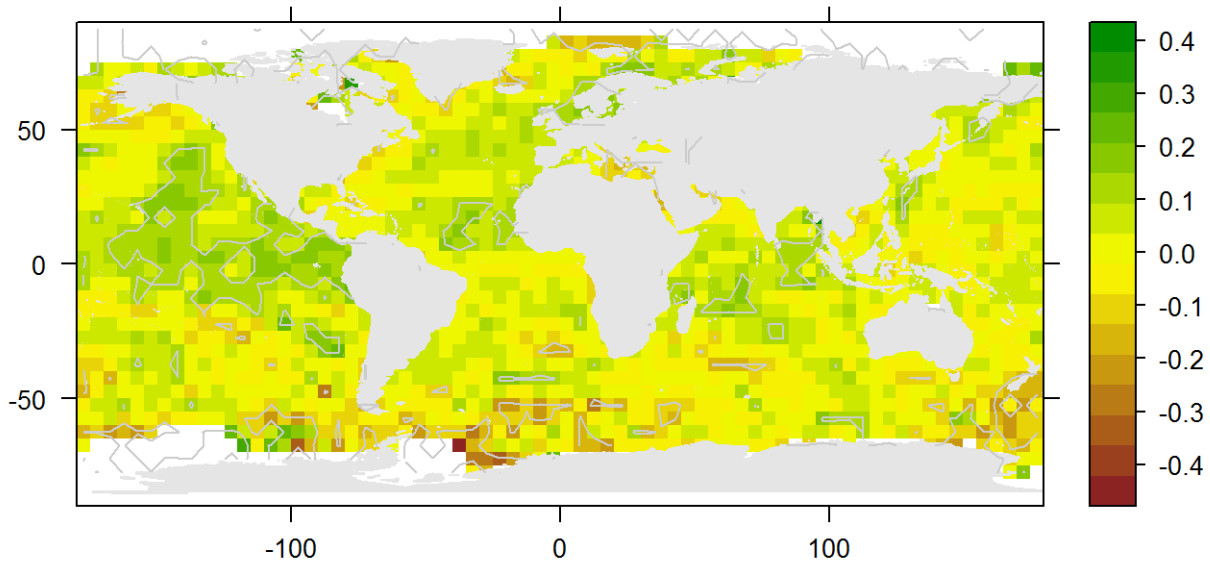

Figure 6-20: : HADSST2 SST anomaly correlation with **PC1** loadings of SPEI in 3 month aggregation (Limpopo basin). Grey contours denote 0.95 level of correlation significance.

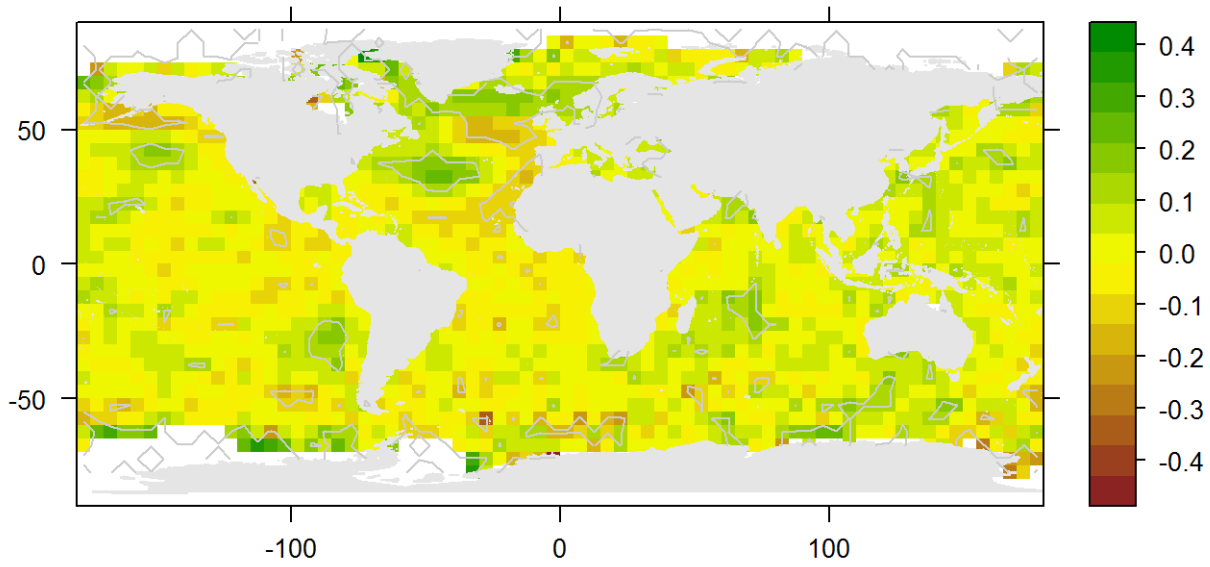

Figure 6-21: : HADSST2 SST anomaly correlation with **PC2** loadings of SPEI in 3 month aggregation (Limpopo basin). Grey contours denote 0.95 level of correlation significance.

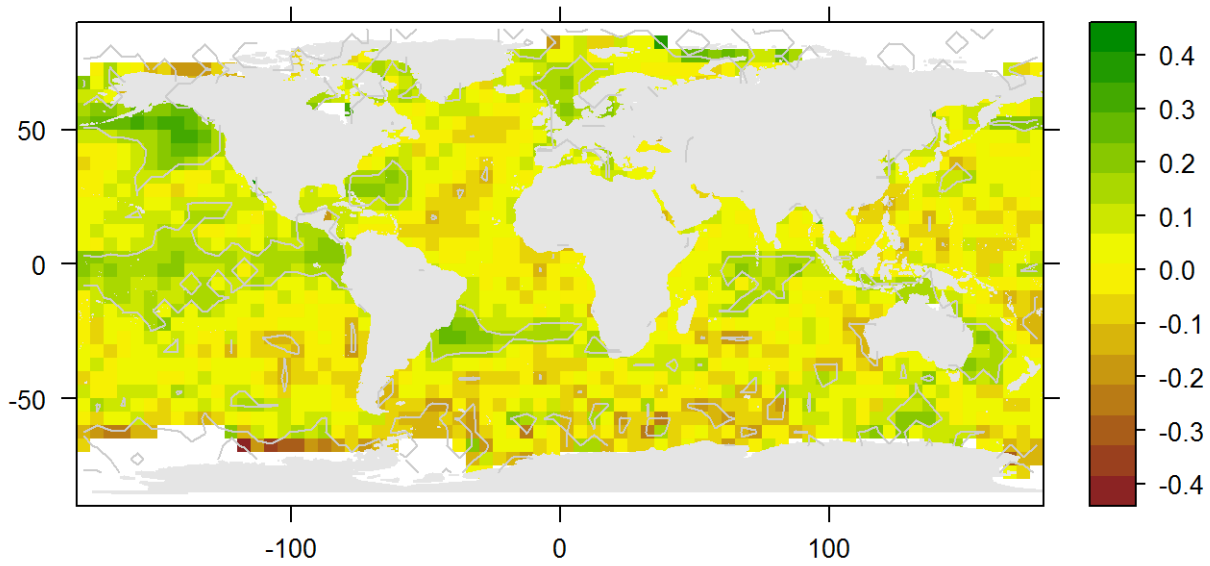

Figure 6-22: : HADSST2 SST anomaly correlation with **PC3** loadings of SPEI in 3 month aggregation (Limpopo basin). Grey contours denote 0.95 level of correlation significance.

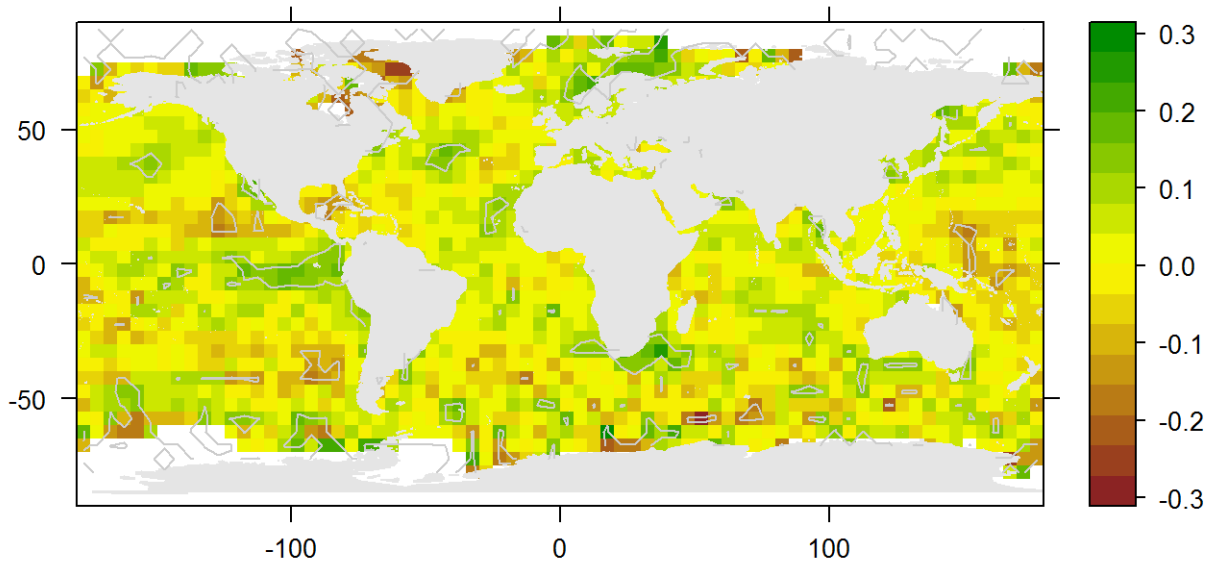

Figure 6-23: : HADSST2 SST anomaly correlation with **PC4** loadings of SPEI in 3 month aggregation (Limpopo basin). Grey contours denote 0.95 level of correlation significance.

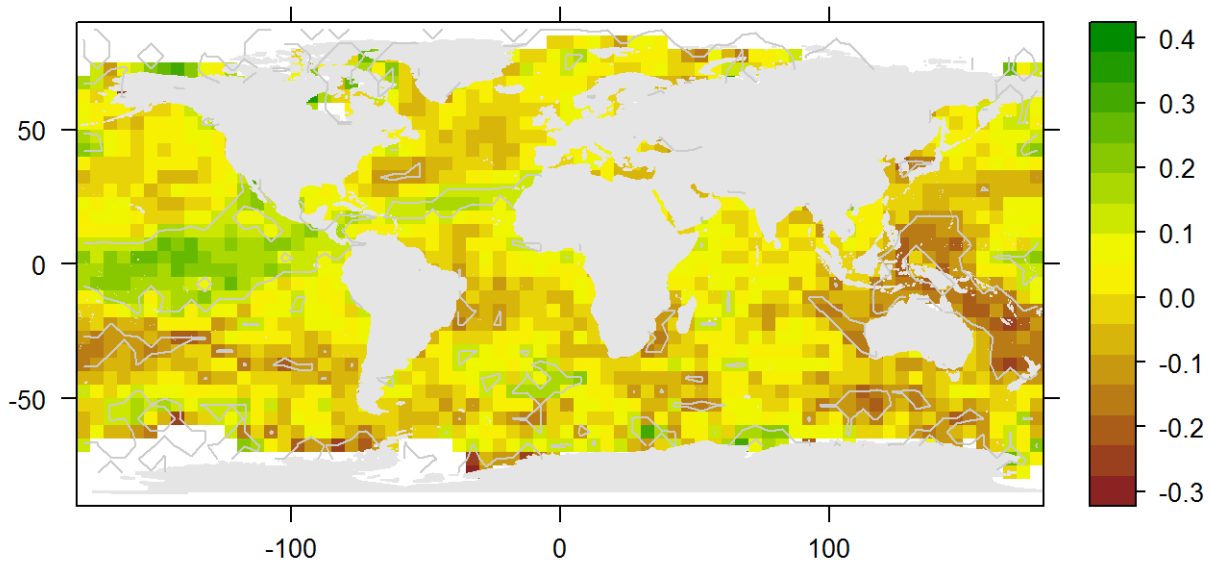

Figure 6-24: : HADSST2 SST anomaly correlation with **PC5** loadings of SPEI in 3 month aggregation (Limpopo basin). Grey contours denote 0.95 level of correlation significance.

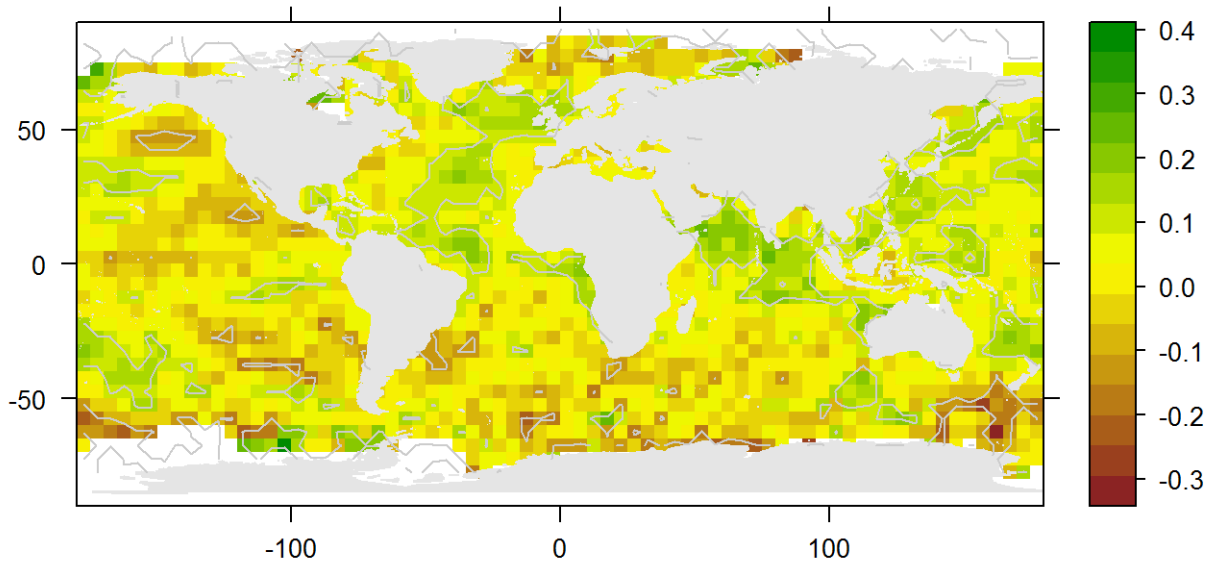

Figure 6-25: : HADSST2 SST anomaly correlation with **PC6** loadings of SPEI in 3 month aggregation (Limpopo basin). Grey contours denote 0.95 level of correlation significance.

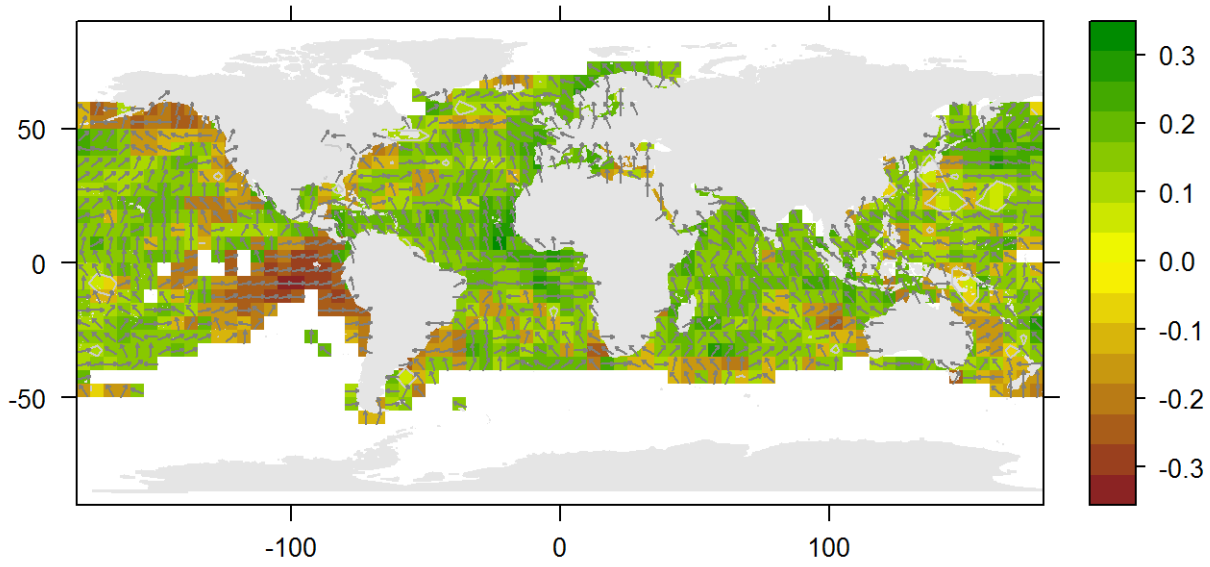

Figure 6-26: HADSST2 SST anomaly crosscorrelation with **PC1** loadings of SPEI in 3 month aggregation (Limpopo basin). The maximal correlation within a lag of 2 years is shown. Arrows pointing left indicate negative lags. Grey contours denote 0.95 level of correlation significance.

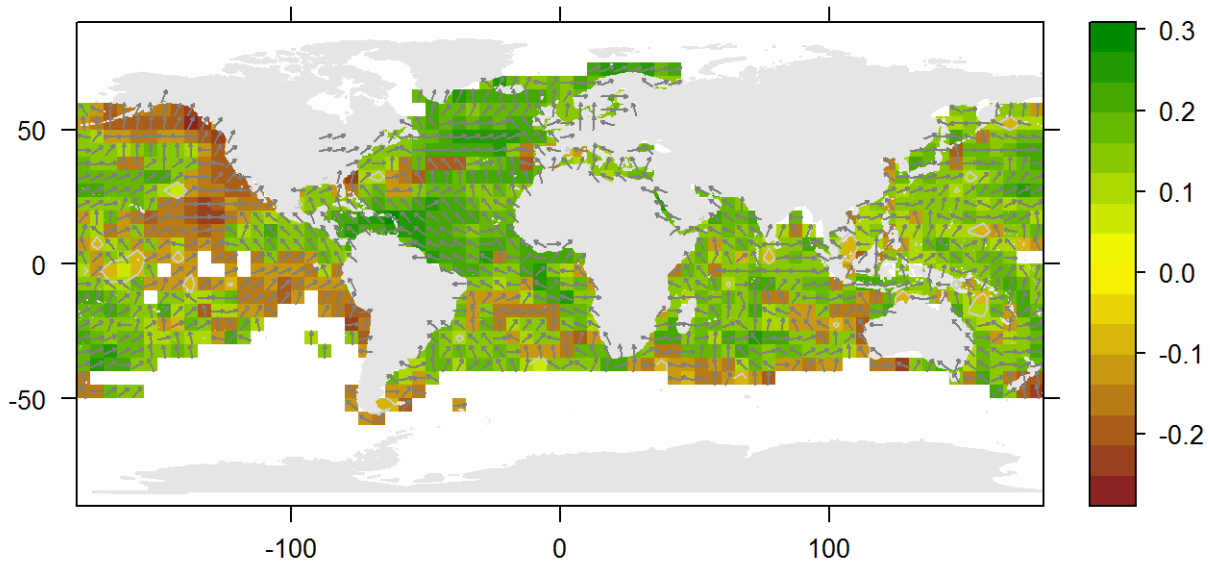

Figure 6-27: HADSST2 SST anomaly crosscorrelation with **PC2** loadings of SPEI in 3 month aggregation (Limpopo basin). The maximal correlation within a lag of 2 years is shown. Arrows pointing left indicate negative lags. Grey contours denote 0.95 level of correlation significance.

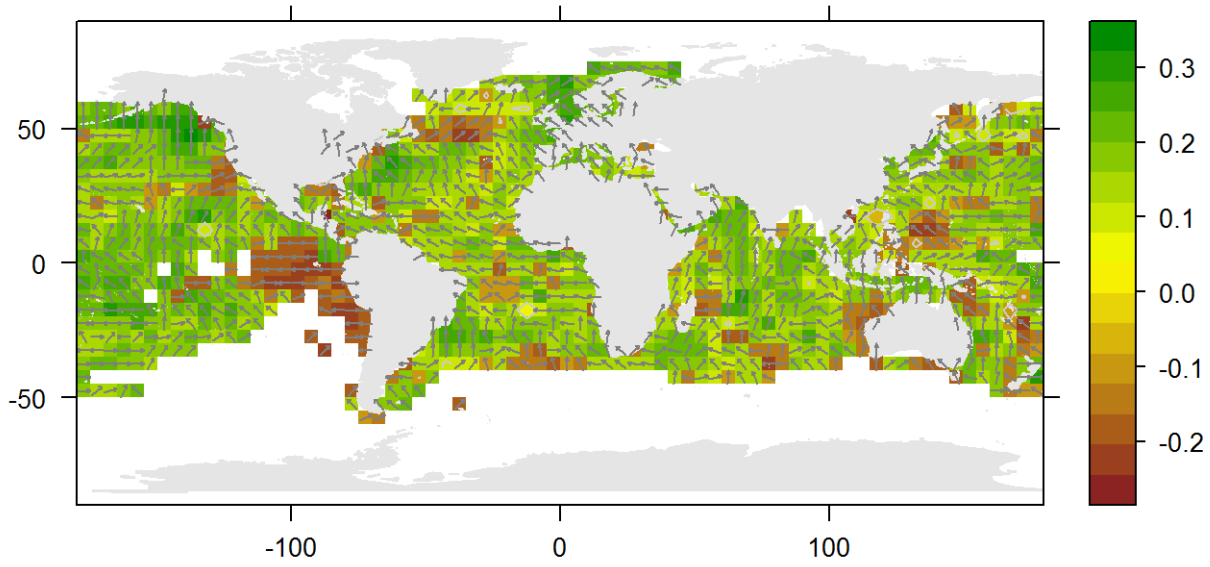

Figure 6-28: HADSST2 SST anomaly crosscorrelation with **PC3** loadings of SPEI in 3 month aggregation (Limpopo basin). The maximal correlation within a lag of 2 years is shown. Arrows pointing left indicate negative lags. Grey contours denote 0.95 level of correlation significance.

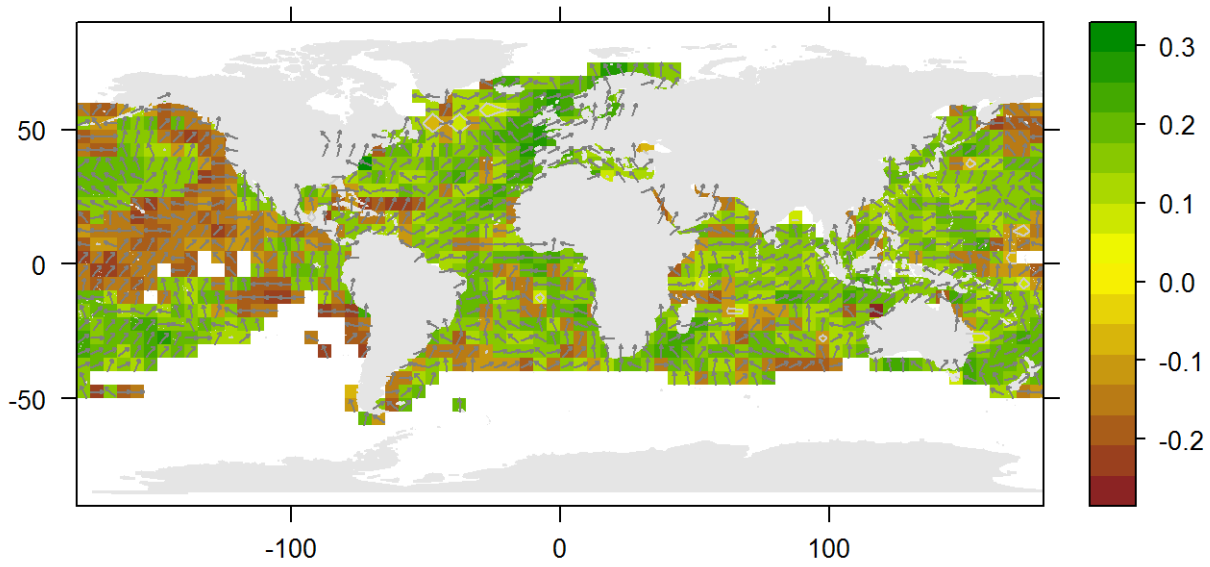

Figure 6-29: HADSST2 SST anomaly crosscorrelation with **PC4** loadings of SPEI in 3 month aggregation (Limpopo basin). The maximal correlation within a lag of 2 years is shown. Arrows pointing left indicate negative lags. Grey contours denote 0.95 level of correlation significance.

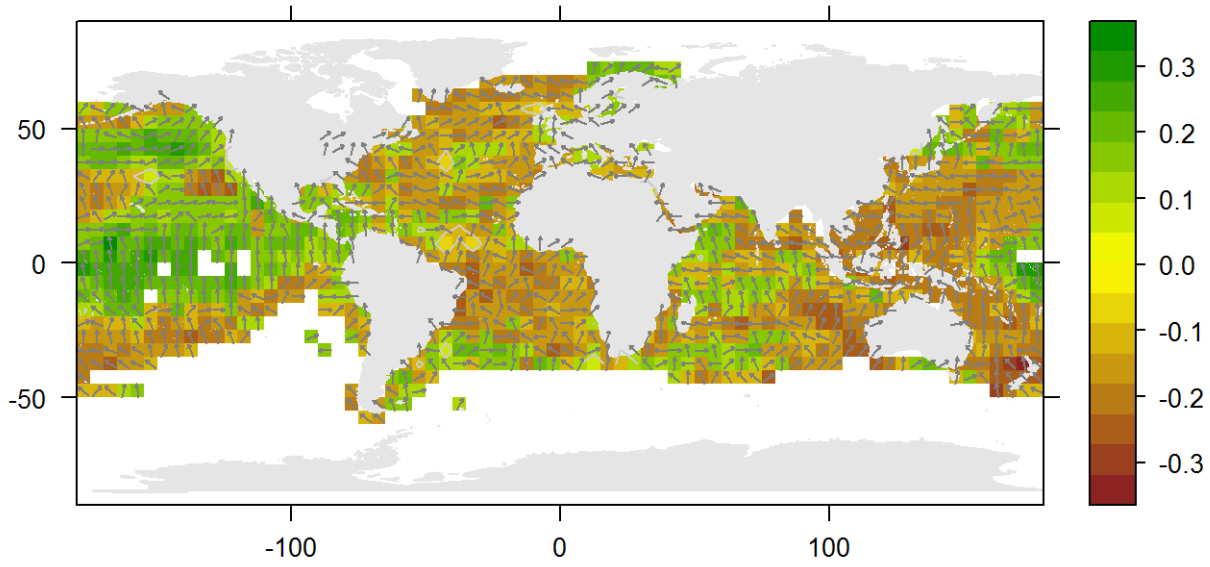

Figure 6-30: HADSST2 SST anomaly crosscorrelation with **PC5** loadings of SPEI in 3 month aggregation (Limpopo basin). The maximal correlation within a lag of 2 years is shown. Arrows pointing left indicate negative lags. Grey contours denote 0.95 level of correlation significance.

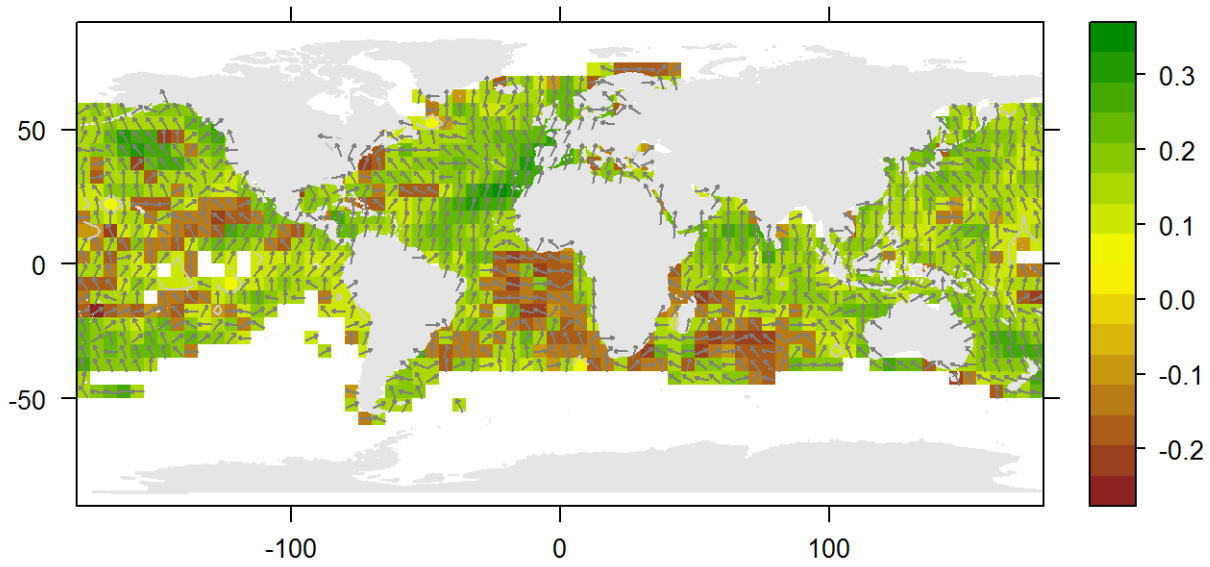

Figure 6-31: HADSST2 SST anomaly crosscorrelation with **PC6** loadings of SPEI in 3 month aggregation (Limpopo basin). The maximal correlation within a lag of 2 years is shown. Arrows pointing left indicate negative lags. Grey contours denote 0.95 level of correlation significance.

6.1.2 Wavelet analysis of runoff

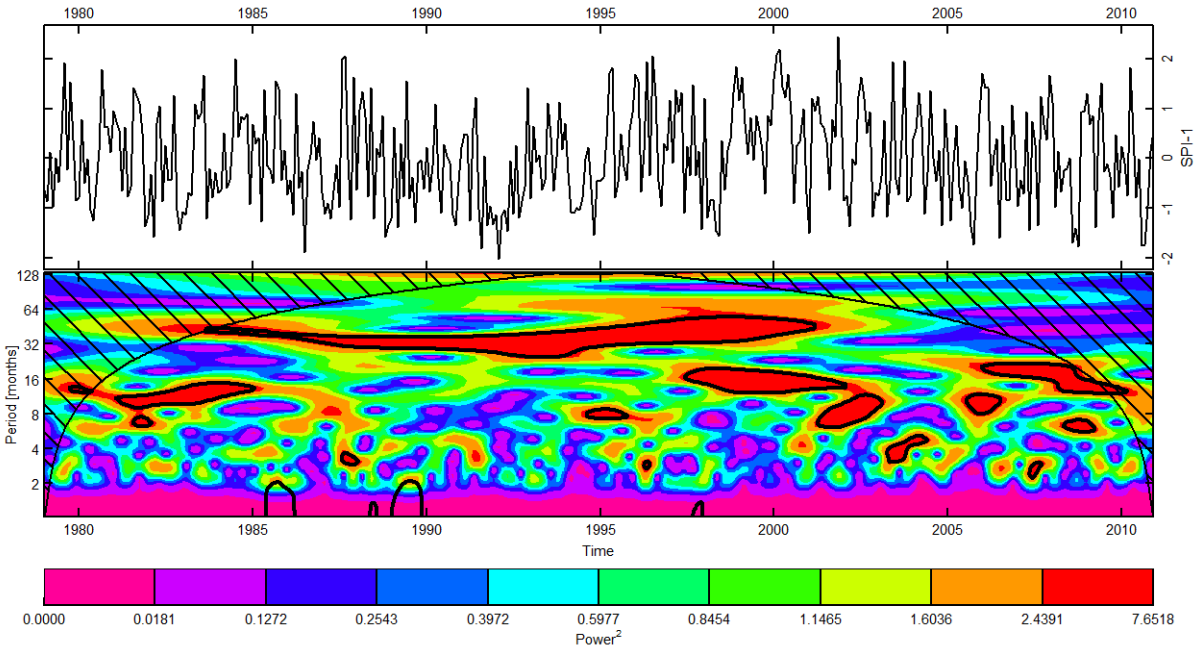

Figure 6-32: Wavelet analysis: Limpopo 1-month-SPI (upper) and wavelet power spectrum (lower) with contours showing significance.

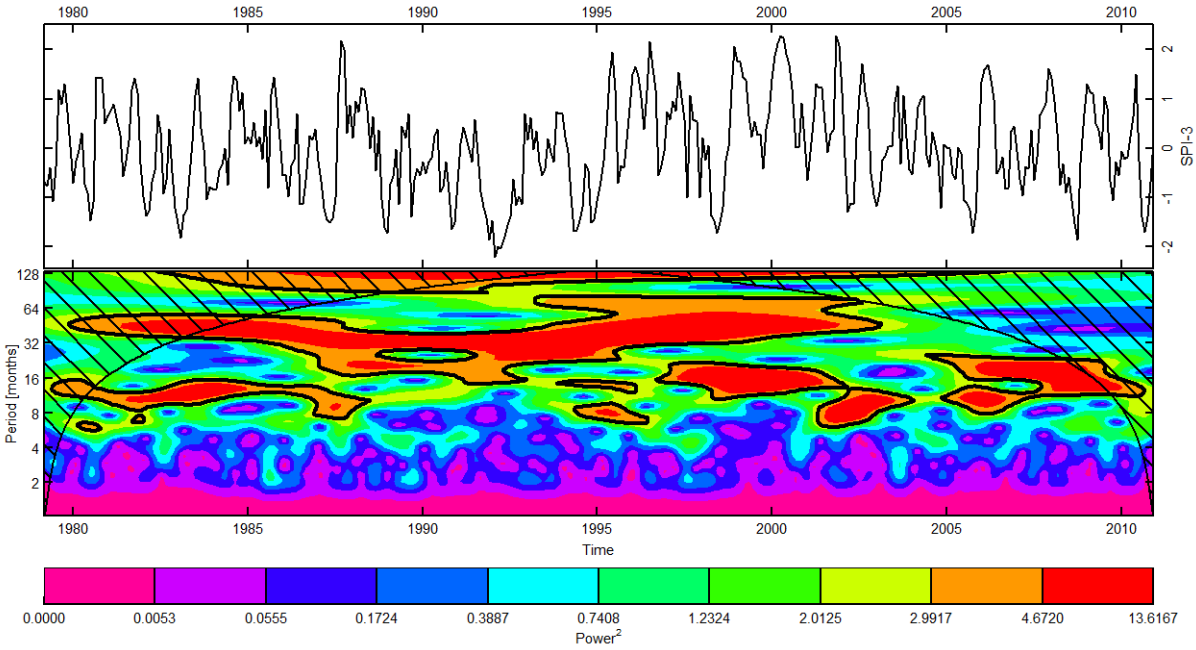

Figure 6-33: Wavelet analysis: Limpopo 3-month-SPI (upper) and wavelet power spectrum (lower) with contours showing significance.

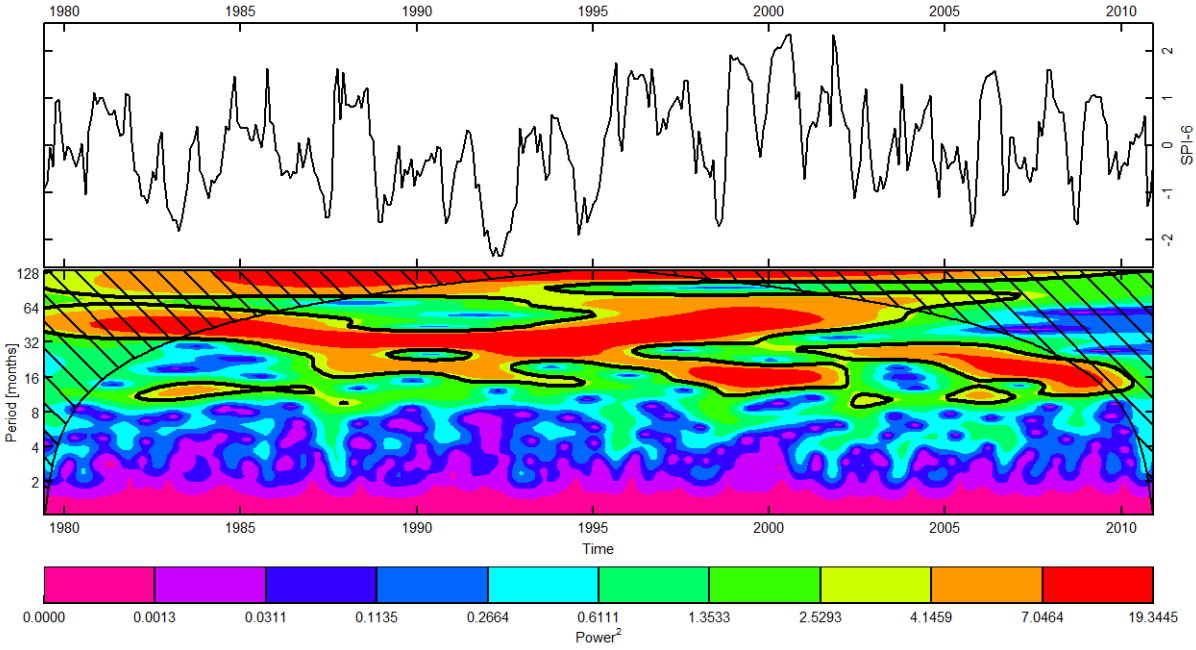

Figure 6-34: Wavelet analysis: Limpopo 6-month-SPI (upper) and wavelet power spectrum (lower) with contours showing significance.

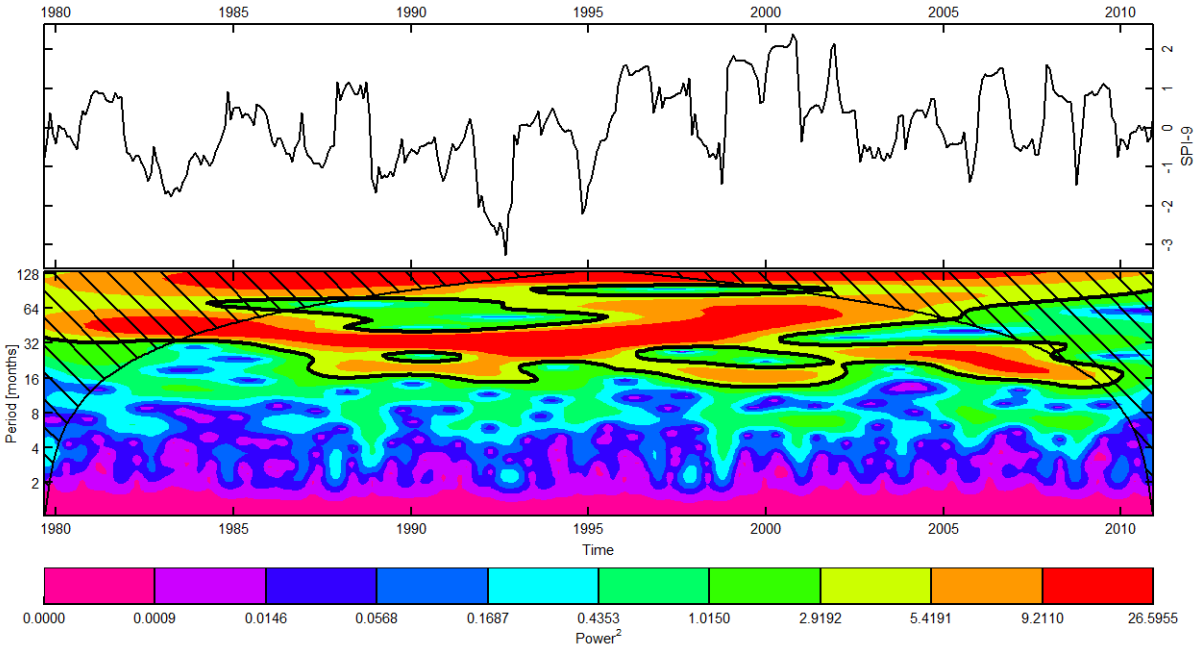

Figure 6-35: Wavelet analysis: Limpopo 9-month-SPI (upper) and wavelet power spectrum (lower) with contours showing significance.

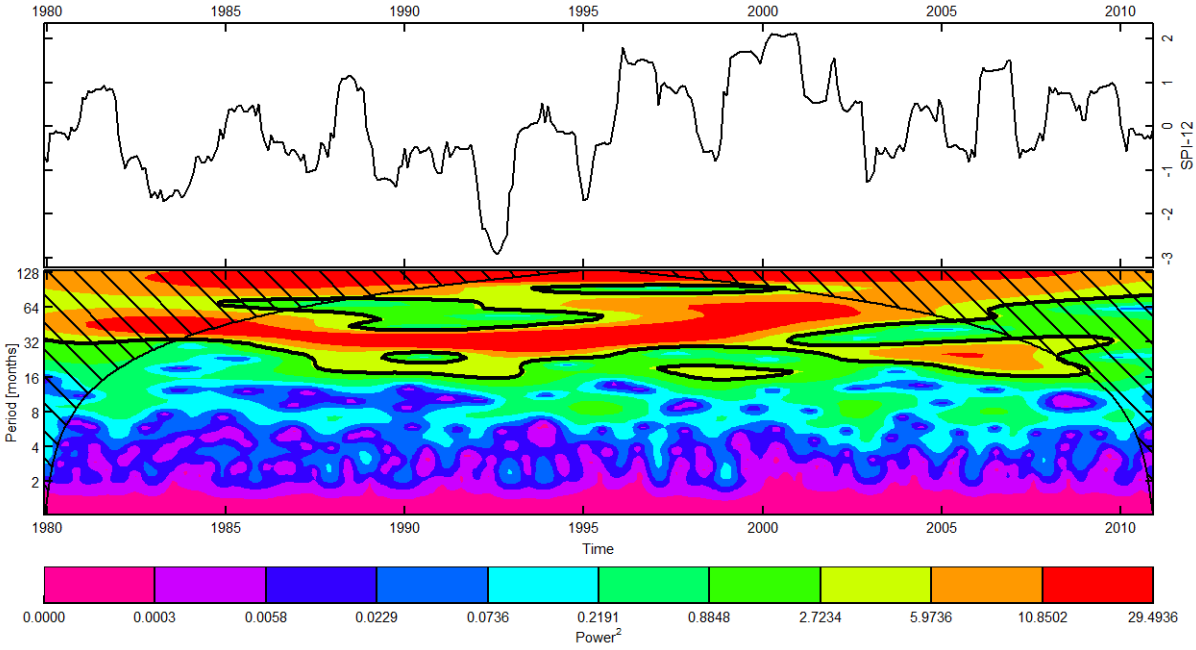

Figure 6-36: Wavelet analysis: Limpopo 12-month-SPI (upper) and wavelet power spectrum (lower) with contours showing significance.

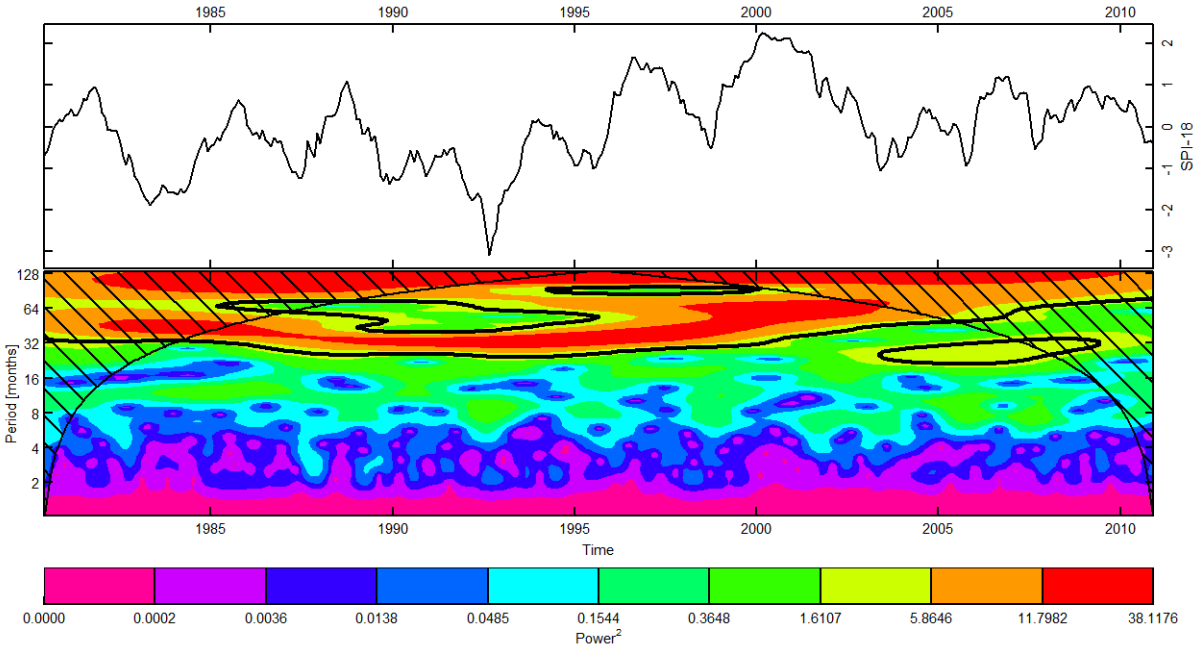

Figure 6-37: Wavelet analysis: Limpopo 18-month-SPI (upper) and wavelet power spectrum (lower) with contours showing significance.

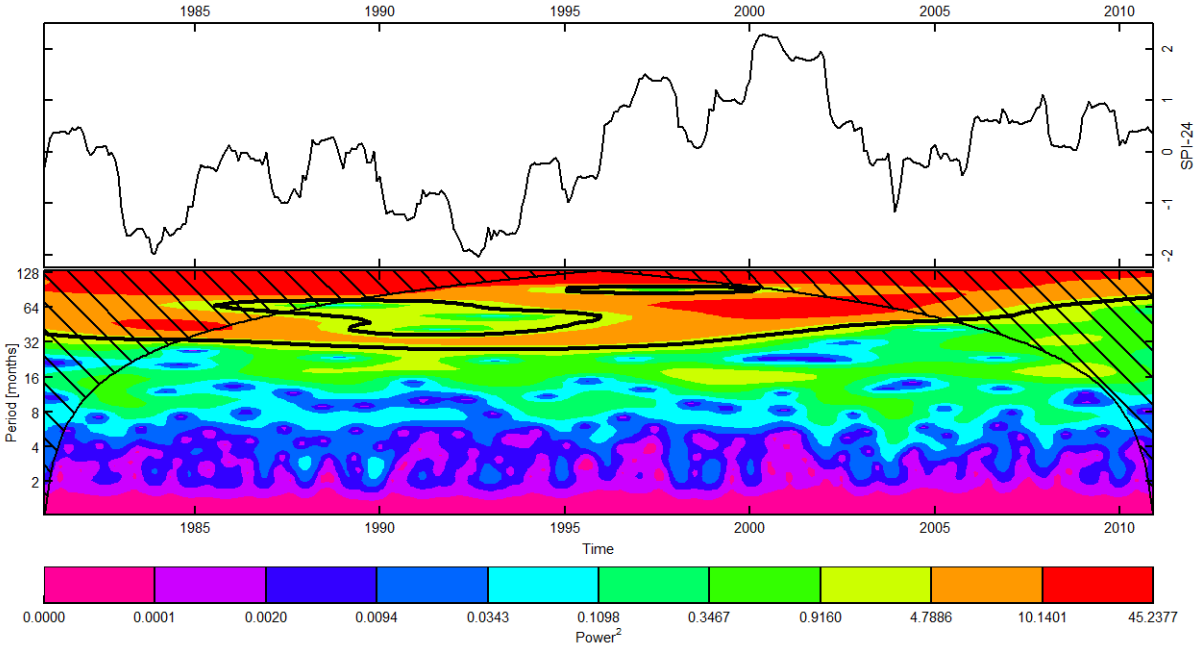

Figure 6-38: Wavelet analysis: Limpopo 24-month-SPI (upper) and wavelet power spectrum (lower) with contours showing significance.

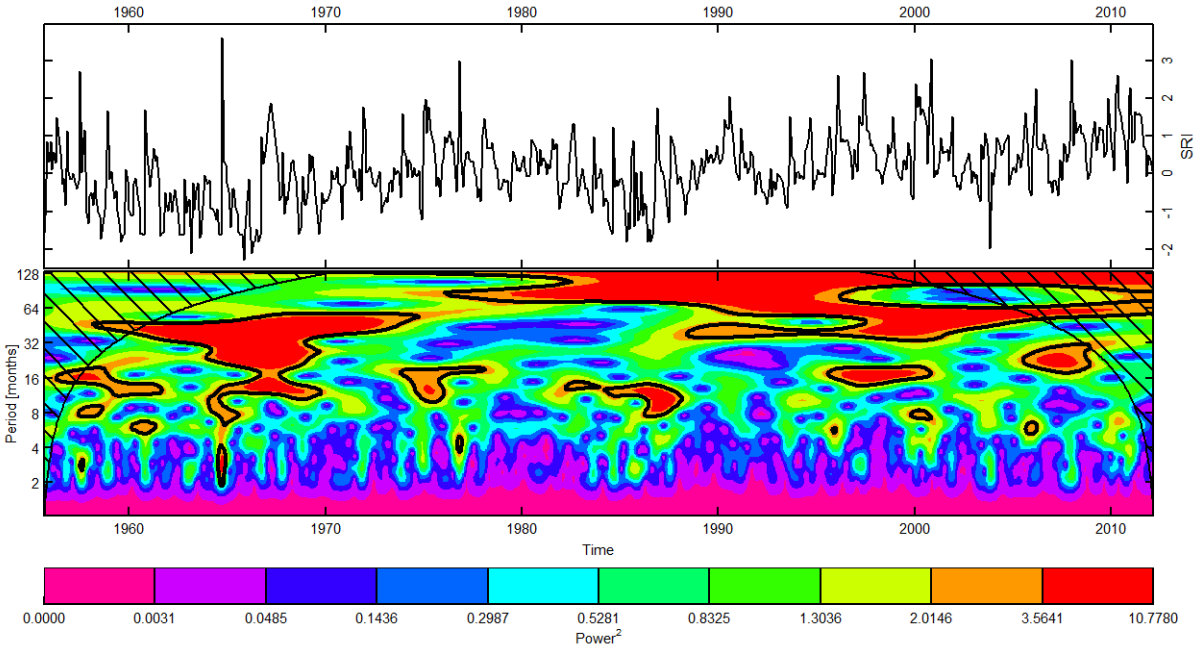

Figure 6-39: Pienaars River (Buffelspoort): standardized runoff index time series (upper) and wavelet analysis power spectra (lower).

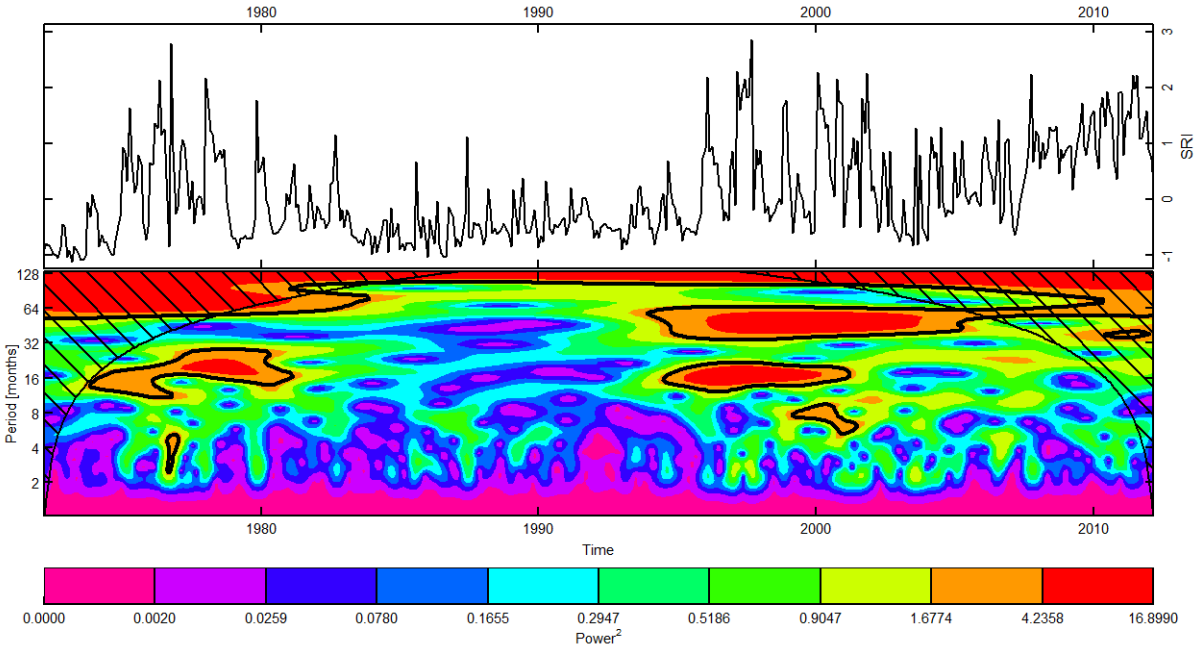

Figure 6-40: Krokodil River: standardized runoff index time series (upper) and wavelet analysis power spectra (lower).

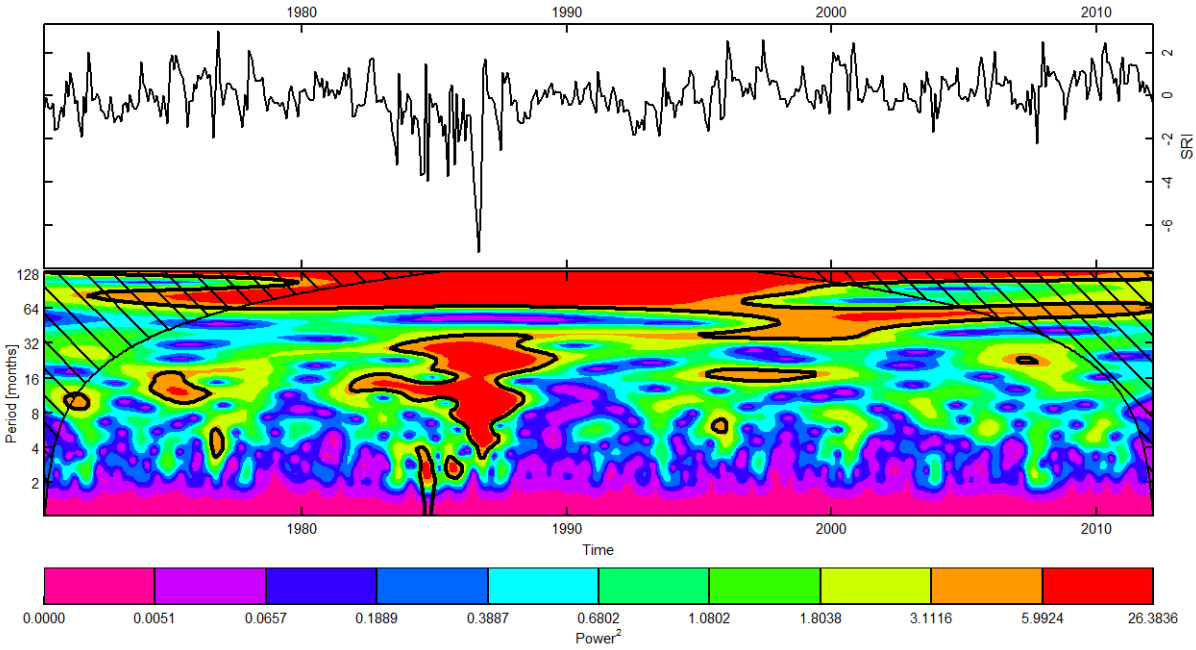

Figure 6-41: Pienaars River (Klipvoor): standardized runoff index time series (upper) and wavelet analysis power spectra (lower).

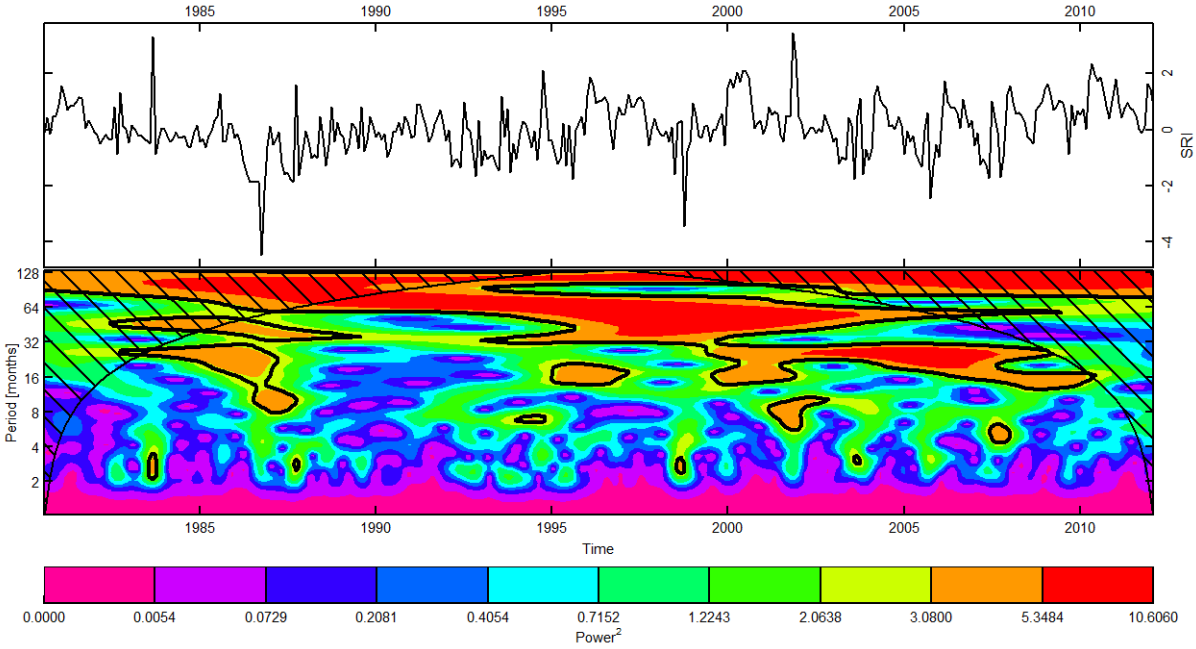

Figure 6-42: Mokolo River: standardized runoff index time series (upper) and wavelet analysis power spectra (lower).

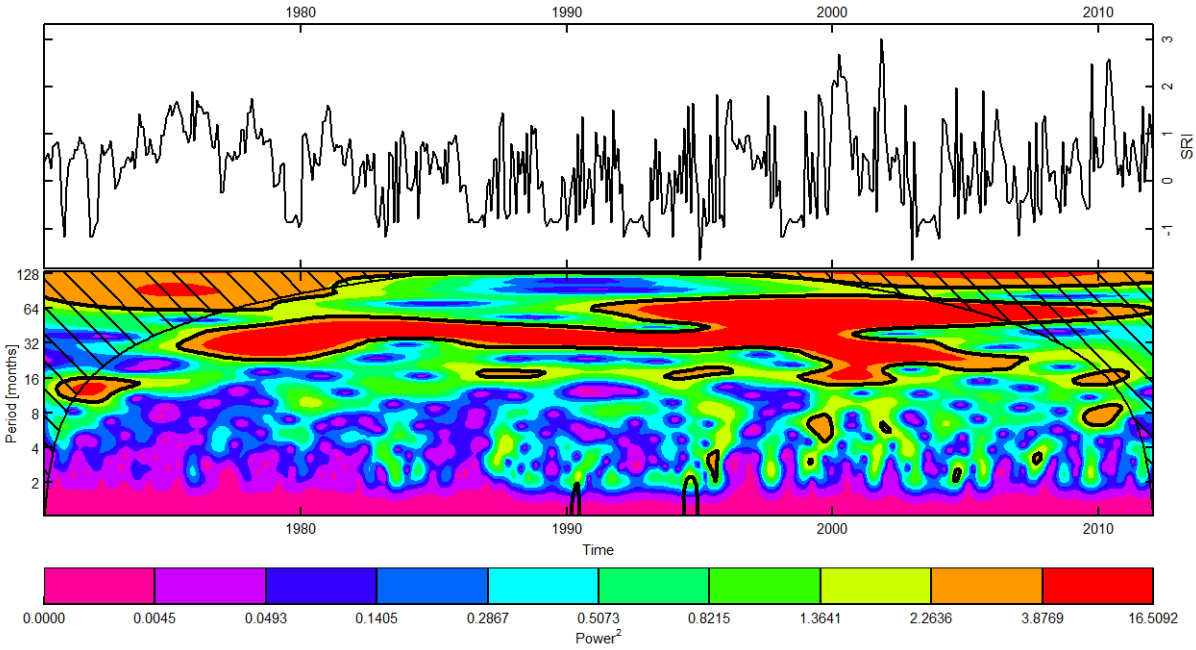

Figure 6-43: Mogalakwena River (Glen Alpine): standardized runoff index time series (upper) and wavelet analysis power spectra (lower).

6.1.3 Wavelet coherence analysis of runoff/precipitation and climate anomaly factors

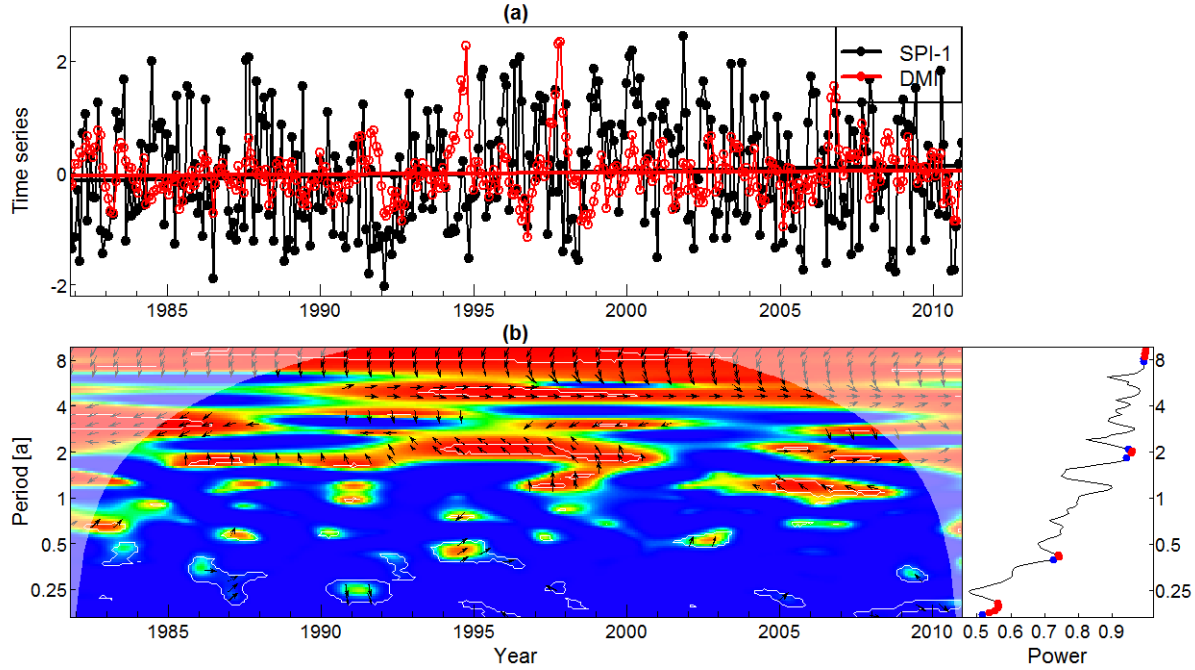

Figure 6-44: Limpopo Basin:1-month Standardized Precipitation Index (SPI) and the Indian Ocean Dipole Mode Index (DMI) time series (upper) and wavelet coherence plot (lower). Arrow directions indicate the phase relationship: in phase (right), antiphase (left), red leading black (down), black leading red (up).

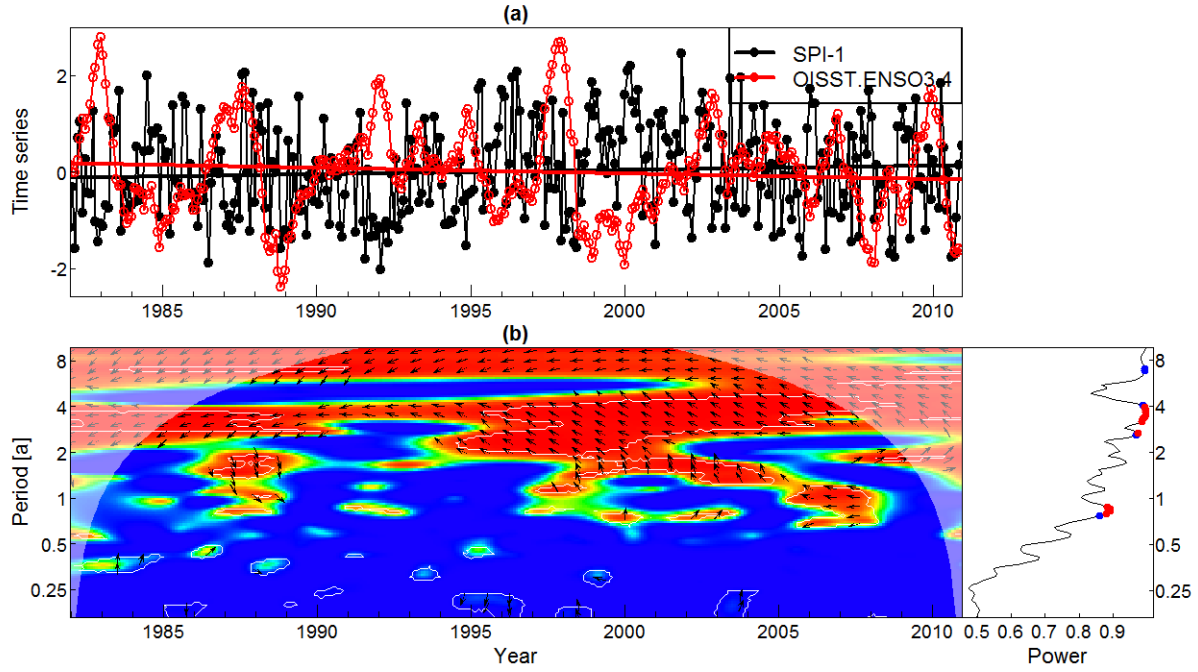

Figure 6-45: Limpopo Basin:1-month Standardized Precipitation Index (SPI) and NINO3.4 (OISST2 dataset) time series (upper) and wavelet coherence plot (lower). Arrow directions indicate the phase relationship: in phase (right), antiphase (left), red leading black (down), black leading red (up).

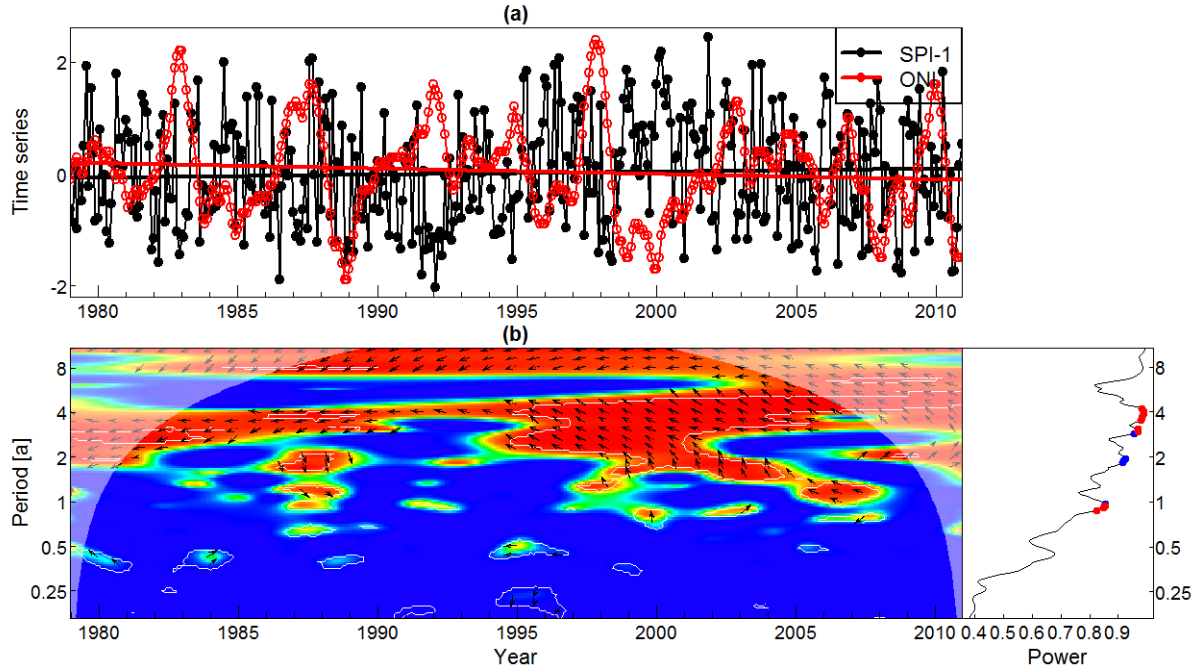

Figure 6-46: Limpopo Basin:1-month Standardized Precipitation Index (SPI) and Oceanic Nino Index (ONI) time series (upper) and wavelet coherence plot (lower). Arrow directions indicate the phase relationship: in phase (right), antiphase (left), red leading black (down), black leading red (up).

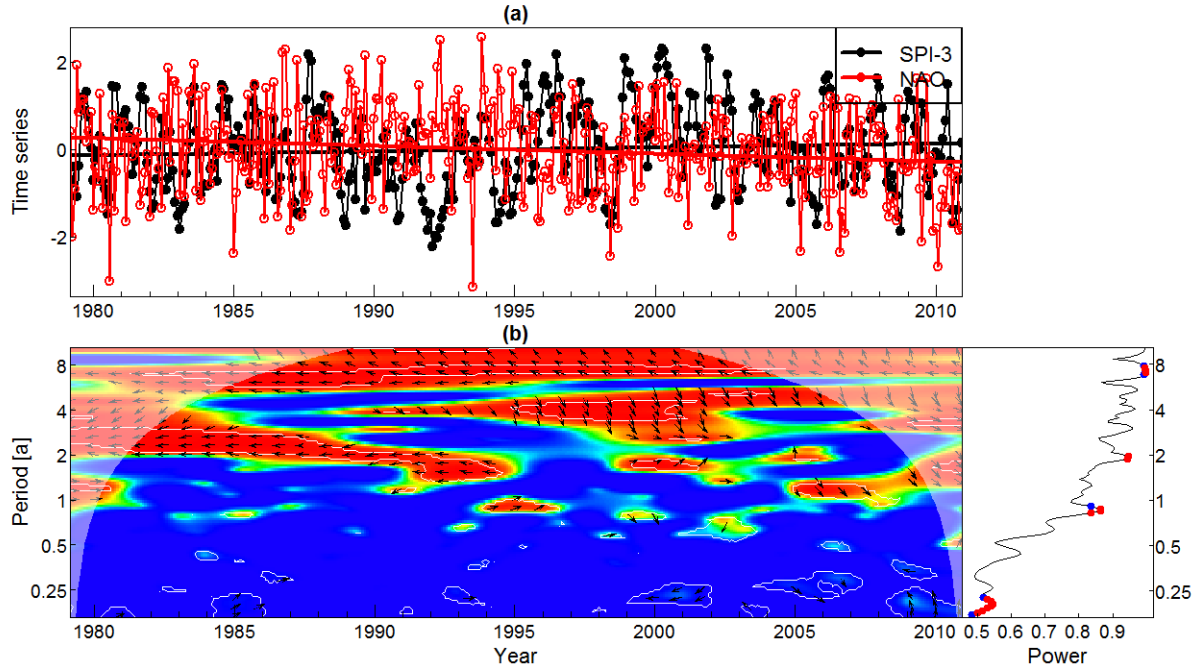

Figure 6-47: Limpopo Basin:1-month Standardized Precipitation Index (SPI) and NINO3.4 (OISST2 dataset) time series (upper) and wavelet coherence plot (lower). Arrow directions indicate the phase relationship: in phase (right), antiphase (left), red leading black (down), black leading red (up).

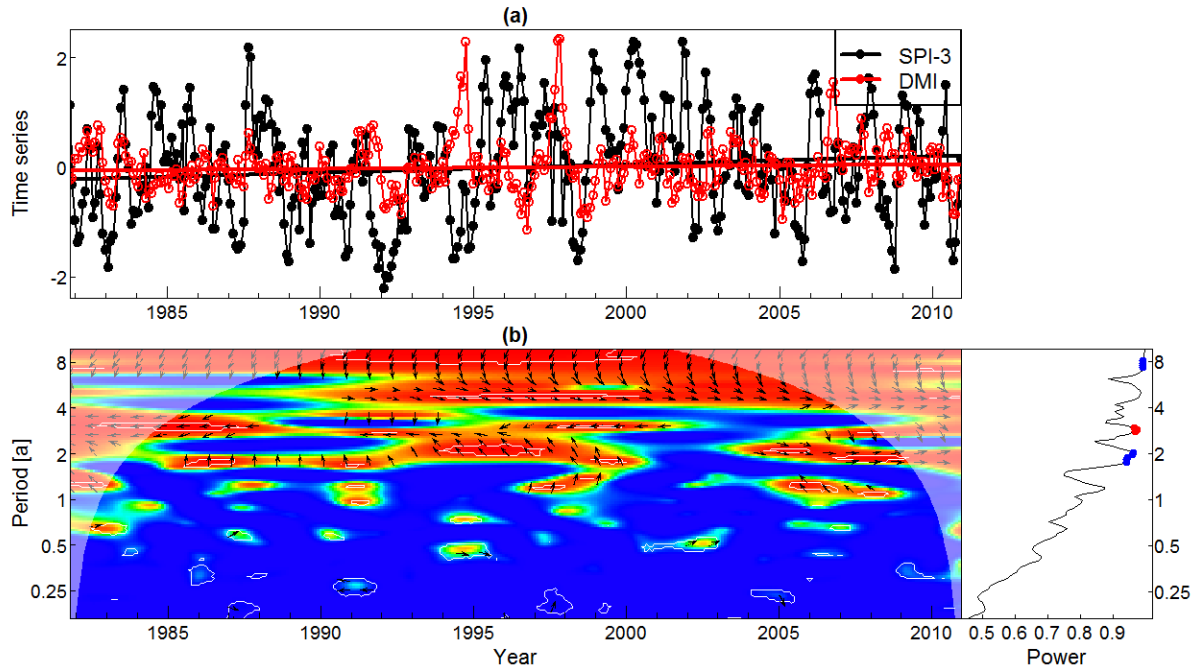

Figure 6-48: Limpopo Basin: 3-month Standardized Precipitation Index (SPI) and the Indian Ocean Dipole Mode Index (DMI) time series (upper) and wavelet coherence plot (lower). Arrow directions indicate the phase relationship: in phase (right), antiphase (left), red leading black (down), black leading red (up).

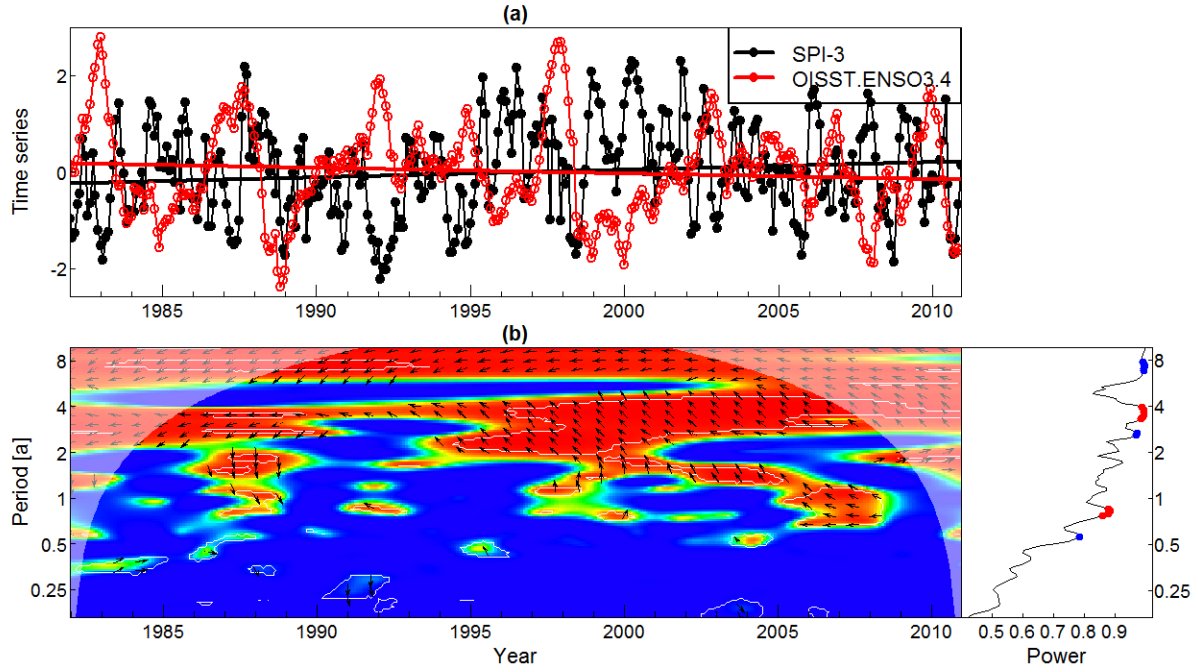

Figure 6-49: Limpopo Basin: 3-month Standardized Precipitation Index (SPI) and NINO3.4 (OISST2 dataset) time series (upper) and wavelet coherence plot (lower). Arrow directions indicate the phase relationship: in phase (right), antiphase (left), red leading black (down), black leading red (up).

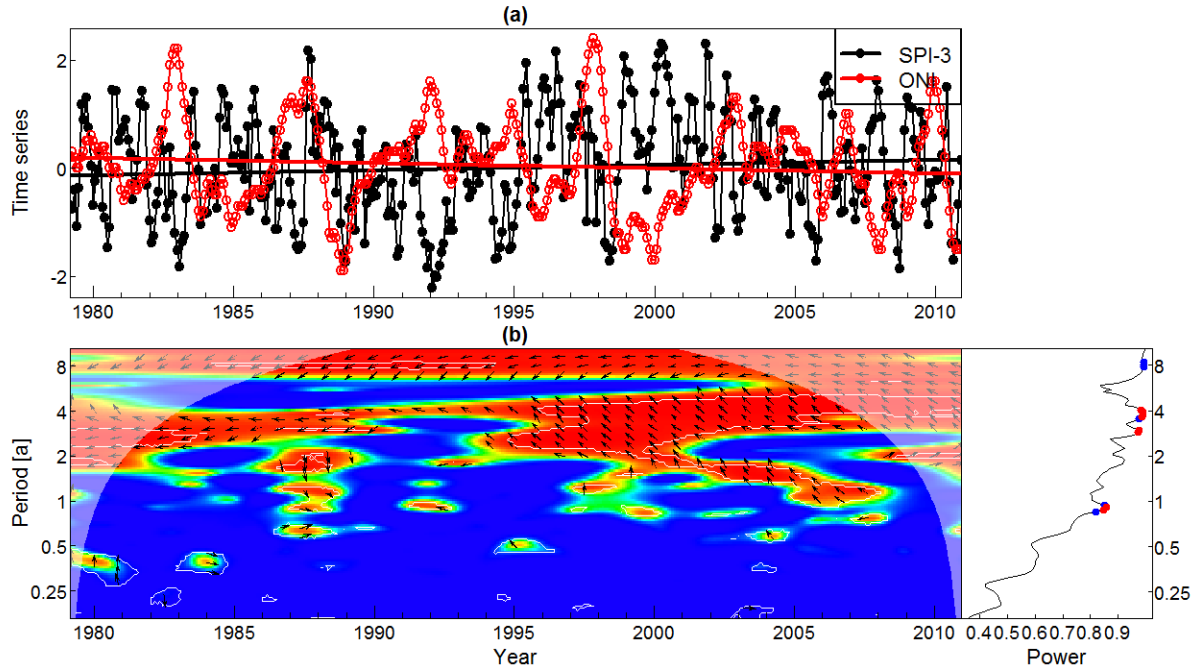

Figure 6-50: Limpopo Basin:3-month Standardized Precipitation Index (SPI) and Oceanic Nino Index (ONI) time series (upper) and wavelet coherence plot (lower). Arrow directions indicate the phase relationship: in phase (right), antiphase (left), red leading black (down), black leading red (up).

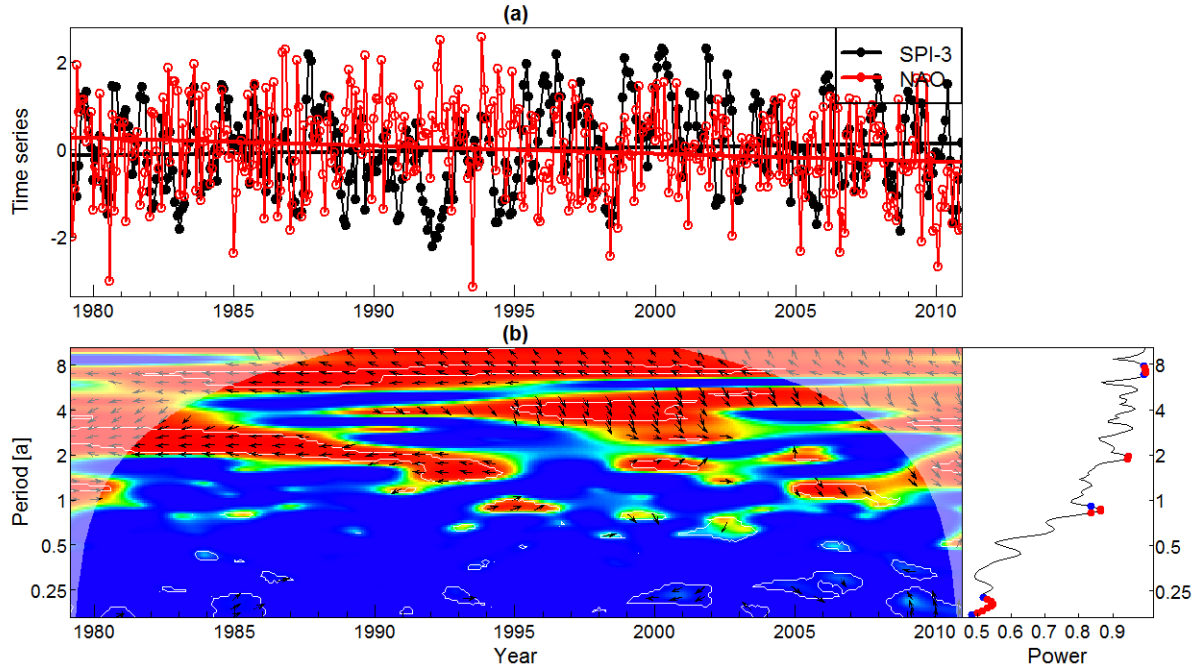

Figure 6-51: Limpopo Basin:3-month Standardized Precipitation Index (SPI) and Northern Atlantic Oscillation Index (NAO) time series (upper) and wavelet coherence plot (lower). Arrow directions indicate the phase relationship: in phase (right), antiphase (left), red leading black (down), black leading red (up).

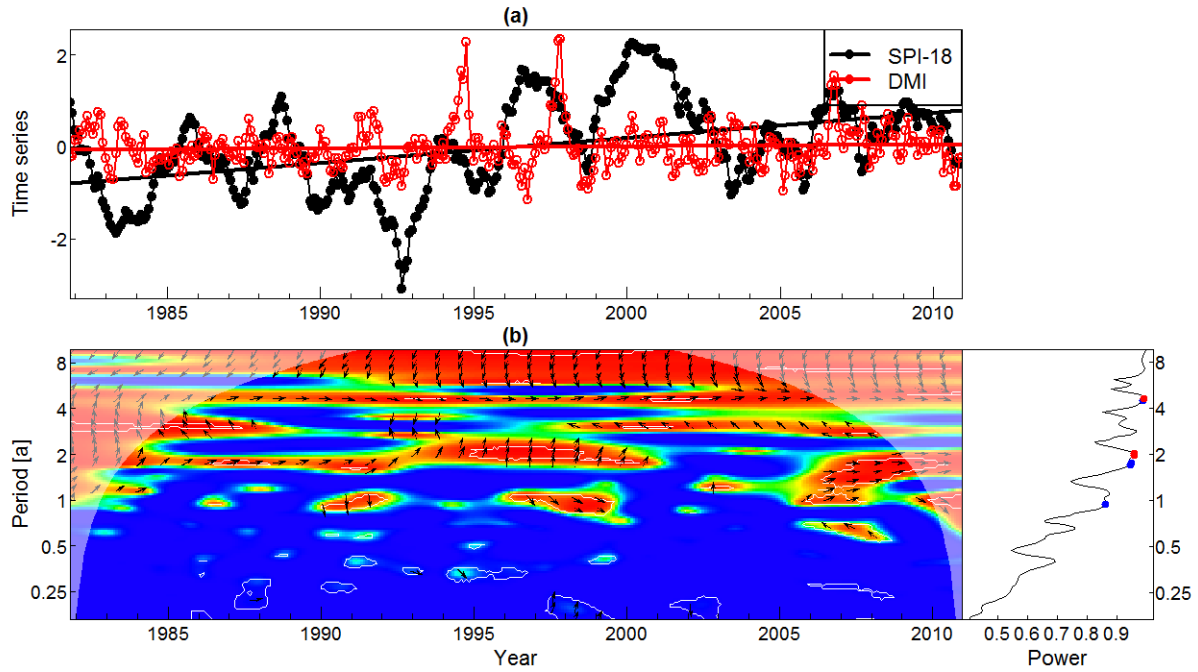

Figure 6-52: Limpopo Basin: 18-month Standardized Precipitation Index (SPI) and the Indian Ocean Dipole Mode Index (DMI) time series (upper) and wavelet coherence plot (lower). Arrow directions indicate the phase relationship: in phase (right), antiphase (left), red leading black (down), black leading red (up).

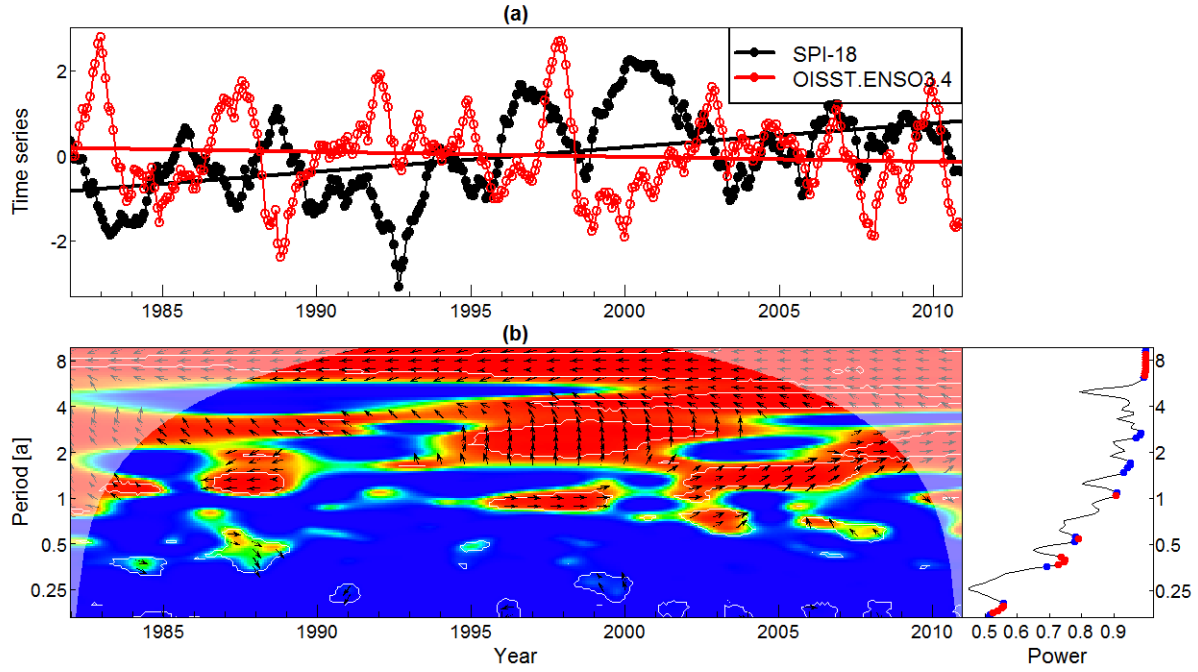

Figure 6-53: Limpopo Basin: 18-month Standardized Precipitation Index (SPI) and NINO3.4 (OISST2 dataset) time series (upper) and wavelet coherence plot (lower). Arrow directions indicate the phase relationship: in phase (right), antiphase (left), red leading black (down), black leading red (up).

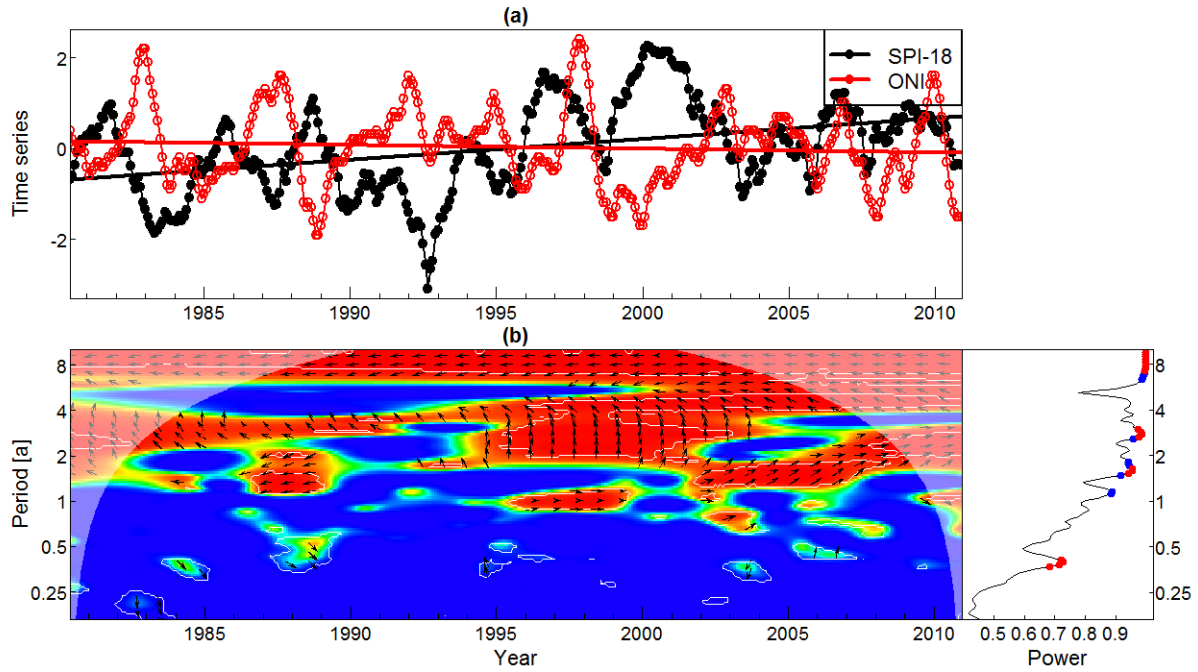

Figure 6-54: Limpopo Basin:18-month Standardized Precipitation Index (SPI) and Oceanic Nino Index (ONI) time series (upper) and wavelet coherence plot (lower). Arrow directions indicate the phase relationship: in phase (right), antiphase (left), red leading black (down), black leading red (up).

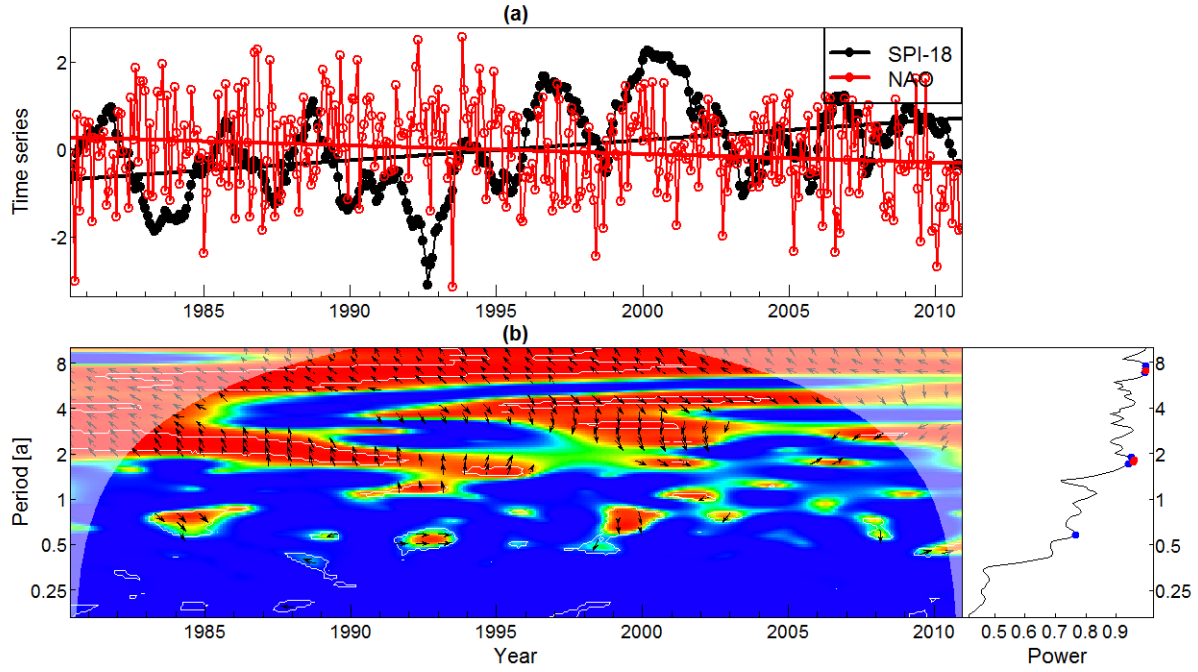

Figure 6-55: Limpopo Basin:18-month Standardized Precipitation Index (SPI) and Northern Atlantic Oscillation Index (NAO) time series (upper) and wavelet coherence plot (lower). Arrow directions indicate the phase relationship: in phase (right), antiphase (left), red leading black (down), black leading red (up).

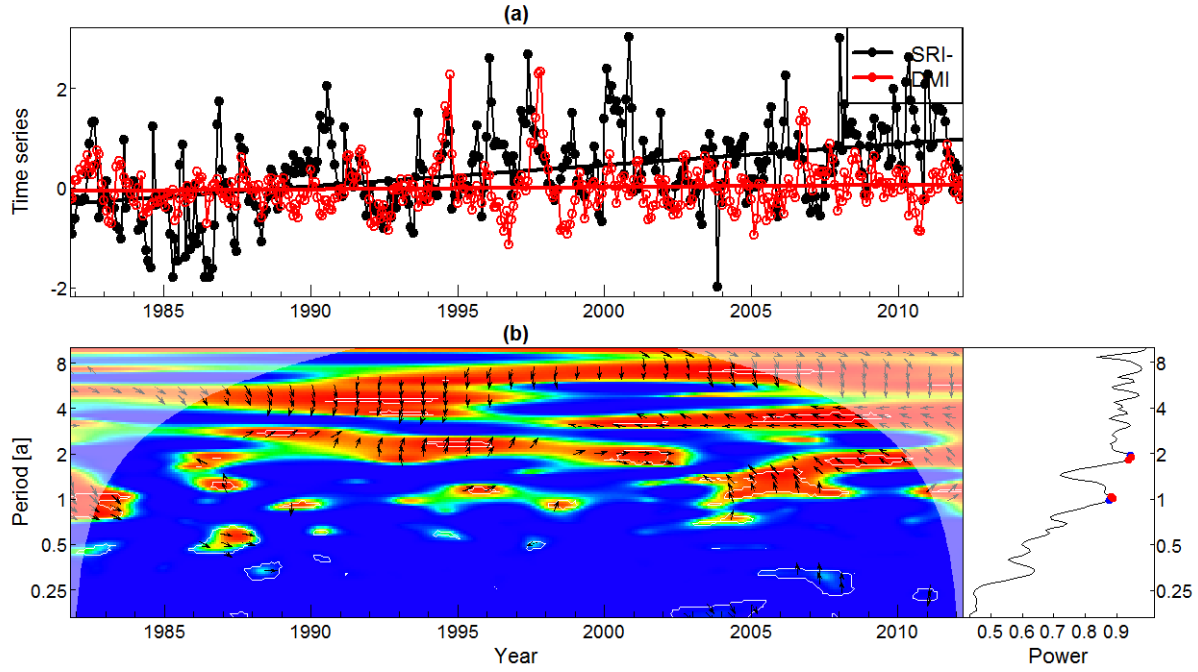

Figure 6-56: Pienaars River (**Buffelspoort**): Standardized runoff index (SRI) and Indian Ocean Dipole Mode Index (**DMI**) time series (upper) and wavelet coherence plot (lower). Arrow directions indicate the phase relationship: in phase (right), antiphase (left), red leading black (down), black leading red (up).

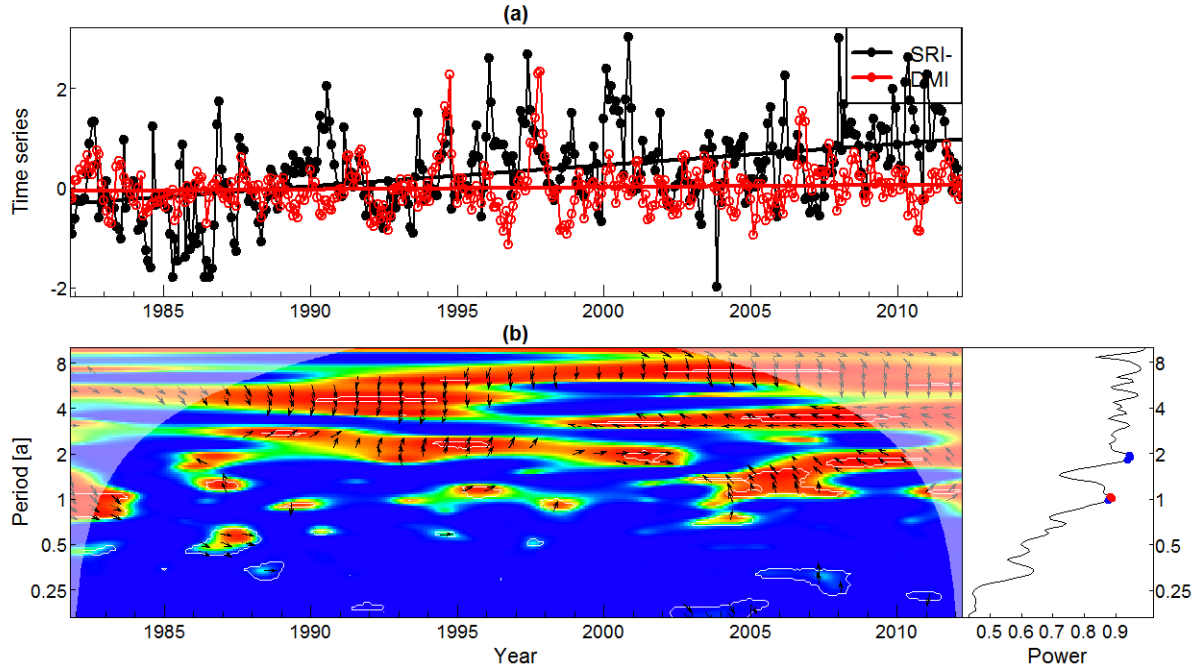

Figure 6-57: Pienaars River (**Buffelspoort**): Standardized runoff index (SRI) and Indian Ocean Dipole Mode Index (**DMI**) time series (upper) and wavelet coherence plot (lower). Arrow directions indicate the phase relationship: in phase (right), antiphase (left), red leading black (down), black leading red (up).

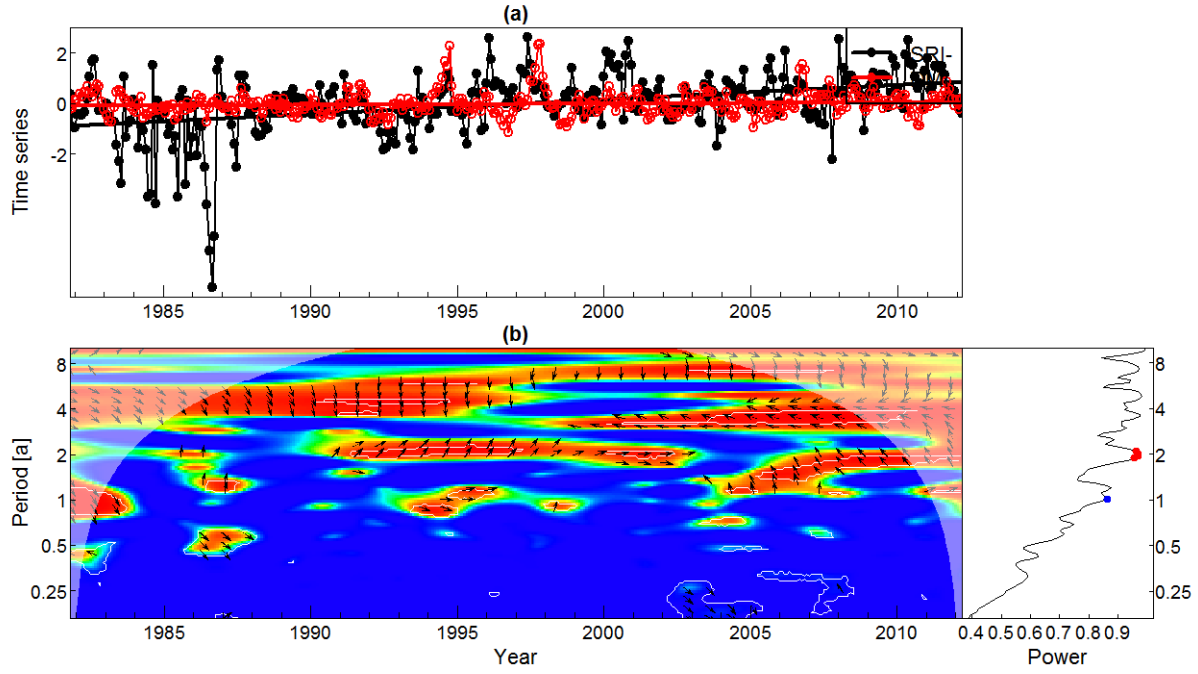

Figure 6-58: Pienaars River (**Klipvoor**):): Standardized runoff index (SRI) and Indian Ocean Dipole Mode Index (**DMI**) time series (upper) and wavelet coherence plot (lower). Arrow directions indicate the phase relationship: in phase (right), antiphase (left), red leading black (down), black leading red (up).

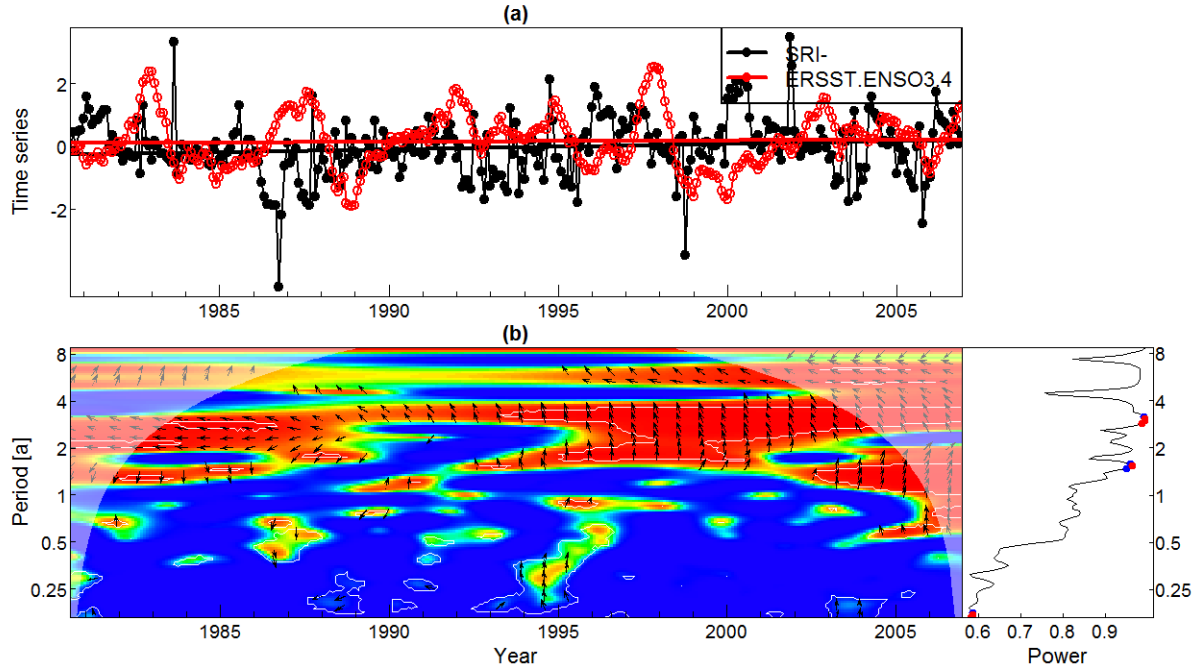

Figure 6-59: Mokolo River (Mokolo Nature Reserve): Standardized runoff index (SRI) and **NINO 3.4** (ERSST) time series plot (upper) and wavelet coherence plot (lower). Arrow directions indicate the phase relationship: in phase (right), antiphase (left), red leading black (down), black leading red (up).

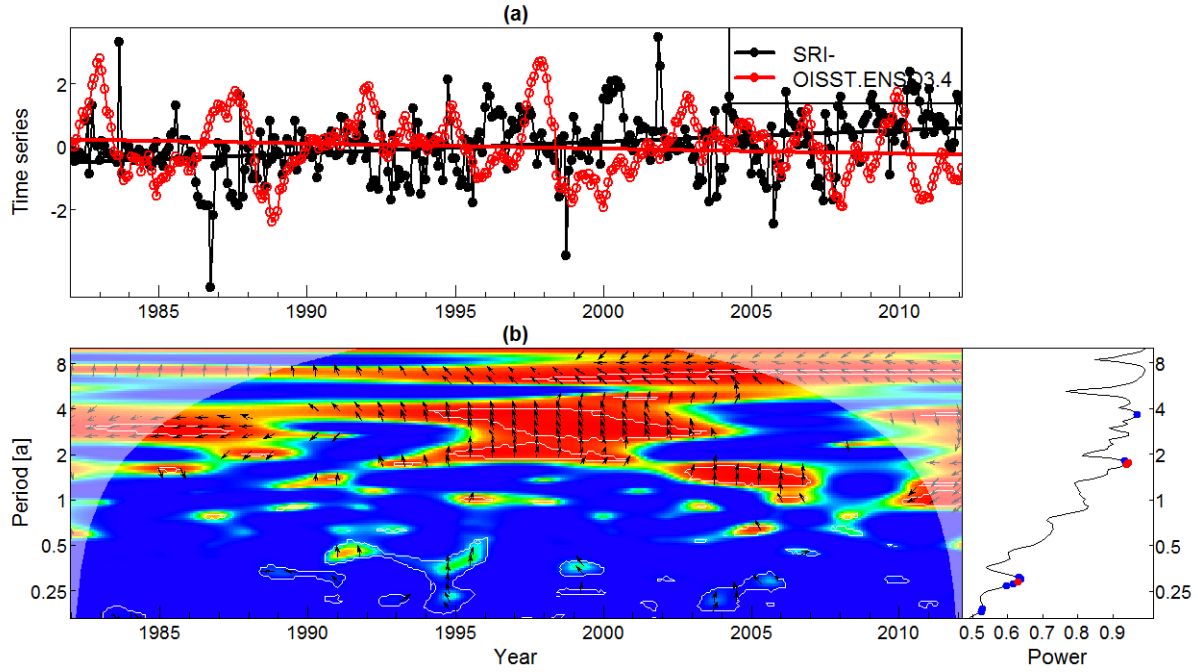

Figure 6-60: Mokolo River (Mokolo Nature Reserve): Standardized runoff index (SRI) and **NINO 3.4** (OISST) time series plot (upper) and wavelet coherence plot (lower). Arrow directions indicate the phase relationship: in phase (right), antiphase (left), red leading black (down), black leading red (up).

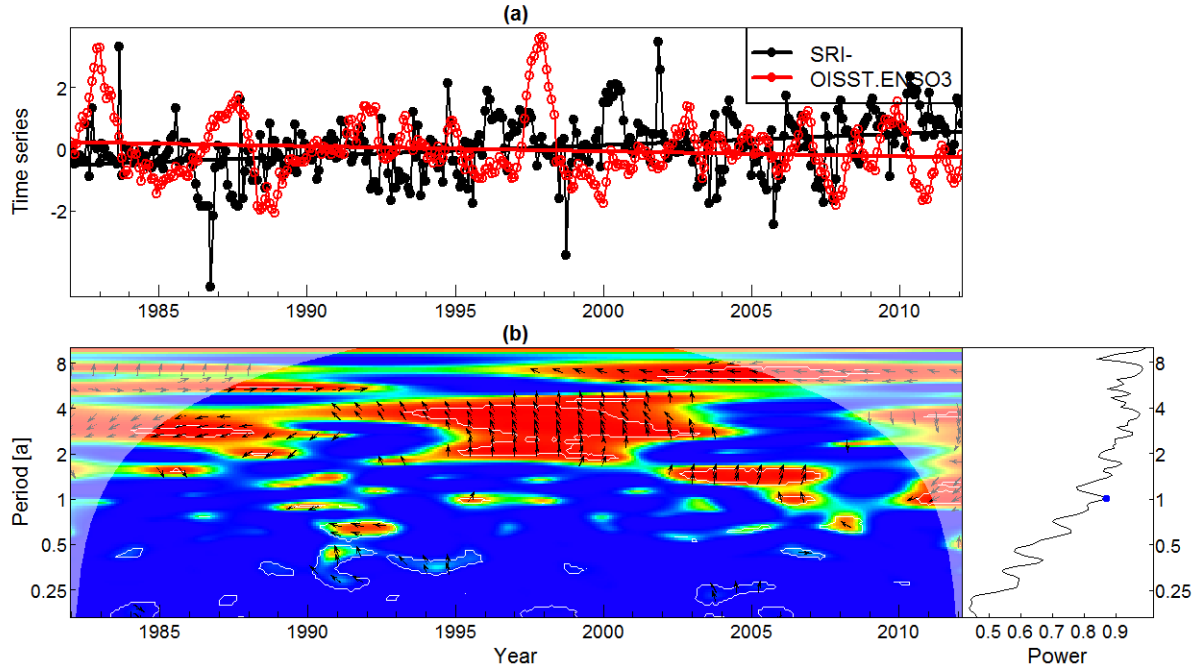

Figure 6-61: Mokolo River (Mokolo Nature Reserve): Standardized runoff index (SRI) and **NINO 3** (OISST) time series plot (upper) and wavelet coherence plot (lower). Arrow directions indicate the phase relationship: in phase (right), antiphase (left), red leading black (down), black leading red (up).

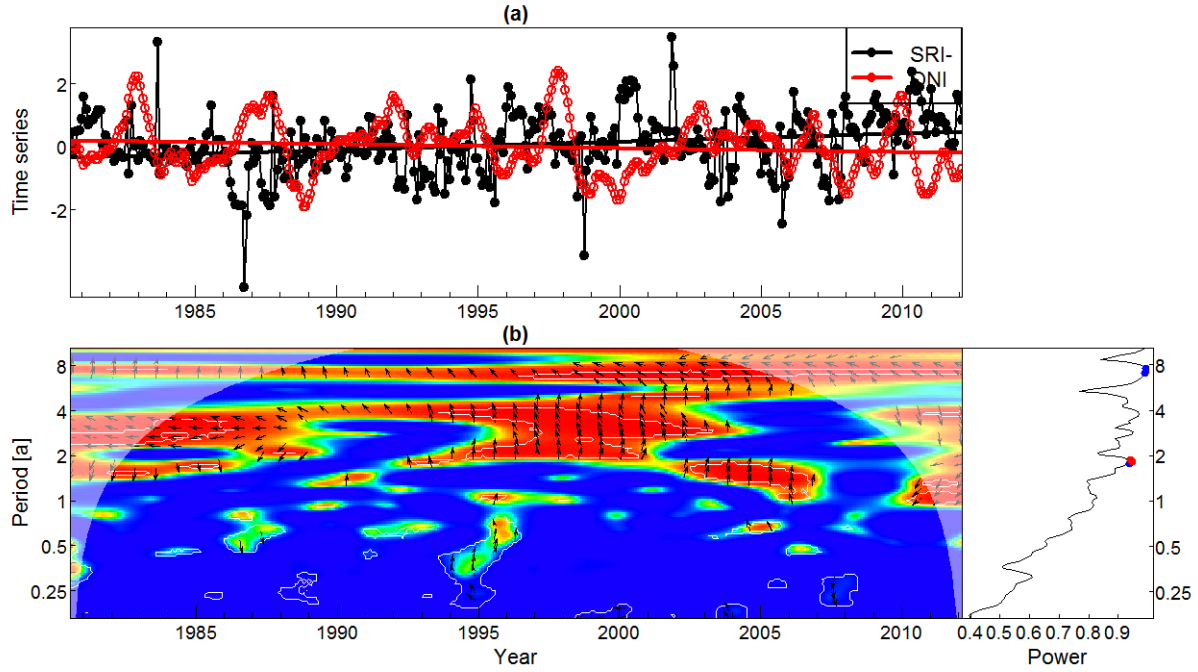

Figure 6-62: Mokolo River (Mokolo Nature Reserve): Standardized runoff index (SRI) and Oceanic Nino Index (ONI) time series plot (upper) and wavelet coherence plot (lower). Arrow directions indicate the phase relationship: in phase (right), antiphase (left), red leading black (down), black leading red (up).

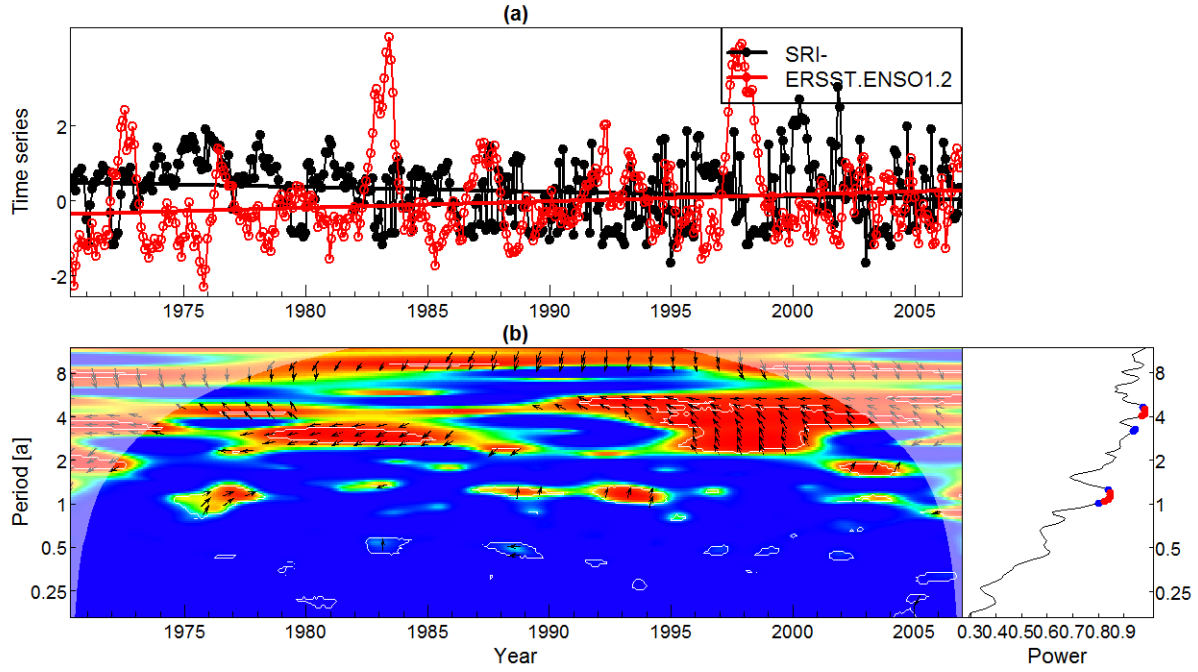

Figure 6-63: Mogalakwena River (Glen Alpine): Standardized runoff index (SRI) and time series plot (upper) and NINO1.2 (ERSST) wavelet coherence plot (lower). Arrow directions indicate the phase relationship: in phase (right), antiphase (left), red leading black (down), black leading red (up).

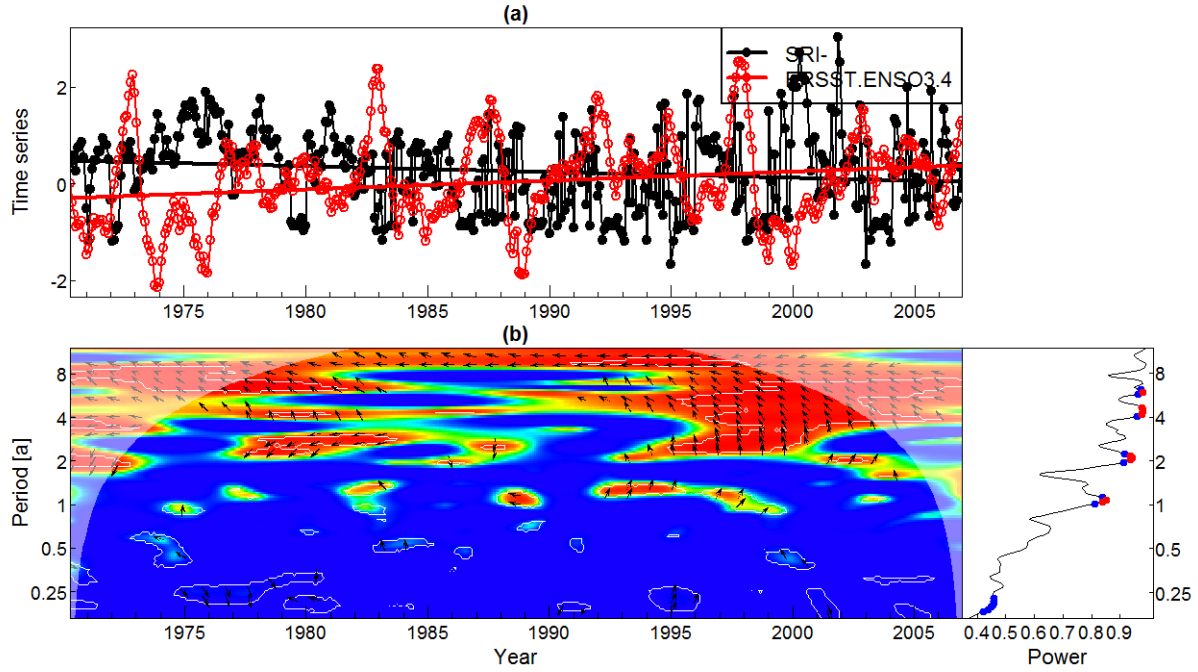

Figure 6-64: Mogalakwena River (Glen Alpine): Standardized runoff index (SRI) and time series plot (upper) and NINO3.4 (ERSST) wavelet coherence plot (lower). Arrow directions indicate the phase relationship: in phase (right), antiphase (left), red leading black (down), black leading red (up).

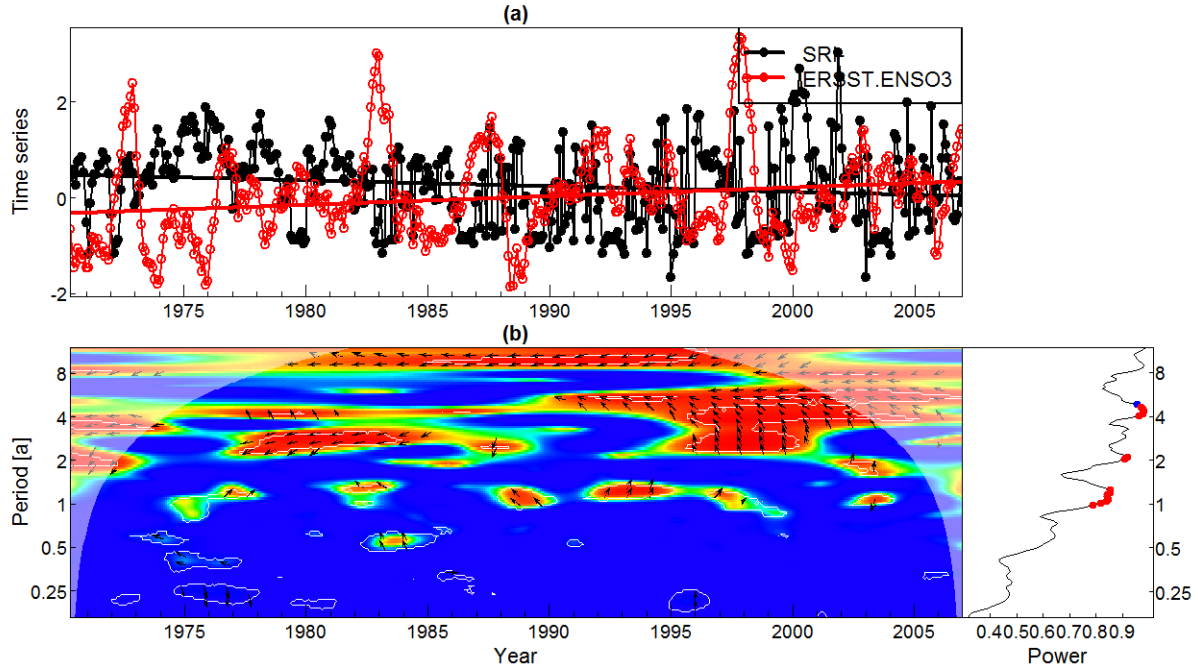

Figure 6-65: Mogalakwena River (Glen Alpine): Standardized runoff index (SRI) and time series plot (upper) and NINO3 (ERSST) wavelet coherence plot (lower). Arrow directions indicate the phase relationship: in phase (right), antiphase (left), red leading black (down), black leading red (up).

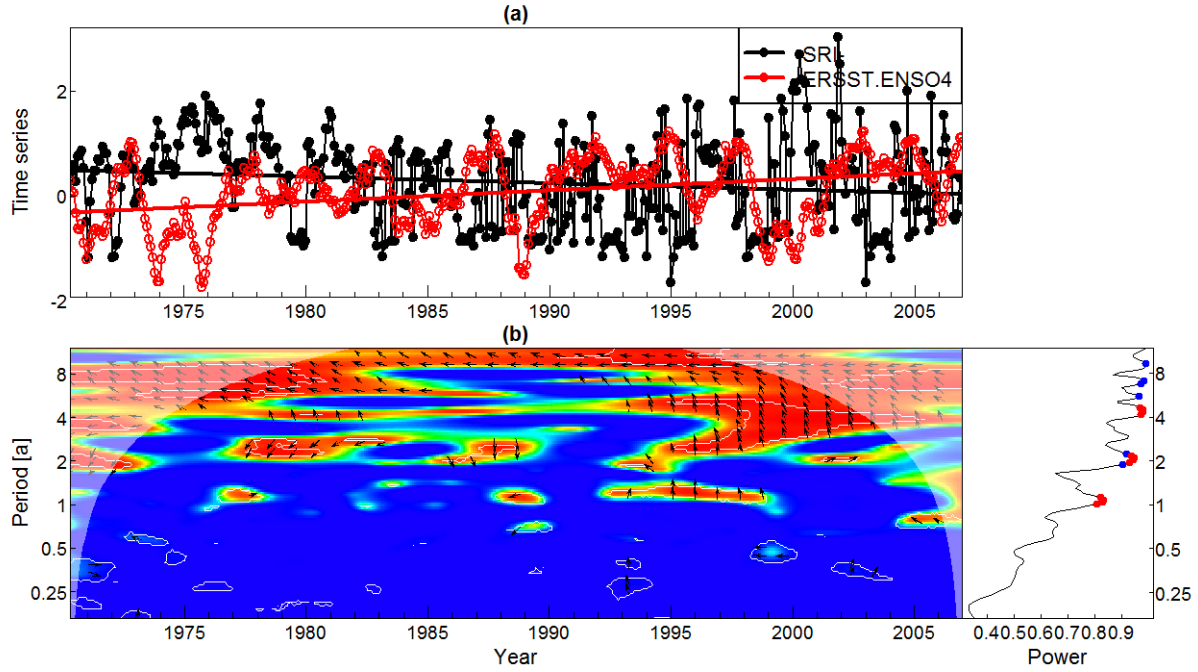

Figure 6-66: Mogalakwena River (Glen Alpine): Standardized runoff index (SRI) and time series plot (upper) and NINO4 (ERSST) wavelet coherence plot (lower). Arrow directions indicate the phase relationship: in phase (right), antiphase (left), red leading black (down), black leading red (up).

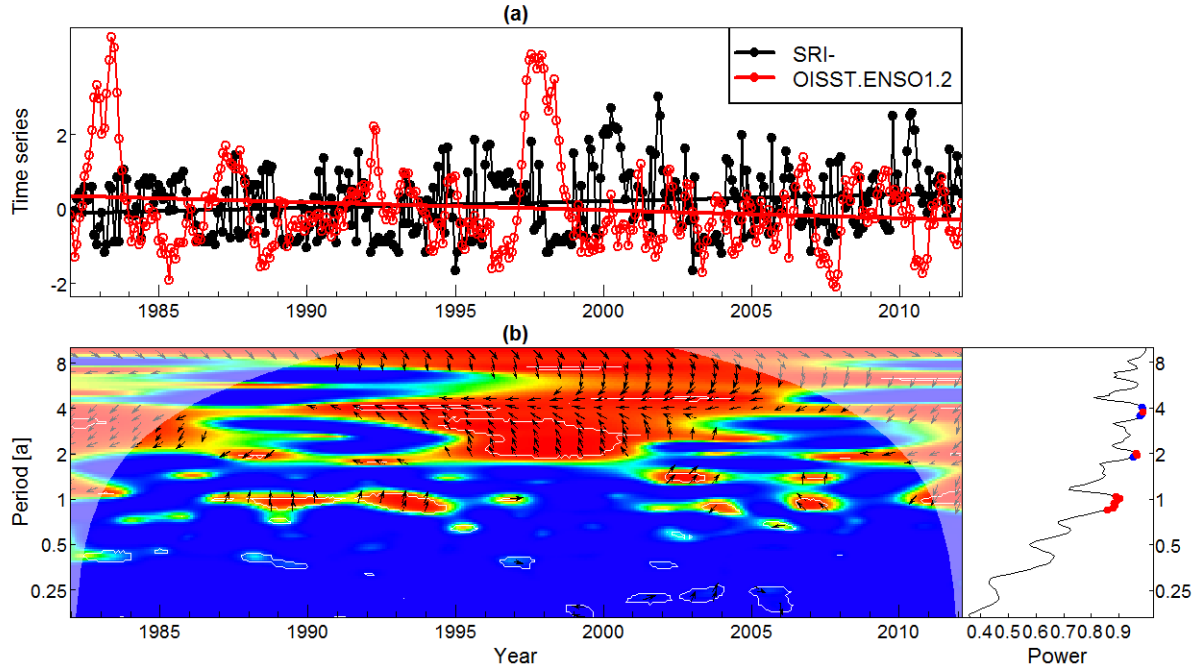

Figure 6-67: Mogalakwena River (Glen Alpine): Standardized runoff index (SRI) and NINO1.2 (OISST) time series plot (upper) and wavelet coherence plot (lower). Arrow directions indicate the phase relationship: in phase (right), antiphase (left), red leading black (down), black leading red (up).

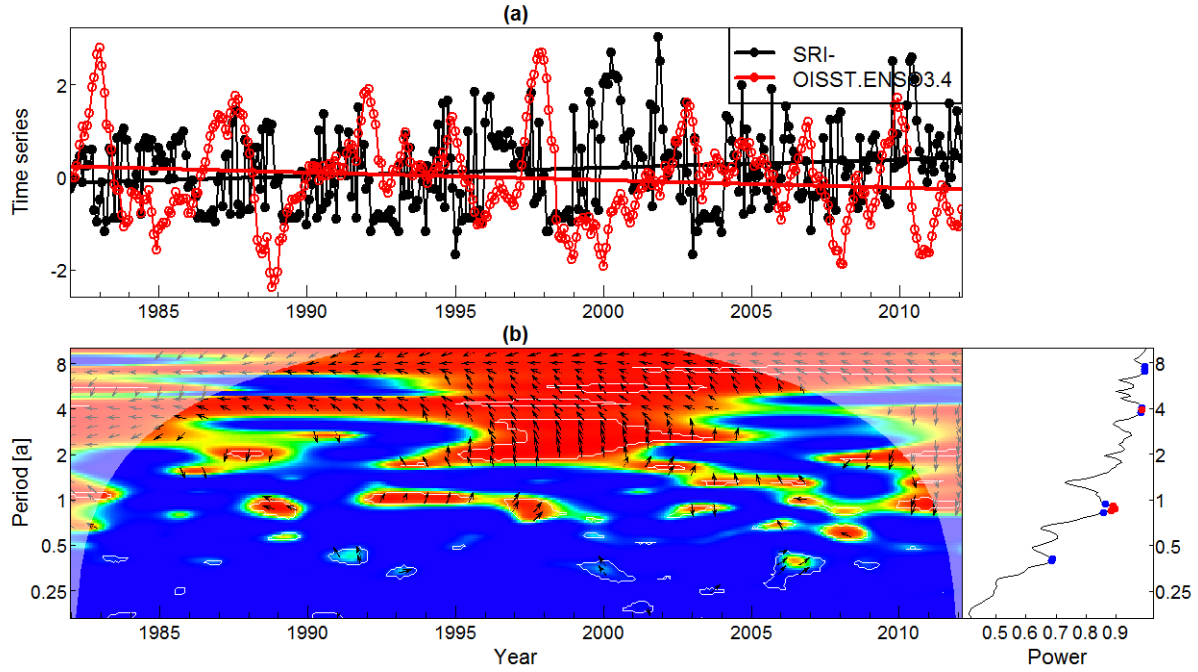

Figure 6-68: Mogalakwena River (Glen Alpine): Standardized runoff index (SRI) and NINO3.4 (OISST) time series plot (upper) and wavelet coherence plot (lower). Arrow directions indicate the phase relationship: in phase (right), antiphase (left), red leading black (down), black leading red (up).

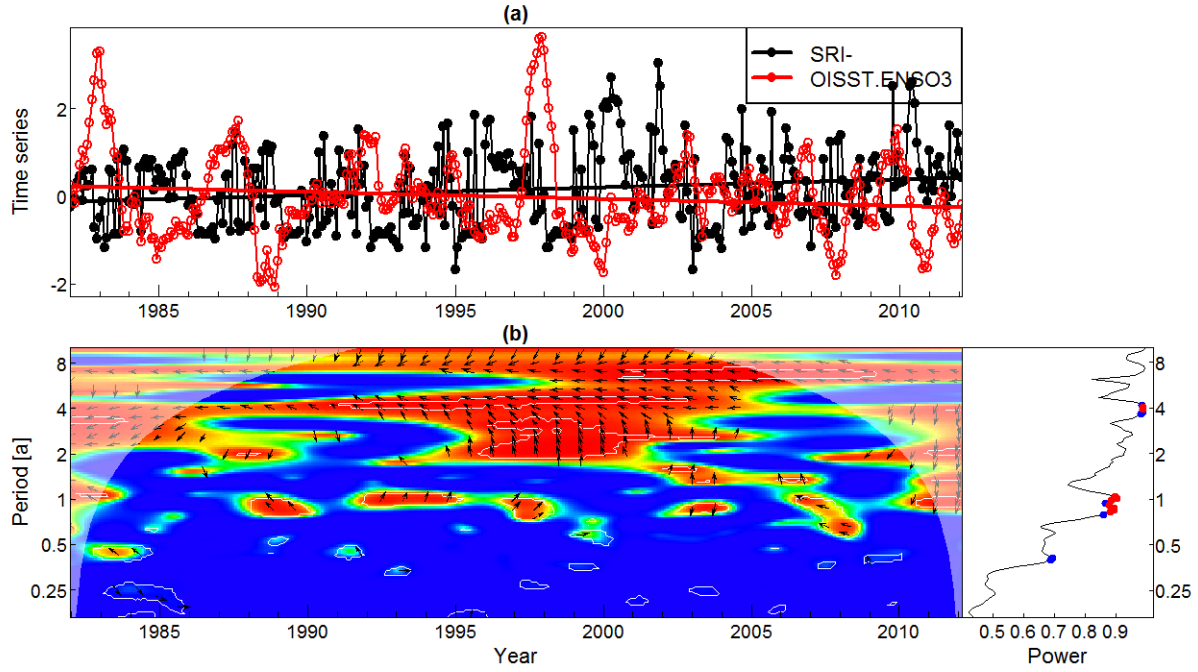

Figure 6-69: Mogalakwena River (Glen Alpine): Standardized runoff index (SRI) and NINO3 (OISST) time series plot (upper) and wavelet coherence plot (lower). Arrow directions indicate the phase relationship: in phase (right), antiphase (left), red leading black (down), black leading red (up).

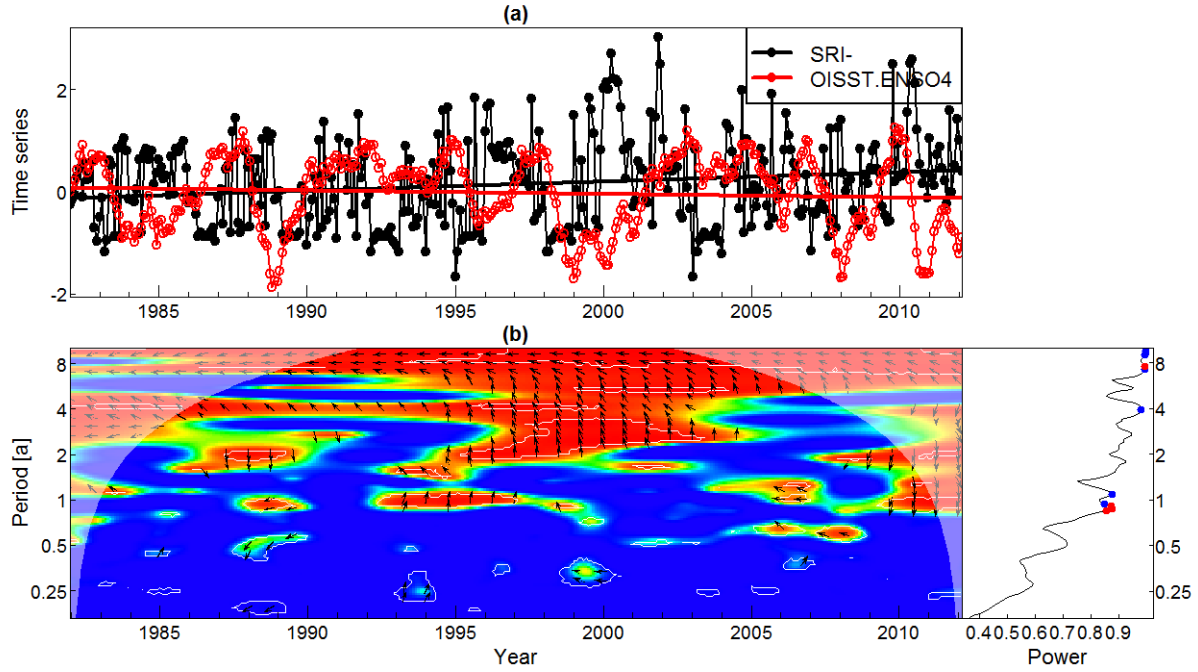

Figure 6-70: Mogalakwena River (Glen Alpine): Standardized runoff index (SRI) and NINO4 (OISST) time series plot (upper) and wavelet coherence plot (lower). Arrow directions indicate the phase relationship: in phase (right), antiphase (left), red leading black (down), black leading red (up).

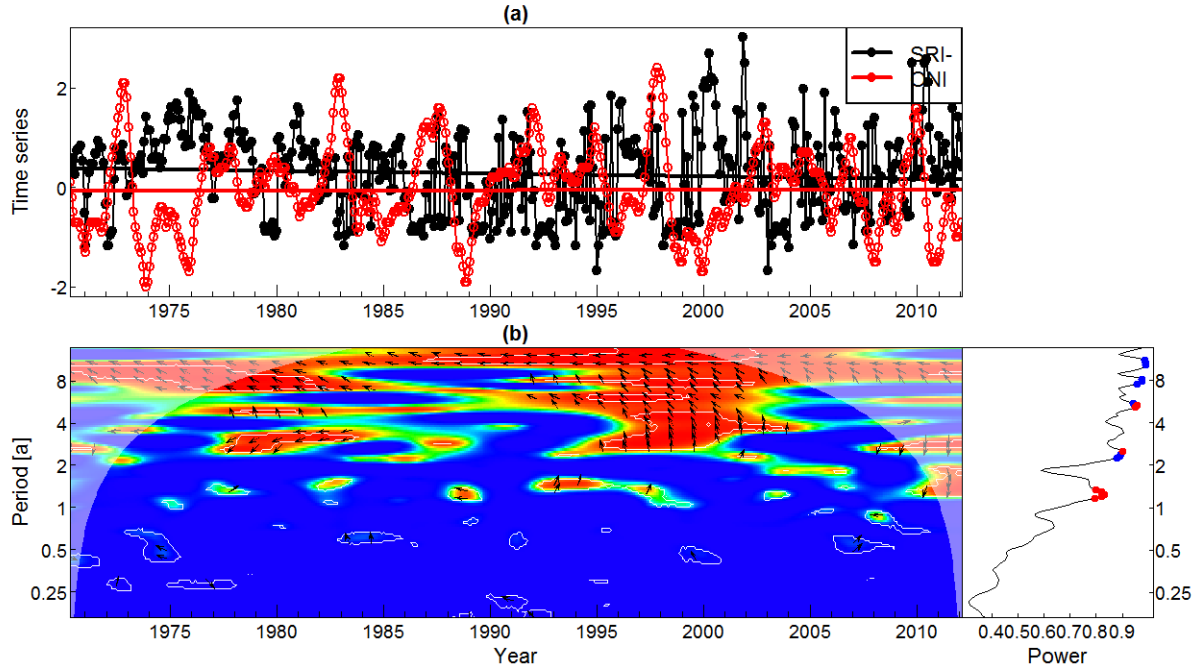

Figure 6-71: Mogalakwena River (Glen Alpine): Standardized runoff index (SRI) and Oceanic Nino Index (ONI) time series plot (upper) and wavelet coherence plot (lower). Arrow directions indicate the phase relationship: in phase (right), antiphase (left), red leading black (down), black leading red (up).

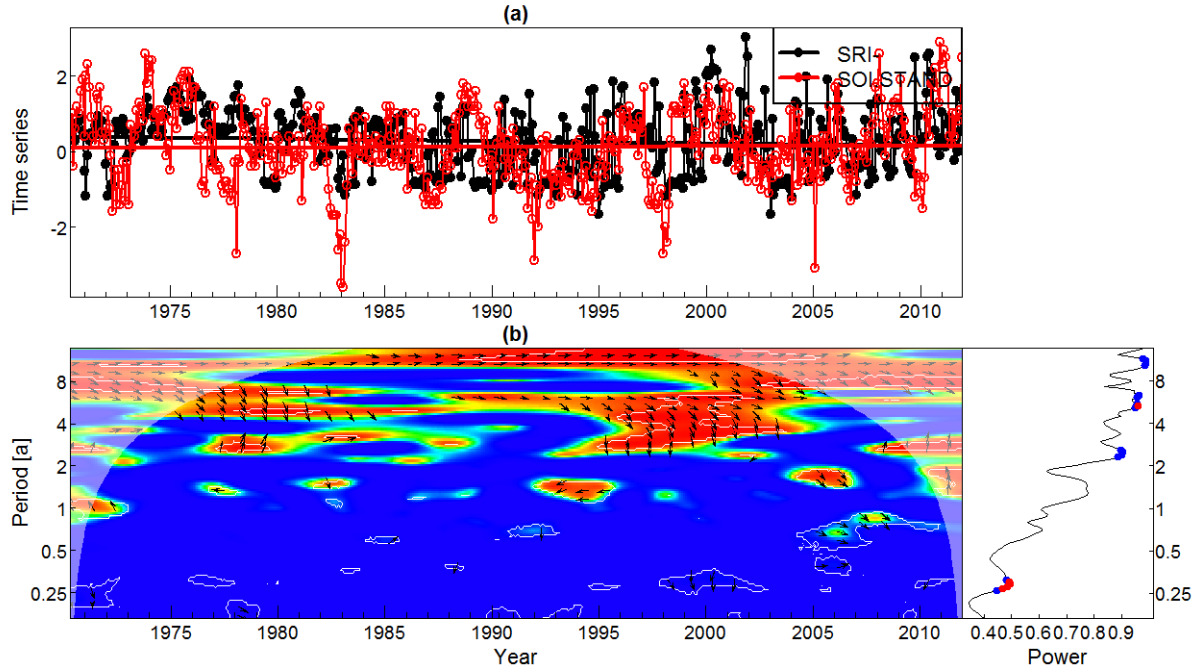

Figure 6-72: Mogalakwena River (Glen Alpine): Standardized runoff index (SRI) and Southern Oscillation Index (SOI) time series plot (upper) and wavelet coherence plot (lower). Arrow directions indicate the phase relationship: in phase (right), antiphase (left), red leading black (down), black leading red (up).

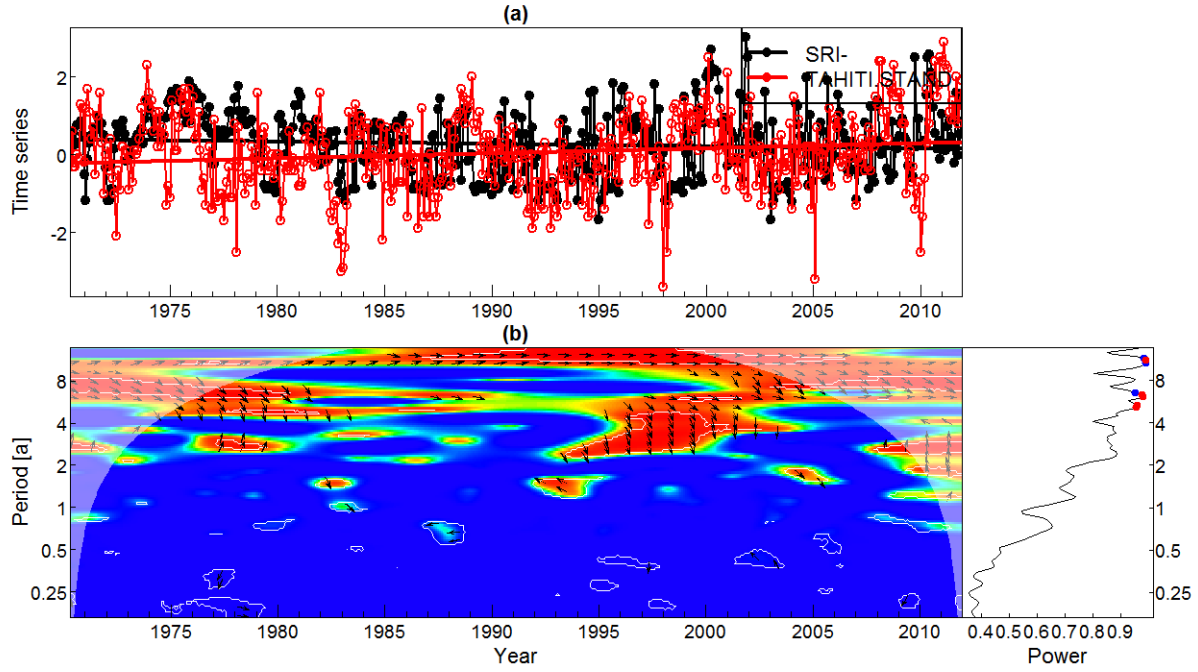

Figure 6-73: Mogalakwena River (Glen Alpine): Standardized runoff index (SRI) and Tahiti air pressure anomaly time series plot (upper) and wavelet coherence plot (lower). Arrow directions indicate the phase relationship: in phase (right), antiphase (left), red leading black (down), black leading red (up).